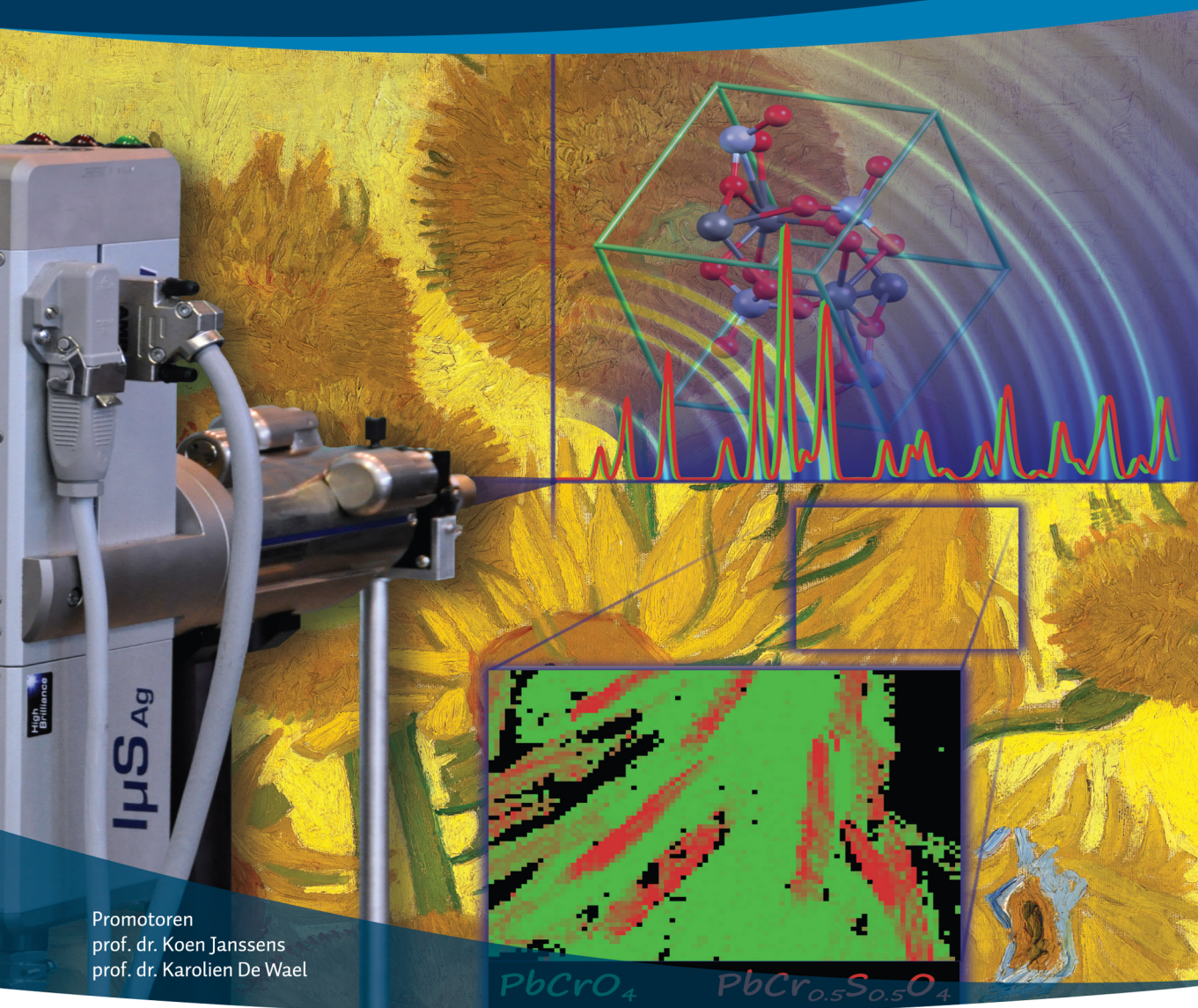


# Highly specific X-ray powder diffraction imaging at the macroscopic and microscopic scale

Proefschrift voorgelegd tot het behalen van de graad van doctor in de wetenschappen: chemie aan de Universiteit Antwerpen te verdedigen door

**Frederik Vanmeert**



Promotoren  
prof. dr. Koen Janssens  
prof. dr. Karolien De Wael

Faculteit Wetenschappen  
Departement Chemie  
Antwerpen 2019

 **Universiteit  
Antwerpen**



**Faculteit Wetenschappen**

Departement Chemie

# **Highly specific X-ray powder diffraction imaging at the macroscopic and microscopic scale**

Hoge specificiteit met röntgen-poederdiffractie als beeldvormende methode op  
de macroscopische en microscopische schaal

Proefschrift voorgelegd tot het behalen van de graad van doctor in de  
wetenschappen: chemie aan de Universiteit Antwerpen te verdedigen door

Frederik VANMEERT

Promotoren:

prof. dr. Koen Janssens

prof. dr. Karolien De Wael

Antwerpen, 2019

### **Front Cover**

*Sunflowers*, 1889, F458, Van Gogh, Van Gogh Museum

Modified from **Vanmeert, F.**; Hendriks, E.; Van der Snickt, G.; Monico, L.; Dik, J.; Janssens, K. “Chemical Mapping by Macroscopic X-ray Powder Diffraction (MA-XRPD) of Van Gogh's Sunflowers: Identification of Areas with Higher Degradation Risk” In: *Angew. Chem.-Int. Edit.* **2018**, 57 (25), 7418-7422. DOI: 10.1002/anie.201713293. Copyright 2018 John Wiley and Sons.

### **Back Cover**

Modified from **Vanmeert, F.**; De Nolf, W.; Dik, J.; Janssens, K. “Macroscopic X-ray Powder Diffraction Scanning: Possibilities for Quantitative and Depth-Selective Parchment Analysis” In: *Anal. Chem.* **2018**, 90 (11), 6445-6452. DOI: 10.1021/acs.analchem.8b00241. Copyright 2018 American Chemical Society.





---

# Table of Contents

---

Acknowledgments.....	9
<b>Chapter 1 – Introduction .....</b>	<b>B</b>
REFERENCES.....	17
<b>Chapter 2 – Instrument Development and Optimization .....</b>	<b>21</b>
2.1. INTRODUCTION.....	22
2.2. EXPERIMENTAL SECTION AND METHODS.....	24
2.2.1. MA-XRF/MA-XRPD setup.....	24
2.2.2. X-ray sources.....	25
2.2.3. Area detectors.....	29
2.2.4. Different MA-XRPD configurations.....	30
2.2.5. Figures-of-merit.....	32
2.2.6. Illuminated manuscript.....	34
2.2.7. MA-XRPD data processing.....	35
2.3. RESULTS AND DISCUSSION.....	37
2.3.1. Angular resolution.....	37
2.3.2. Spatial resolution.....	41
2.3.3. Signal-to-noise ratio (SNR).....	42
2.3.4. Angular range.....	45
2.3.5. Dead time.....	45
2.4. CASE STUDY.....	47
2.4.1. Illuminated 15 <sup>th</sup> /16 <sup>th</sup> century manuscript.....	47
2.5. CONCLUSIONS.....	56
ACKNOWLEDGMENTS.....	57
REFERENCES.....	58
<b>Chapter 3 – Visualizing Chrome Yellow Subtypes .....</b>	<b>61</b>
3.1. INTRODUCTION.....	62
3.2. EXPERIMENTAL SECTION AND METHODS.....	64
3.2.1. MA-XRF.....	64

3.2.2.	MA-XRPD .....	64
3.2.3.	MA-XRPD data processing.....	66
3.2.4.	Peak shift and displacement .....	66
3.2.5.	Preferred orientation .....	70
3.3.	RESULTS AND DISCUSSION.....	71
3.3.1.	Pigment Identification .....	71
3.3.2.	Chrome yellow subtypes .....	76
3.3.3.	Preferred orientation of LS-CY.....	82
3.4.	CONCLUSIONS.....	86
3.5.	SUPPORTING INFORMATION .....	87
3.5.1.	Raman Spectroscopy .....	87
	ACKNOWLEDGEMENTS.....	90
	REFERENCES.....	91

## **Chapter 4 – *In Situ* Determination of Degradation Products.....93**

4.1.	INTRODUCTION.....	94
4.2.	EXPERIMENTAL SECTION AND METHODS.....	97
4.2.1.	Still Life paintings.....	97
4.2.2.	MA-XRF/MA-XRPD instrument .....	99
4.2.3.	Data processing .....	101
4.2.4.	Relative sensitivity and information depth .....	102
4.3.	RESULTS AND DISCUSSION.....	112
4.3.1.	Overview of ground and pigment usage.....	112
4.3.2.	Transmission versus reflection mode .....	114
4.3.3.	Degradation phenomena.....	118
4.4.	CONCLUSIONS.....	128
4.5.	SUPPORTING INFORMATION .....	130
4.5.1.	Cross-section from <i>Still Life with Fruit and a Lobster</i> .....	130
	ACKNOWLEDGMENTS.....	131
	REFERENCES.....	132

## **Chapter 5 – Quantitative and Depth-Selective Analysis .....137**

5.1.	INTRODUCTION.....	138
5.2.	EXPERIMENTAL SECTION AND METHODS.....	142
5.2.1.	MA-XRF/MA-XRPD system .....	142
5.2.2.	Data processing .....	143

5.2.3. Illuminated manuscript.....	143
5.3. RESULTS AND DISCUSSION.....	145
5.3.1. Quantitative information.....	145
5.3.2. Depth-selective information.....	154
5.4. CONCLUSIONS.....	164
ACKNOWLEDGMENTS.....	166
REFERENCES.....	167
<b>Chapter 6 – Tomographic SR-<math>\mu</math>-XRPD Imaging.....</b>	<b>171</b>
6.1. INTRODUCTION.....	172
6.2. EXPERIMENTAL SECTION AND METHODS.....	175
6.2.1. Experimental setup at beamline P06.....	175
6.2.2. X-ray diffraction tomography.....	176
6.2.3. X-ray absorption tomography.....	176
6.2.4. $\mu$ -XRF/ $\mu$ -XRPD data processing.....	177
6.2.5. <i>Wheat stack under a cloud sky</i> , Van Gogh.....	177
6.3. RESULTS AND DISCUSSION.....	179
6.4. CONCLUSIONS.....	186
ACKNOWLEDGMENTS.....	187
REFERENCES.....	188
<b>Chapter 7 – Conclusions.....</b>	<b>193</b>
REFERENCES.....	199
Abstract.....	201
Samenvatting.....	203
Appendix – Publications.....	207





---

# Acknowledgments

---

I would like to start by expressing my gratitude to my main supervisor Koen Janssens for pushing me ever onwards in my struggle to understand new and exciting problems. His insights and abundant experience have been crucial for tackling many of the challenges faced throughout this work. I greatly appreciate the support of my second supervisor Karolien De Wael, especially during the final hours of this work.

I would like to thank all the current and former members of the AXES research group for making the past years not only scientifically interesting but also a truly pleasant period. I would like to specifically thank Wout de Nolf for sharing with me his knowledge on XRPD imaging and for his work on XRDUA which made my research possible. I will remember the endless hours spent together with Gert Nuyts and Letizia Monico at different synchrotron beamlines: we have had many nightly conversations and shared both happy and frustrating moments. I would like to further thank Stijn Legrand, Geert van der Snickt, Steven de Meyer, Matthias Alfeld, Simone Cagno, Willemien Anaf, Marie Radepont and Kevin Hellemans with whom I have worked closely over the years. A big thank you for all AXES colleagues for the many pleasant moments during group activities, board game nights, barbecues, after-work drinks, ... .

Research is not something you do by yourself and in the past years I have had many pleasant collaborations with scientists and conservators from various research groups and prestigious museums throughout Europe and beyond.

I deeply appreciate the openness with which I have been welcomed inside the different museums and am grateful for the unique opportunities that were given

to me to analyze some of their precious works of art. I would like to express my thanks to Lizet Klaasen and Johan Willems from the Royal Museum of Fine Arts Antwerp, Annelies van Loon, Nouchka de Keyser, Susan Smelt, Gwen Tauber and Petria Noble from the Rijksmuseum, Ella Hendriks from the Van Gogh Museum, Margje Leeuwenstein from the Kröller-Müller Museum, Griet Steyaert from Musea Brugge and Abbie Vandivere from the Mauritshuis. Without their interest and enthusiasm for newly developed analytical techniques most of my work would not have been possible.

Many beamline scientists have supported my work and I gratefully acknowledge their assistance during the many experiments: Gerald Falkenberg, Jan Garrevoet, Matthias Alfeld and Ulrike Boesenberg of beamline P06 and Karen Appel of beamline L at DESY, Marine Cotte, Wout de Nolf and Emeline Pouyet of beamline ID21 and Peter Cloetens, Alexandra Pacureanu, Remi Tucoulou and Jussi-Petteri Suuronen of beamlines ID16A-B at ESRF, Christian Mocuta and Solenn Reguer of beamline DiffAbs at SOLEIL.

Although not included in this work, I would like to thank Ole Lind, Véronique Rouchon, Gilian Odin, Maroussia Duranton, Oulfa Belhadj, Domagoj Mudronja, Stjepko Fazinic and Darko Tibljas for introducing me to various interesting topics and the pleasant collaborations over the years.

I want to thank all my friends and family for their unrelenting support and encouragement when I needed it. It has been a satisfying, but trying time and I want to thank you for your friendship and patience. I want to thank my parents and their partners for giving me the freedom to pursue my own path. My brother Rob and sister Marianne, their partners Sien and Davy and my little niece and nephews, Olivia, Merlijn and Cilian, to remind me of what is truly important in life. This has been a work of many years and I want to thank Sem and David for being there throughout these years, especially when frustrations got high.

Alba, you changed my life from the first moment you entered our office. Thank you for guiding me to the finish line. I am proud to say that my PhD is almost at its end.

To the many others that have not been mentioned: Thank you!



---

# Chapter 1 – Introduction

---

In the last decade, macroscopic X-ray fluorescence scanning (MA-XRF) has become an established method for noninvasive investigation of painted surfaces [1,2]. The resulting elemental maps provide complementary information to methods such as X-ray radiography (XRR) and Infrared reflectography (IRR) that are traditionally used for the investigation of these artworks. The distribution of pigments in, or below the surface of, paintings from well-known artists such as Van Eyck [3], Memling [4], Rembrandt [5,6], Magritte [7] and Van Gogh [8,9] have been examined with MA-XRF and reveal changes made by the artists during their creative process (*pentimenti*) or those carried out at a later date (e.g., during restorations) and can bring to light completely hidden underpaintings. The technique has contributed to and influenced the restoration process of well-known masterpieces [3,8] and while mostly used for the investigation of paintings [10], successful studies have been made on manuscripts [11-13] and stained-glass windows [14].

Since XRF only provides information on the presence of a range of chemical elements (phosphorus and upwards), the identification of pigments needs to be inferred based on the location of these elements and the color of the painted area. This becomes a problem when pigments with a similar elemental content, such as lead white (cerussite,  $\text{PbCO}_3$  and/or hydrocerussite,  $2\text{PbCO}_3 \cdot \text{Pb}(\text{OH})_2$ ), red lead (minium,  $\text{Pb}_3\text{O}_4$ ), Naples yellow (bindheimite,  $\text{PbSb}_2\text{O}_6 \cdot \text{PbO}$ ) and lead tin yellow ( $\text{Pb}_2\text{SnO}_4$ ) are used together, as they will all contribute to the Pb-L and Pb-M elemental distribution images. The lack of specificity of MA-XRF also becomes apparent when areas of artworks are considered in which degradation phenomena

have altered the appearance of the paint. A second drawback lies in the energy-dependent sampling depth for different elements. The elemental images corresponding to low energy X-rays, such as S-K, K-K and Ca-K, convey information limited to (usually) only the top visible surface of the painting (i.e., the top few  $\mu\text{m}$ ), which limits their usefulness, while those of, e.g., Cu-K, Pb-L and Hg-L reveal information that can come from much deeper (one to several hundreds of  $\mu\text{m}$  below the surface).

X-ray powder diffraction (XRPD) is an important technique for the direct identification of crystalline phases in complex mixtures; it is routinely performed using conventional benchtop diffractometers and more recently with micro ( $\mu$ -)XRPD instruments inside the laboratory [15,16]. The analysis normally requires removal of (a limited amount of) material from the artwork. Micro-destructive sampling of works of art such as precious paintings, in those cases where it is not entirely prohibited, is in practice limited to a small number of locations, e.g., in areas where paint loss already took place or where sampling does not disturb the aesthetic experience of the artwork (e.g., on the edges of a painting). For this reason, the use of noninvasive analogues has become increasingly popular and several portable (p-)XRPD instruments have already been developed [17]. For large immovable objects such as mural paintings and polychrome sculptures or in outdoor environments these instruments might be the only viable alternative to sampling; the long acquisition time (of the order of 20–60 min) required by these devices limits their use to *in situ* point-by-point investigations.

In recent years, the high specificity of XRD has been combined with the high spatial resolution achievable at state-of-the-art synchrotron radiation (SR) facilities leading to significantly more information. In the cultural heritage sector, SR-XRPD imaging at the (sub)microscopic scale has been employed for the study

of prehistoric flint-stones [18], ceramics from the Roman period [19] and porcelain from the Ming dynasty [20], for the identification of various pigments and artist materials [21-23], their degradation products (cadmium yellow [24], chrome yellow [9], vermilion red [25], red lead [26]) and formation of lead soaps [27]. At the macroscopic scale SR-XRPD has been employed for the investigation of Roman wall painting fragments in reflection geometry [28] and in transmission mode for imaging of illuminated manuscript cuttings [29] and Herculaneum papyri fragments [30] and an entire painting [31]. However it remains a tremendous undertaking, both financially and logistically, to guarantee the security and safety of a (precious) work of art during transportation to and its stay at such a large-scale facility.

In this thesis, various forms of specificity attainable with XRPD imaging are explored: at the chemical, material and spatial level. This high specificity is illustrated through applications at both the macroscopic and microscopic scale.

To better allow investigations at the macroscopic scale, XRPD imaging is transformed to a transportable noninvasive imaging technique that can be employed for the *in situ* investigation of artworks, e.g., inside museums and conservation workshops. To facilitate the successful conversion of MA-XRPD into a mobile instrument, a first instrumental study employing different combinations of laboratory X-ray sources and state-of-the-art X-ray sensitive area detectors was conducted. The impact of these devices on key characteristics, such as spatial and angular resolution and signal-to-noise ratio, is assessed in **Chapter 2**. Depending on the requirements of the object, different configurations are preferred. In this chapter a first case study on a 15<sup>th</sup>/16<sup>th</sup> century illuminated parchment is discussed.

In following chapters, the developed instrument has been applied for the *in situ* investigation of several oil paintings: the iconic *Sunflowers* painting by Van Gogh (**Chapter 3**), and two flower still life paintings by Jan Davidsz. de Heem and one



copy painting after De Heem (**Chapter 4**). These applications illustrate the capability of laboratory MA-XRPD imaging to deliver large-scale maps ( $\text{cm}^2 - \text{dm}^2$ ) reflecting the distribution of crystalline phases on/below the surface of flat painted artefacts in a noninvasive manner. Next to providing information on the distribution of the pigments employed by an artist, the chemical specificity of MA-XRPD also provides information on degradation products that have formed over time inside the paint layers. For the latter, a brief comparison between MA-XRPD in transmission (depth-averaged information) and reflection (superficial information) mode is made.

While mostly used for the identification of crystalline materials, XRPD can be used to extract more detailed information about the pigments employed. In **Chapter 5**, pigment mixtures, composed of the same compounds in different ratios, are distinguished using quantitative analysis resulting in a differentiation on the material level. These quantitative results can be directly linked to different pictorial features, indicating an artist's *modus operandi*, the usage of different batches of similar paint, or materials of various degrees of purity. While the 2D distribution images provide a projection of the entire layer build-up of the artwork, in this chapter the possibility for depth-selective discrimination between pigments at different depths in the paint stratigraphy is illustrated.

In **Chapter 6**, XRPD imaging is performed at the microscopic scale using (sub)microscopic X-ray beams available at synchrotron facilities to further elucidate the degradation pathway of the red lead pigment on a minute paint sample from *Wheat stack under a cloudy sky* by Van Gogh. For this purpose, tomographic  $\mu$ -XRPD imaging is exploited for both its chemical and spatial specificity.

Note: In this thesis the mineralogical names of pigments are used without implying their origin (mineralogical or synthetic), unless specifically mentioned.

**REFERENCES**

- [1] Alfeld, M.; Broekaert, J. A. C. *Spectrochim. Acta, Part B* **2013**, *88*, 211-230.
- [2] Alfeld, M.; de Viguerie, L. *Spectrochim. Acta, Part B* **2017**, *136*, 81-105.
- [3] Van der Snickt, G.; Dubois, H.; Sanyova, J.; Legrand, S.; Coudray, A.; Glaude, C.; Postec, M.; Van Espen, P.; Janssens, K. *Angew. Chem.-Int. Edit.* **2017**, *56*, 4797-4801.
- [4] Janssens, K.; Legrand, S.; Van der Snickt, G.; Vanmeert, F. *Elements* **2016**, *12*, 39-44.
- [5] Alfeld, M.; Siddons, D. P.; Janssens, K.; Dik, J.; Woll, A.; Kirkham, R.; van de Wetering, E. *Appl. Phys. A: Mater. Sci. Process.* **2013**, *III*, 157-164.
- [6] Janssens, K.; Van der Snickt, G.; Alfeld, M.; Noble, P.; van Loon, A.; Delaney, J.; Conover, D.; Zeibel, J.; Dik, J. *Microchem. J.* **2016**, *126*, 515-523.
- [7] Van der Snickt, G.; Martins, A.; Delaney, J.; Janssens, K.; Zeibel, J.; Duffy, M.; McGlinchey, C.; Van Driel, B.; Dik, J. *Appl. Spectrosc.* **2016**, *70*, 57-67.
- [8] Alfeld, M.; Van der Snickt, G.; Vanmeert, F.; Janssens, K.; Dik, J.; Appel, K.; van der Loeff, L.; Chavannes, M.; Meedendorp, T.; Hendriks, E. *Appl. Phys. A: Mater. Sci. Process.* **2013**, *III*, 165-175.
- [9] Monico, L.; Janssens, K.; Hendriks, E.; Vanmeert, F.; Van der Snickt, G.; Cotte, M.; Falkenberg, G.; Brunetti, B. G.; Miliani, C. *Angew. Chem.-Int. Edit.* **2015**, *54*, 13923-13927.
- [10] Janssens, K.; Van der Snickt, G.; Vanmeert, F.; Legrand, S.; Nuyts, G.; Alfeld, M.; Monico, L.; Anaf, W.; De Nolf, W.; Vermeulen, M.; Verbeeck, J.; De Wael, K. *Top. Curr. Chem.* **2016**, 374.
- [11] Mosca, S.; Frizzi, T.; Pontone, M.; Alberti, R.; Mbelli, L.; Capogrosso, V.; Nevin, A.; Valentini, G.; Comelli, D. *Microchem. J.* **2016**, *124*, 775-784.
- [12] Ricciardi, P.; Legrand, S.; Bertolotti, G.; Janssens, K. *Microchem. J.* **2016**, *124*, 785-791.

- [13] Pouyet, E.; Devine, S.; Grafakos, T.; Kieckhefer, R.; Salvant, J.; Smieska, L.; Woll, A.; Katsaggelos, A.; Cossairt, O.; Walton, M. *Anal. Chim. Acta* **2017**, *982*, 20-30.
- [14] Van der Snickt, G.; Legrand, S.; Caen, J.; Vanmeert, F.; Alfeld, M.; Janssens, K. *Microchem. J.* **2016**, *124*, 615-622.
- [15] Duran, A.; Perez-Rodriguez, J. L.; Jimenez de Haro, M. C. *Anal. Bioanal. Chem.* **2009**, *394*, 1671-1677.
- [16] Svarcova, S.; Koci, E.; Bezdicka, P.; Hradil, D.; Hradilova, J. *Anal. Bioanal. Chem.* **2010**, *398*, 1061-1076.
- [17] Nakai, I.; Abe, Y. *Appl. Phys. A: Mater. Sci. Process.* **2012**, *106*, 279-293.
- [18] Lombardo, T.; Grolimund, D.; Kienholz, A.; Hubert, V.; Worle, M. *Microchem. J.* **2016**, *125*, 254-259.
- [19] Sciau, P.; Goudeau, P.; Tamura, N.; Dooryhee, E. *Appl. Phys. A* **2006**, *83*, 219-224.
- [20] Wang, T.; Zhu, T. Q.; Feng, Z. Y.; Fayard, B.; Pouyet, E.; Cotte, M.; De Nolf, W.; Salome, M.; Sciau, P. *Anal. Chim. Acta* **2016**, *928*, 20-31.
- [21] Welcomme, E.; Walter, P.; Bleuet, P.; Hodeau, J. L.; Dooryhee, E.; Martinetto, P.; Menu, M. *Appl. Phys. A: Mater. Sci. Process.* **2007**, *89*, 825-832.
- [22] Van der Snickt, G.; De Nolf, W.; Vekemans, B.; Janssens, K. *Appl. Phys. A* **2008**, *92*, 59-68.
- [23] Gonzalez, V.; Wallez, G.; Calligaro, T.; Cotte, M.; De Nolf, W.; Eveno, M.; Ravaud, E.; Menu, M. *Anal. Chem.* **2017**, *89*, 13203-13211.
- [24] Van der Snickt, G.; Janssens, K.; Dik, J.; De Nolf, W.; Vanmeert, F.; Jaroszewicz, J.; Cotte, M.; Falkenberg, G.; Van der Loeff, L. *Anal. Chem.* **2012**, *84*, 10221-10228.
- [25] Radepont, M.; de Nolf, W.; Janssens, K.; Van der Snickt, G.; Coquinot, Y.; Klaassen, L.; Cotte, M. *J. Anal. At. Spectrom.* **2011**, *26*, 959.

- [26] Vanmeert, F.; Van der Snickt, G.; Janssens, K. *Angew. Chem.-Int. Edit.* **2015**, *54*, 3607-3610.
- [27] Cotte, M.; Checroun, E.; De Nolf, W.; Taniguchi, Y.; De Viguerie, L.; Burghammer, M.; Walter, P.; Rivard, C.; Salomé, M.; Janssens, K.; Susini, J. *Stud. Conserv.* **2017**, *62*, 2-23.
- [28] Dooryhée, E.; Anne, M.; Bardiès, I.; Hodeau, J. L.; Martinetto, P.; Rondot, S.; Salomon, J.; Vaughan, G. B. M.; Walter, P. *Appl. Phys. A* **2005**, *81*, 663-667.
- [29] Smieska, L. M.; Mullett, R.; Ferri, L.; Woll, A. R. *Appl. Phys. A* **2017**, *123*, 484.
- [30] Brun, E.; Cotte, M.; Wright, J.; Ruat, M.; Tack, P.; Vincze, L.; Ferrero, C.; Delattre, D.; Mocella, V. *Proc. Natl. Acad. Sci. U S A* **2016**, *113*, 3751-3754.
- [31] De Nolf, W.; Dik, J.; Van der Snickt, G.; Wallert, A.; Janssens, K. *J. Anal. At. Spectrom.* **2011**, *26*, 910.

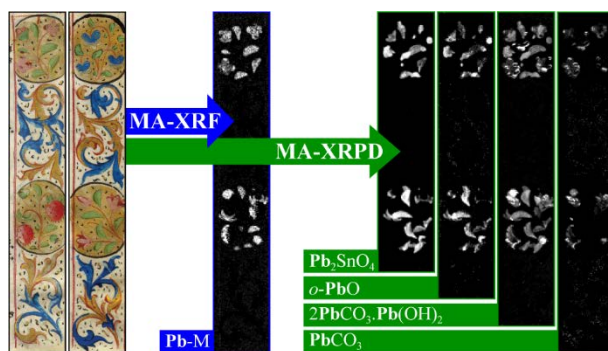


---

# Chapter 2 – Instrument Development and Optimization

---

*In this chapter, the development of a novel MA-XRF/MA-XRPD instrument using a laboratory X-ray source is presented. Several combinations of X-ray sources and area detectors are evaluated in terms of their*



*spatial and angular resolution and their sensitivity. The highly-specific imaging capability of the combined MA-XRF/MA-XRPD instrument is demonstrated on a 15<sup>th</sup>/16<sup>th</sup> century illuminated manuscript directly revealing the distribution of a large number of inorganic pigments. This case study illustrates the wealth of new mapping information that can be obtained in a noninvasive manner using the laboratory MA-XRF/MA-XRPD instrument.*

This chapter is a modified version of a published paper: Reprinted with permission from Vanmeert, F.; De Nolf, W.; De Meyer, S.; Dik, J.; Janssens, K. “Macroscopic X-ray Powder Diffraction Scanning, a New Method for Highly Selective Chemical Imaging of Works of Art: Instrument Optimization” In: *Anal. Chem.* **2018**, *90* (II), 6436-6444. DOI: 10.1021/acs.analchem.8b00240. Copyright 2018 American Chemical Society

## 2.1. INTRODUCTION

Over the past ten years macroscopic X-ray fluorescence imaging (MA-XRF) has established itself as an important new tool for imaging of (flat) works of art, delivering significantly more pictorial and material-specific information than traditional X-ray radiography. The resulting elemental distributions provide not only information about the usage of (mostly) inorganic pigments throughout the artwork, but also reveal changes made by the artists during its creative process (*pentimenti*) or carried out at a later date (e.g. during restorations) and can bring to light completely hidden underpaintings [1-3]. Its successful implementation into a mobile instrument [4] has made MA-XRF available to curators, conservators and conservation scientists inside museums worldwide; many major museums in Europe and the US now use this method. Various MA-XRF instruments have been developed since [5-10]. While the development of these mobile MA-XRF instruments has significantly impacted cultural heritage research, the obtained information is limited to the elemental level [11,12].

In order to differentiate between compounds with similar elemental content (e.g., hematite,  $\text{Fe}_2\text{O}_3$ , and goethite,  $\alpha\text{-FeOOH}$ ; or malachite,  $\text{CuCO}_3\cdot\text{Cu}(\text{OH})_2$ , and azurite,  $2\text{CuCO}_3\cdot\text{Cu}(\text{OH})_2$ ), molecular imaging techniques, such as visible/near infrared (VNIR) reflectance imaging and macroscopic FTIR scanning in reflection mode (MA-rFTIR), have recently been developed [12-16]. While XRPD imaging allows for a direct identification of inorganic crystalline species in complex samples, it is available only at synchrotron radiation facilities for (mostly) microscopic investigations of small samples [17,18]. MA-XRPD investigations employing synchrotron radiation are much more scarce, owing to the cost and risks involved during transportation of a precious work of art to these facilities. In order to broaden the applicability of this technique, the development of a combined MA-XRF/MA-XRPD laboratory instrument is described in this chapter.

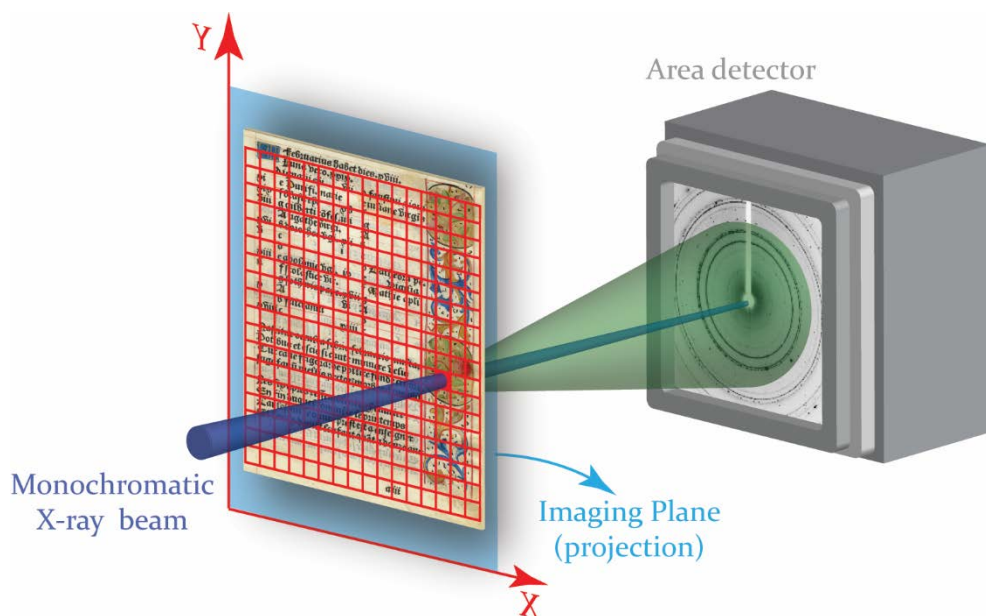


Figure 2-1 Schematic illustration of a MA-XRPD imaging experiment.

The schematic principle of the MA-XRPD instrument is illustrated in Figure 2-1. A low power X-ray microsource combined with focusing optics (e.g., polycapillary lenses) that can simultaneously function as an energy-discriminator (e.g., multilayer mirrors and double-curved crystals) delivers a (slightly) focused and monochromatic X-ray beam that is used to raster-scan the work of art. In each point a diffraction image is collected using an X-ray sensitive area detector. These diffraction images contain information about the crystalline contents in each analyzed point.

In this chapter different combinations of X-ray sources and area detectors placed in different geometries are evaluated using several figures-of-merit: the angular and spatial resolution, the signal-to-noise ratio, the captured angular range and the dead time in between consecutive measurements. The highly-specific and noninvasive imaging capabilities of the instruments is demonstrated on a sheet of parchment from an illuminated 15<sup>th</sup>/16<sup>th</sup> century Book of Tides.



## 2.2. EXPERIMENTAL SECTION AND METHODS

### 2.2.1. MA-XRF/MA-XRPD setup

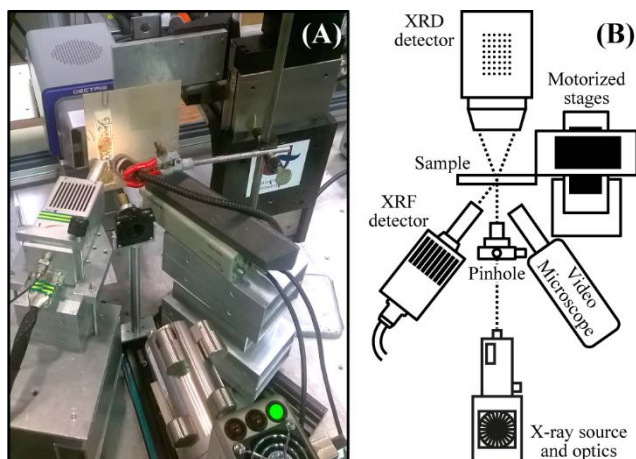


Figure 2-2. Photograph (A) and schematic (B) of a MA-XRF/MA-XRPD instrument in transmission mode.

In the combined MA-XRF/MA-XRPD systems the X-ray source with beam defining/focusing optic is placed perpendicular to the (essentially two-dimensional) work of art (Figure 2-2). The monochromatic X-rays required for XRPD are selected from the output of the X-ray tube either via a  $K_{\beta}$ -filter or a multilayer grating. In this chapter, powder diffraction signals are exclusively collected in transmission mode by positioning the area detector behind the object and perpendicular to the primary X-ray beam. Reflection-mode scanning MA-XRPD measurements, while quite feasible to realize, are not discussed here but will be addressed in Chapter 4. A (semi-transparent) beam stop is used to protect the detector from direct exposure to the primary beam. A Vortex-EX silicon drift detector (SII, Northridge, CA, US) allows for the acquisition of fluorescence radiation. The Vortex detector benefits from a large active area ( $\pm 50 \text{ mm}^2$ ) and has a typical energy resolution of  $< 165 \text{ eV FWHM}$  (at  $\text{Mn-K}_{\alpha}$ ).

The entire instrument remains stationary while the artwork is moved using XYZ motorized stages (Newport Corporation, Irvine, CA, USA; maximum travel ranges: 10 cm × 25 cm × 10 cm). The artwork is positioned by use of a video camera with limited depth of field. The entire scanning operation, including motor movements and acquisitions, is controlled by in-house software. Calibration of various instrumental parameters is performed using a LaB<sub>6</sub> standard for powder diffraction (SRM 660, NIST).

## 2.2.2. X-ray sources

### 2.2.2.1. Determination of the X-ray beam profile

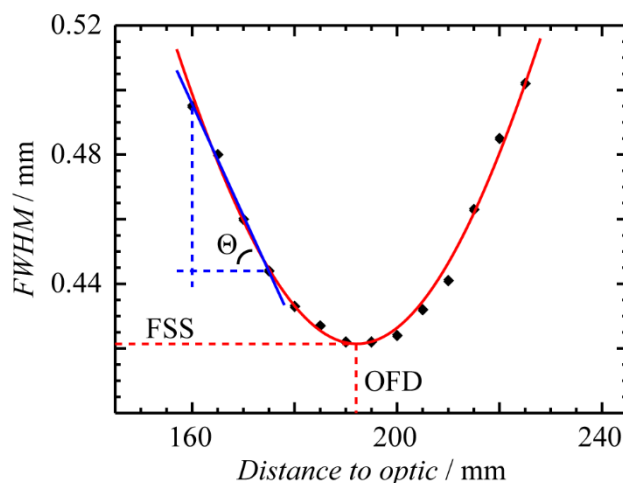


Figure 2-3. Plot of the FWHM of the focused X-ray beam at various distances from the optic showing OFD and FSS (red, Gaussian fit) and  $\Theta$  (blue, linear fit).

The output focal distance (OFD), focal spot size (FSS) and divergence ( $\Theta$ ) were experimentally determined using wire (Zr or Fe/Cr18/Ni8 wire, 25  $\mu\text{m}$ , Goodfellow) or knife-edge (Zr foil, 25  $\mu\text{m}$ , Goodfellow) scans for all X-ray sources (excluding I $\mu$ S-Mo). The beam size was determined at various distances from the exit of the X-ray optic by measuring the Fe-K or Zr-K fluorescence while scanning

the wire or foil transverse to the beam axis. The full-width-at-half-maximum (FWHM) of the profiles was used as an estimate for the beam sizes (Figure 2-3). The OFD and FSS of the X-ray optic was determined with a Gaussian fit through the different FWHM values. The slope of the linear fit corresponds to the divergence ( $\Theta$ ) of the beam which is valid for small angles. The relative beam intensities of the Warrikhoff source was measured using the Zr-K fluorescence originating from a Zr foil ( $25\ \mu\text{m}$ ) placed at a fixed distance from the source for different input focal distances (IFD).

#### 2.2.2.2. Polycapillary-based X-ray source

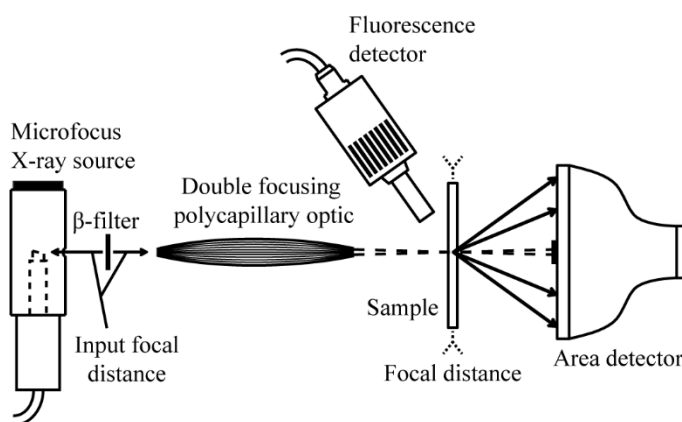


Figure 2-4. Schematic illustration of the Warrikhoff source combined with a double focusing polycapillary optic.

The low power Mo anode X-ray micro source (RTW-Röntgentechnik Dr Warrikhoff GmbH & Co. KG, D) was equipped with a double polycapillary lens (00-SF-01, X-ray Optics Laboratory, Beijing Normal University, CN) as beam forming optic [19]. By placing a simple  $K_{\beta}$ -filter (Zr foil,  $50\ \mu\text{m}$ , Goodfellow, UK) between the source and polycapillary lens to suppress the unwanted Mo- $K_{\beta}$  radiation and part of the background continuum of the X-ray tube, an X-ray micro beam with divergence, monochromaticity and intensity adequate for conducting

XRPD experiments can be formed without the need for a more elaborate monochromator [20].

Although it is well documented that the properties of a polycapillary lens are energy dependent [21], they also depend on the distance between the X-ray source anode and the lens. For optimal output intensity, the X-ray source spot is placed at the designed input focal distance (IFD) of the double focusing polycapillary as shown in Figure 2-4. By positioning the polycapillary lens closer to the source spot than the optimal IFD of the lens (and thus ‘out of focus’) the beam is reduced not only in intensity, but also the FSS,  $\Theta$  and OFD become smaller, as shown in Table 2-1.

**Table 2-1. Characteristics of the X-ray beam formed by the polycapillary optic (00-SF-01) at different IFD <sup>a</sup>**

Label	IFD (cm)	OFD (cm)	$\Theta$ (mrad)	FSS ( $\mu\text{m}$ )	Relative intensity (%)
IFD <sub>1</sub>	4.3 (1)	4.0 (1)	1.4 (2)	205 (2)	8.5 (1)
IFD <sub>2</sub>	5.9 (1)	11.4 (1)	1.1 (1)	307 (1)	19.6 (1)
IFD <sub>3</sub>	6.9 (1)	17.6 (1)	2.0 (1)	381 (1)	43.4 (1)
IFD <sub>4</sub>	7.9 (1)	19.2 (1)	3.7 (1)	422 (1)	100.0 (2)
IFD <sub>5</sub>	8.5 (1)	18.7 (1)	3.8 (1)	389 (2)	49.8 (1)

<sup>a</sup> Errors are given in parentheses.

Changing from IFD<sub>4</sub> to IFD<sub>1</sub> improves the divergence from 3.7 (1) to 1.4 (2) mrad and the FSS from 422 to 205  $\mu\text{m}$ , at the expense of an appreciable decrease in the focused beam flux (8.5% relative to the intensity at the designed input distance IFD<sub>4</sub>). At smaller IFD, the transmission of the polycapillary lens decreases as the X-rays entering the outer capillaries exceed the critical angle for total external reflection and become absorbed. If the IFD is increased beyond IFD<sub>4</sub> (e.g. to IFD<sub>5</sub>) a smaller solid angle of the tube output is captured by the lens, leading to a lower output intensity of the optic.

### 2.2.2.3. Mirror-based X-ray sources

The Incoatec microsources (I $\mu$ S; Incoatec GmbH, D) make use of a Montel optic consisting of two perpendicular mirrors coated with laterally graded multilayers [22]. The Montel multilayer optic simultaneously functions as energy discriminator and as focusing device. The mirrors are kept under low vacuum (several mbar) to prevent degradation of the coating. Focusing optics with large focal distances (between 20 and 40 cm) and limited divergence (< 5 mrad) were chosen to minimize broadening of the diffraction signals. The Incoatec sources can be equipped with several flight tubes to reduce air absorption between optic and sample; a collimator is used to separate the double focused X-ray beam from the unfocused and single focused beams generated by the Montel optics. An Al filter (30  $\mu$ m) was used with the I $\mu$ S-Ag<sup>HB</sup> X-ray source to suppress Ag-L radiation in the primary beam. Table 2-2 lists the specifications of the Incoatec sources.

**Table 2-2. Technical specifications of the I $\mu$ S sources**

	I $\mu$ S-Cu	I $\mu$ S-Cu <sup>HB</sup>	I $\mu$ S-Mo	I $\mu$ S-Ag <sup>HB</sup>
Primary Energy		Cu-K $\alpha$	Mo-K $\alpha$	Ag-K $\alpha$
Optics	Graded multilayer (W/C)			
Power (W)	30	50	30	44
Voltage (kV)	50			
Current ( $\mu$ A)	600	1000	600	880
OFD (cm) <sup>ab</sup>	39.8 (1)	19.6 (1)	21	21.6 (1)
FSS ( $\mu$ m) <sup>a</sup>	313 (5)	142 (2)	110	112 (3)
$\Theta$ (mrad) <sup>a</sup>	2.6 (4)	2.4 (1)	5	3.8 (3)
Flux (photon s <sup>-1</sup> )	7.0 10 <sup>8</sup>	2.9 10 <sup>8</sup>	1.3 10 <sup>7</sup>	1.1 10 <sup>7</sup>
Cooling	air cooling			
Weight (kg) <sup>c</sup>	6.6	7.2	6.6	7.2

<sup>a</sup> Experimentally determined for all X-ray sources except I $\mu$ S-Mo. Errors are given in parentheses.

<sup>b</sup> Including the length of flight tubes.

<sup>c</sup> Including the optics.

### 2.2.3. Area detectors

A SMART 1000 CCD camera (Bruker AXS Inc., WI, USA) and several hybrid photon counting pixel detectors, PILATUS 100K, PILATUS 200K (Dectris Ltd., CH) and XPAD SI40 (ImXPAD SAS, FR) were used. Their characteristics are summarized in Table 2-3.

**Table 2-3. Technical specifications of the area detectors**

	SMART 1000 CCD	PILATUS 100K	PILATUS 200K	XPAD SI40
Active area (mm <sup>2</sup> )	62.5 × 62.5	83.8 × 33.5	83.8 × 70	75 × 30
# pixels	1024 × 1024	487 × 195	487 × 407	560 × 240
Pixel size (μm)	61		172	130
Point spread function	not known		1 pixel	
Detection method	Scintillator <sup>a</sup>		Si	
Detector thickness (μm)	/	320	1000	500
Detection efficiency <sup>b</sup>				
Cu-K <sub>α</sub>	/	0.97	0.96	0.99
Mo-K <sub>α</sub>	0.9	0.37	0.76	0.51
Ag-K <sub>α</sub>	/	0.20	0.51	0.30
Read-out time	10 s	< 3 ms	7 ms	6 ms

<sup>a</sup> highly effective phosphor optimized for Mo radiation (Conversion rate: ~ 40 e<sup>-</sup> per Mo X-ray photon)

<sup>b</sup> SMART 1000 CCD: stopping power of the phosphor screen (vendor specification);  
For others: calculated absorption by the silicon crystal.

Compared to the hybrid pixel detectors, the SMART 1000 CCD has a much smaller pixel size (61 μm) and features a higher detector efficiency at higher X-ray energies (e.g. Mo-K<sub>α</sub> and Ag-K<sub>α</sub>). Disadvantages of the detector are its long readout time (10 s) and limited dynamic range. Furthermore, to reduce electronic noise the detector chip needs to be cooled down to -45 °C using a bulky cooling unit (NesLab RTE-I40). The hybrid pixel detectors have the benefit of a very short readout time (several ms) and a high dynamic range. The ability to discriminate

the detected photons based on their energy by means of adjustable thresholds makes these detectors practically noise-free. All hybrid pixel detectors in this study make use of Si photodiodes; to increase the sensitivity towards higher energy, different crystal thicknesses were chosen: 320, 500 and 1000  $\mu\text{m}$  for respectively the PILATUS 100K, XPAD S140 and PILATUS 200K cameras. To reduce the relative humidity around the active area, the PILATUS 100K and 200K detectors need to be flushed with a flow of dry air or  $\text{N}_2$ .

#### 2.2.4. Different MA-XRPD configurations

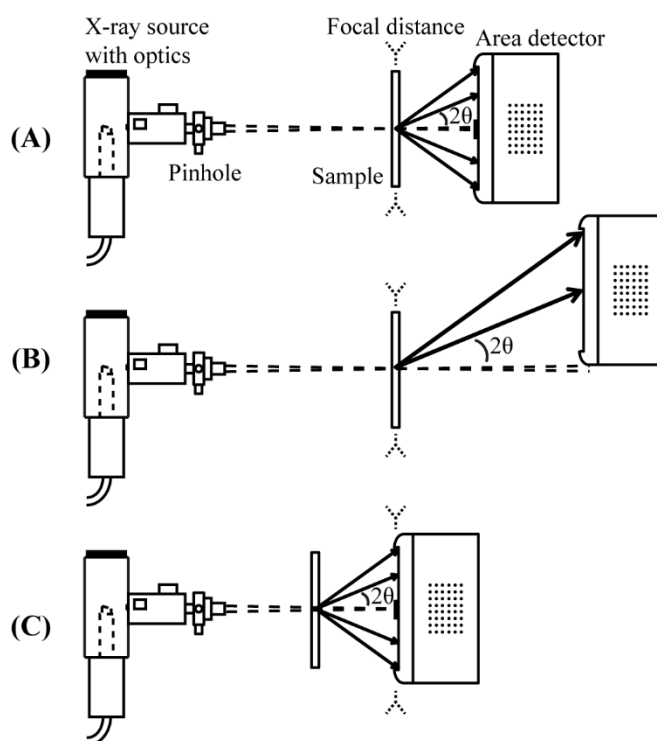


Figure 2-5. Schematic of the three geometries with different positions of the sample and/or area detector.

The X-ray sources and area detectors described in the previous sections were placed in three different geometries in which the position of the sample and/or

area detector is varied: (A) the sample is placed in the focal point and the detector is positioned in a centered position behind the sample, (B) the distance between sample and the detector is increased and the detector is moved out of the primary beam path and (C) the sample is placed closer to the source and the detector is positioned in the focal point (see Figure 2-5). In total 15 configurations are described in which a different combination between source, detector and/or geometry is used. For most configurations the distance between the sample and the area detector was chosen to capture a similar Q-range. An overview of the different configurations is given in Table 2-4.

**Table 2-4. Overview of the different configurations**

Configuration	Source and optic	Area Detector	Geometry	max. Q value (nm <sup>-1</sup> )	Sample-detector distance (cm)
1	Warrikhoff <sup>a</sup>	S 1000	A	33.5	7.8
2	Warrikhoff <sup>a</sup>	S 1000	B	41.3	13.0
3	Warrikhoff <sup>a</sup>	X S140	B	38.5	16.8
4	Warrikhoff <sup>a</sup>	P 100K	B	62.7	11.0
5	Warrikhoff <sup>a</sup>	P 200K	A	37.8	9.1
6	Warrikhoff <sup>a</sup>	P 200K	B	39.9	18.1
7	I $\mu$ S-Mo	S 1000	A	34.9	7.5
8	I $\mu$ S-Cu	P 200K	A	37.5	3.0
9	I $\mu$ S-Cu	P 200K	C	37.7	2.9
10	I $\mu$ S-Ag <sup>HB</sup>	P 200K	A	38.4	11.7
11	I $\mu$ S-Ag <sup>HB</sup>	P 200K	B	38.9	23.8
12	I $\mu$ S-Ag <sup>HB</sup>	P 200K	C	38.1	11.8
13	I $\mu$ S-Cu <sup>HB</sup>	P 200K	A	37.3	3.0
14	I $\mu$ S-Cu <sup>HB</sup>	P 200K	B	38.9	7.7
15	I $\mu$ S-Cu <sup>HB</sup>	P 200K	C	37.3	3.0

S: SMART; P: PILATUS; X: XPAD

<sup>a</sup> using IFD<sub>1</sub>.



### 2.2.5. Figures-of-merit

Several figures-of-merit were determined for the different X-ray source - detector combinations: spatial resolution, angular resolution, signal-to-noise ratio (SNR), the captured angular range ( $2\theta$  angles or  $Q$  values) and the time between consecutive acquisitions (dead time). The area detector influences the latter four figures-of-merit, while the X-ray source properties affect all with exception of the dead time.

The spatial resolution is limited by the X-ray spot size at the sample location and was determined using the wire or knife-edge procedure, see section 2.2.2.1.

The angular resolution and SNR were calculated using several diffraction measurements at different positions on a  $\text{LaB}_6$  standard reference powder with maximal source current and voltage for all configurations. After azimuthal integration, the background was estimated using either orthogonal polynomials or iterative peak stripping while a single Gaussian profile was used for modelling each reflection. The FWHM of the modelled reflections is used as an estimate of the angular resolution.

For determining the signal-to-noise ratio, the net peak area of the Gaussian used for the strongest reflection (110) of  $\text{LaB}_6$  was taken. The uncertainty on the net peak area was assumed to be much smaller than the local sample variation and was not included in the SNR calculation (see below). A window of six  $\sigma$  of the Gaussian was taken between reflection (100) and (110) at  $Q = 18.25 \text{ nm}^{-1}$  to estimate the background noise. The SNR was normalized to 1 second exposure time (see below).

The collected angular range was calculated for a primary beam impinging the center of each detector for geometries A and C and experimental values are given for geometry B.

***SNR determination***

The signal-to-noise ratio (SNR) is given by the ratio of the net peak area ( $S_p$ ) for a given reflection and the signal noise ( $N$ )

$$SNR = S_p / N$$

For point detectors, counting statistics are assumed so that the noise ( $N$ ) is estimated by the standard deviation ( $\sigma$ ) on the background signal ( $S_b$ ).

$$N = \sigma = \sqrt{S_b} \tag{Eq. 2-1}$$

Both the net peak area and the background signal increase linearly with time ( $t$ ) so that the SNR can be written in intensity rates ( $R$ ).

$$SNR = \frac{R_p t}{\sqrt{R_b t}} = \frac{R_p}{\sqrt{R_b}} \sqrt{t}$$

For area detectors the intensities are calculated by azimuthal integration so that Eq. 2-1 is not valid. The uncertainty on the background ( $s$ ) is estimated by XRDUA following error propagation during azimuthal integration of the diffraction images. Counting statistics are assumed for each detector pixel [23]. The signal noise is estimated from the uncertainty on the background signal for each diffractogram bin ( $i$ ).

$$N = b \sum_i s_i$$

for which  $b$  is the diffractogram bin width. The SNR for area detectors can therefore be expressed by

$$SNR = \frac{S_p}{b \sum_i s_i}$$

which is valid for photon counting detectors for which Poisson statistics apply. For CCD cameras this assumption is valid only if the time-independent electronic noise can be neglected (e.g. for high signals or long exposure times). Similarly to the background noise, the dark noise that arises from thermally generated electrons in the CCD chip also follows Poisson statistics.

### 2.2.6. Illuminated manuscript

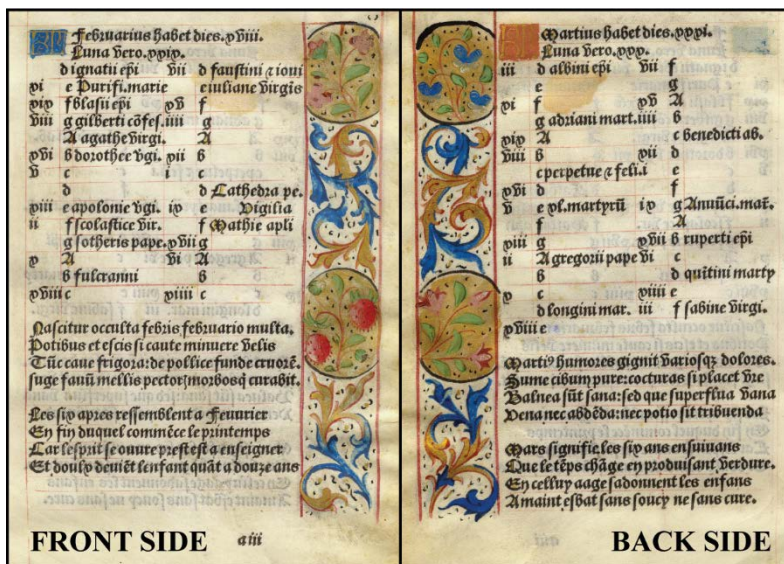


Figure 2-6. Photographs of the front and back side of the 15th/16th c. illuminated sheet of parchment.

The manuscript (private collection) is an excerpt from an illuminated 15<sup>th</sup>/16<sup>th</sup> century Book of Tides and features numerous decorations, see Figure 2-6. In black ink, a Latin text accompanied by a French translation covers most of the parchment. In the margin, colorful vegetal motifs such as strawberries and flowers were applied on both sides. In terms of pigments and materials used as well as its

painting style, this folio is very similar to late 15<sup>th</sup> century folios belonging to Books of Hours of North French/Flemish origin. Similar works are present in for example the Morgan Library and Museum, NYC (e.g., MS M.161 folio 23r, 47r and 80r; <http://www.themorgan.org/manuscript/77108> [Accessed 17 March 2018]) [24]. The illuminated manuscript has previously been analyzed with a portable Raman-X-ray instrument (PRAXIS) using combined  $\mu$ -Raman spectroscopy,  $\mu$ -XRF and synchrotron  $\mu$ -XRPD [25], as well as with 3D confocal XRF [26]. Throughout all these studies no visual change to the manuscript folio was noticeable.

### 2.2.7. MA-XRPD data processing

The XRDUA software package was used for processing of the diffraction data and visualization of the crystalline phase distributions [27]. A detailed overview of the functionality of the XRDUA imaging software is given elsewhere [28]. During a scanning experiment the diffraction data can be analyzed in real-time through regions-of-interest (so-called explorative processing) which provide immediate information about the crystalline contents and their spatial distribution without prior knowledge of the sample. After the automated azimuthal integration process whole pattern fitting was performed on the one-dimensional data. A Rietveld model containing all identified crystalline compounds (summation index  $i$ ) was constructed using crystal structures obtained from the American Mineralogist Crystal Structure Database [29] or from literature:

$$I_{\text{Riet}}(2\theta) = I_{\text{bkg}}(2\theta) + \sum_i S_i \sum_H F_{iH}^2 C_{iH} \Omega_i(2\theta - 2\theta_{iH})$$

where  $S_i$  denotes the total peak intensity scaling factor of each phase present,  $F_{iH}$  denotes the structure factor and  $C_{iH}$  the part of the Lorentz-polarization factor not removed during azimuthal integration. A Gaussian peak shape ( $\Omega_i$ ) was used.

Both the  $K_{\alpha 1}$  and  $K_{\alpha 2}$  peak contributions to the diffraction patterns were taken into account. The relative peak positions and intensities of each individual compound remained fixed during least squares fitting, while the width of the diffraction signals was modelled using only the theta-independent part of the Cagliotti peak width function. In this way refined values for the displacement, scaling and width parameters for each compound in each data point were obtained. Several constraints were set on the displacement and width parameters to avoid solutions without physical meaning. The background contribution ( $I_{bkg}$ ) was modelled using a strip function. Plotting the scaling parameter as a grey scale value yields the MA-XRPD distribution maps of the crystalline paint components [28].

For comparing XRPD data acquired at different wavelengths, it is more convenient to express the diffracted intensity as a function of the energy-independent scattering vector ( $Q$ ) instead of the typically used  $2\theta$ -scale.  $Q$ -values given throughout this work represent the momentum transfer (i.e. the modulus of the scattering vector given by  $Q = 2\pi/d = 4\pi \sin(\theta)/\lambda$ ). The evaluation of the X-ray fluorescence spectral data was performed with the PyMCA package [30].

## 2.3. RESULTS AND DISCUSSION

### 2.3.1. Angular resolution

A high angular resolution is critical to detect small changes in the lattice parameters of the crystal structures or for unambiguously identifying unknown compounds in a complex mixture.

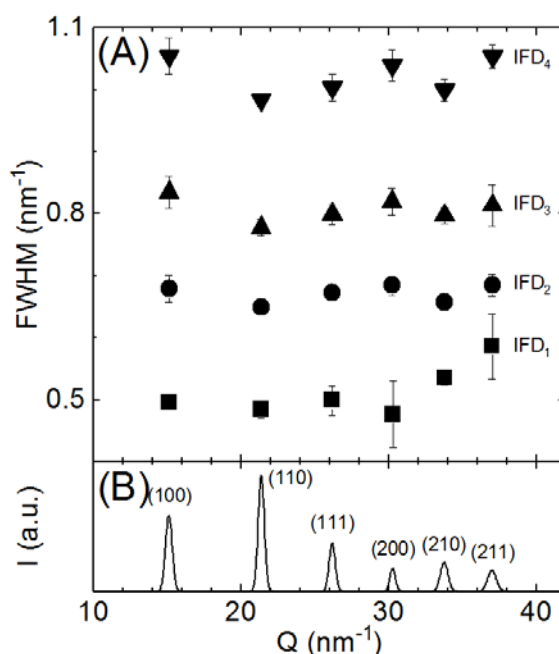


Figure 2-7. (A) Diffraction peak FWHM versus momentum transfer ( $Q$ ) for six  $\text{LaB}_6$  reflections at different IFD for configuration I. Results are the averages of five to ten measurements with the standard deviations ( $1\sigma$ ) shown as error bars. (B) Averaged X-ray diffractogram of the  $\text{LaB}_6$  reflections used in (A).

Depending on the input focal distance that is used for the polycapillary lens with the Warrikhoff microsource, an X-ray beam with a different focal spot size and divergence is formed, as was shown in Table 2-1. A short distance between the lens and the source (IFD<sub>1</sub>) results in a decreased spot size and divergence, while

sacrificing a significant portion of the beam intensity. However, as can be seen in Figure 2-7, changing the distance between the source and lens from IFD<sub>4</sub> to IFD<sub>1</sub> for configuration 1 also greatly improves the angular resolution from about 0.98 to 0.48 nm<sup>-1</sup> FWHM for the (110) reflection of the LaB<sub>6</sub> standard. Therefore, only results from the Warrickhoff X-ray source positioned at IFD<sub>1</sub> relative to the lens will be taken into account for the discussion of the different configurations.

The angular resolution of the 15 different configurations is shown in Figure 2-8 for two LaB<sub>6</sub> reflections, (100) and (211), positioned at the edge of the captured Q-range. These results show that the same geometry does not provide the best angular resolution for each source-detector combination. Geometry A always provides broader diffraction signals compared to B and C. The increase in sample-to-detector distance for geometry B or the intrinsic focusing of the diffraction signals on the detector surface in geometry C improves the angular resolution for these geometries.

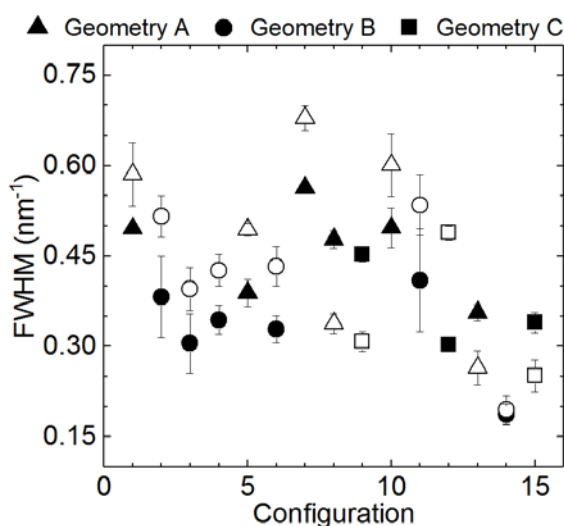


Figure 2-8. Diffraction peak FWHM for two LaB<sub>6</sub> reflections; (100) (filled symbols) and (211) (empty symbols) for the different configurations. The error bars represent the standard deviation (1s) for 5 to 16 measurements.

Although the SMART 1000 CCD detector has a much smaller pixel size compared to the different hybrid detectors, the point spread function (PSF) of the CCD causes a broadening of the diffraction signals which can be observed when comparing configurations 1 and 5 (geometry A) or 2, 3, 4 and 6 (geometry B). Since the difference between the PILATUS 100K and 200K in this study lies primarily in the size of the active area and the thickness of the silicon photodiodes, no significant change is expected between the peak widths obtained with both detectors (configurations 4 and 6). The smaller pixel size of 130  $\mu\text{m}$  for the XPAD SI40 results in the best angular resolution (0.31 – 0.40  $\text{nm}^{-1}$ ) for all configurations employing the Warrikhoff X-ray source (configurations 1-6).

The angular resolution of the  $\text{I}\mu\text{S-Ag}^{\text{HB}}$  source benefits from the increased distance between sample and detector in geometry B (configuration 11) compared to A (configuration 10), resp. 0.41 – 0.53  $\text{nm}^{-1}$  and 0.48 – 0.60  $\text{nm}^{-1}$ , but achieves the highest resolution in geometry C (configuration 12) with an improvement of the FWHM to 0.30 – 0.49  $\text{nm}^{-1}$ . The increase in peak FWHM values for reflection (211) compared to (100) at higher scattering vectors is mainly ascribed to peak splitting coming from  $\text{Ag-K}_{\alpha 1}$  and  $\text{K}_{\alpha 2}$  contributions (see Figure 2-9).

On the other hand, the  $\text{I}\mu\text{S-Cu}^{\text{HB}}$  source shows a minor difference between geometry A and C (reps. 0.36 – 0.26  $\text{nm}^{-1}$  and 0.34 – 0.25  $\text{nm}^{-1}$ ), but a much better resolution for geometry B with FWHM values around 0.19  $\text{nm}^{-1}$  over the entire Q-range (configurations 13-15). Furthermore, the small spot size, low divergence and long wavelength of the  $\text{I}\mu\text{S-Cu}^{\text{HB}}$  source yields the best angular resolution for all tested configurations and geometries. The spot size of  $\text{I}\mu\text{S-Cu}$  is twice as large compared to  $\text{I}\mu\text{S-Cu}^{\text{HB}}$  and negatively impacts the resolution (configurations 8 and 9). A similar improvement of the angular resolution for geometry B (as seen for  $\text{I}\mu\text{S-Cu}^{\text{HB}}$ , configuration 14) is expected for this source.



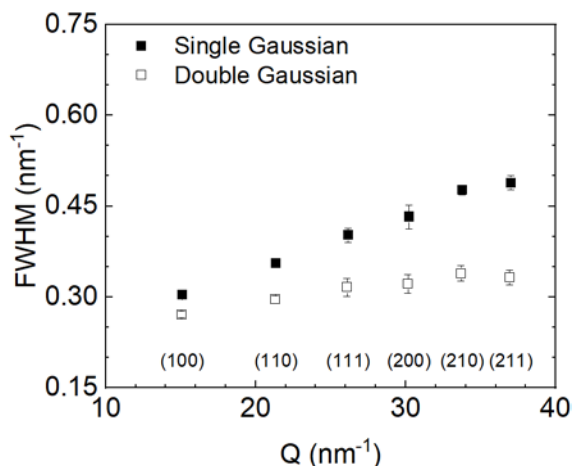


Figure 2-9. FWHM values in function of the momentum transfer ( $Q$ ) for different  $\text{LaB}_6$  reflections for configuration 12. Each reflection is modelled using a single Gaussian (Filled boxes), or using two Gaussians representing the  $K_{\alpha 1}$  and  $K_{\alpha 2}$  contribution (Empty boxes). The same FWHM value was used for the two Gaussians modelling  $K_{\alpha 1}$  and  $K_{\alpha 2}$ . The error bars represent the standard deviation (1s) for 10 measurements. The Miller indices for the different reflections are given.

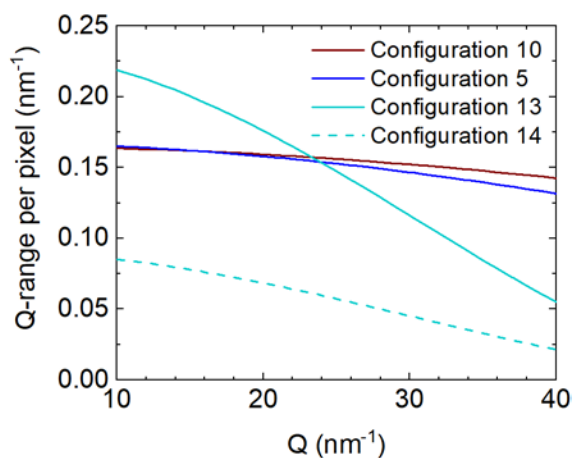


Figure 2-10. Calculated Q-range covered by a single detector pixel in function of the momentum transfer ( $Q$ ) for different configurations.

The decrease in FWHM values with increasing momentum transfer for configurations using Cu-K $\alpha$  results from the decreasing Q-range that is captured by the individual detector pixels. Indeed, a single detector pixel at reflection (100) covers a Q-range of 0.20 nm $^{-1}$ , while a pixel for reflection (211) covers a Q-range of 0.07 nm $^{-1}$ . This effect is much less pronounced when a higher energy or a longer sample to detector distance is used (see Figure 2-10).

The I $\mu$ S-Mo source combined with the SMART 1000 CCD (configuration 7) gives rise to the largest peak FWHM values. This is expected as geometry A continuously yields the worst angular resolution for all configurations while the PSF of the CCD camera further broadens the diffraction signals.

### 2.3.2. Spatial resolution

The spatial resolution of the MA-XRF/MA-XRPD system is a measure of the smallest features that can be distinguished in a sample. In geometries A and B the sample is positioned in the focal point of the X-ray optic, resulting in the highest spatial resolution as shown in Figure 2-11; next to the optic employed, this is mainly determined by the spot size of the X-ray source. With the sources I $\mu$ S-Mo and I $\mu$ S-Ag<sup>HB</sup> a spatial resolution of around 110  $\mu$ m can be obtained (configurations 7, 10, 11 in Table 2-4). The I $\mu$ S-Cu<sup>HB</sup> source has a slightly larger spot size of 140  $\mu$ m (configurations 13-14), while the I $\mu$ S-Cu source produces a focal spot of 310  $\mu$ m (configuration 8). The configurations with the Warrikhoff X-ray source deliver a spatial resolution of around 200  $\mu$ m (configurations 1-6). In geometry C the detector rather than the sample is positioned in the beam focus with the sample placed closer to the source. This results in a lower spatial resolution. For configuration 12, using the I $\mu$ S-Ag<sup>HB</sup>, the sample is positioned 11.8 cm out-of-focus, increasing the beam footprint to around 430  $\mu$ m. For configurations 9 and 15 the low Cu-K $\alpha$  energy requires that only a limited change in the sample position between geometries A and C is needed. This results in a

small change in spot size, respectively to 340 and 160  $\mu\text{m}$  for  $\text{I}\mu\text{S-Cu}$  and  $\text{I}\mu\text{S-Cu}^{\text{HB}}$ . For all configurations with the Warrickhoff source geometry C is not possible because of the small OFD of the polycapillary lens (OFD = 4.0 (l) cm at  $\text{IFD}_1$ ).

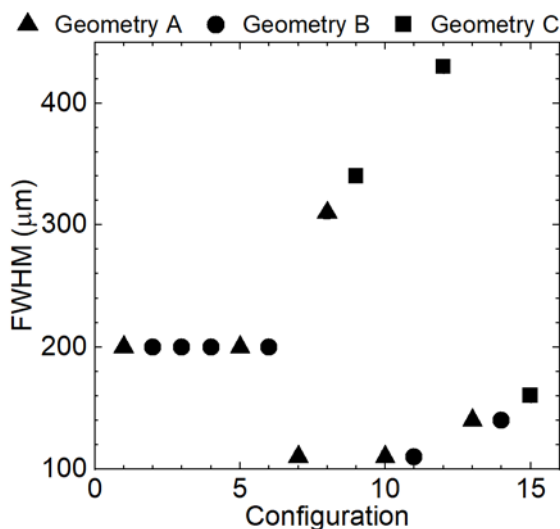


Figure 2-11 Beam footprints for the different configurations. The errors bars representing the standard deviation (1s) of three measurements is smaller than the symbols used.

### 2.3.3. Signal-to-noise ratio (SNR)

The dwell time per point directly affects the total scan time and should be kept as short as possible so that areas can be imaged in a reasonable time, but also to limit the radiation dose that the examined sample is exposed to. On the other hand, reducing the dwell time is only meaningful if the diffraction information remains distinguishable from the background noise. The signal-to-noise ratios have been normalized to 1 second to facilitate the comparison of the different configurations. For the hybrid photon counting detectors, the SNR was found to be proportional to the square root of the exposure time (in analogy to point detectors). For the SMART 1000 CCD detector the  $\text{SNR} \propto t^{0.6}$ , see Figure 2-12.

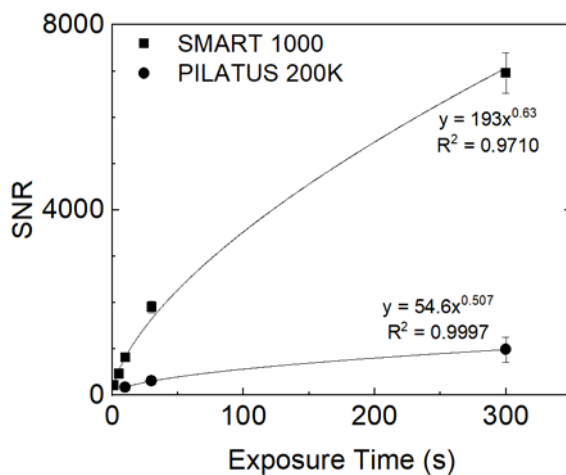


Figure 2-12. SNR for 2D XRPD in function of the exposure time calculated for the (110) reflection of  $\text{LaB}_6$  with configurations 7 and 12. The error bars represent the standard deviation (1s) for five (configuration 7, SMART 1000) or ten (configuration 12, PILATUS 200K) measurements.

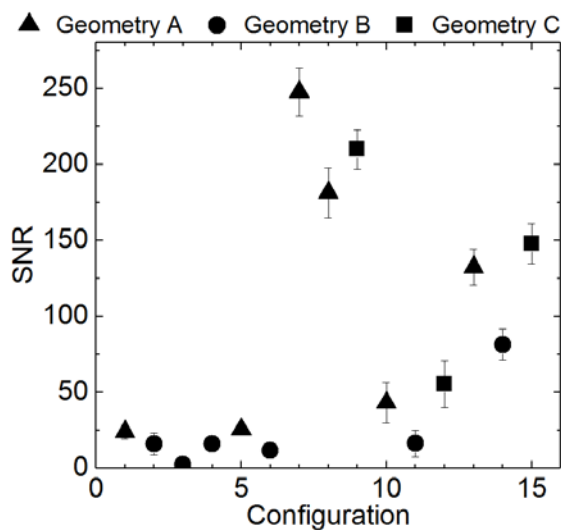


Figure 2-13. Signal-to-noise ratio normalized to 1 s exposure time obtained with the different configurations. The error bars represent the standard deviation (1s) for 5 to 16 measurements.

The SNR normalized to one second exposure time for the different configurations are shown in Figure 2-13. The low flux delivered onto the sample by placing the polycapillary lens at IFD<sub>1</sub> for the Warrikhoff source results in a low SNR for all configurations (1-6). For the configurations with the Incoatec sources (8-15) the SNR improves with increasing flux.

Although the I $\mu$ S-Mo and I $\mu$ S-Ag<sup>HB</sup> sources have a comparable flux, the SNR is almost six times higher for the former when the same geometry is used (configuration 7 and 10). Since the SMART 1000 CCD is optimized for detecting Mo-K $\alpha$  photons and one X-ray photon gives rise to the formation of several tens of electron-hole pairs (~40 electron-hole pairs per Mo-K $\alpha$  photon), the uncertainty on the obtained intensities is reduced. Similarly, configuration 1 has the highest SNR compared to the other Warrikhoff source configurations (3-6) that make use of the hybrid detectors.

The limited detection efficiency for the high Ag-K $\alpha$  energy, even for a 1 mm thick active Si layer, combined with the relatively low flux reduces the SNR for configurations 10-12 even more. For configurations 4 and 6 an increase in SNR would be expected due to the two times higher detection efficiency of the 1 mm thick silicon layer of the PILATUS 200K compared to the 100K detector. The deviant behavior of these configurations could be due to difficult alignment of the polycapillary. For geometry B the SNR is always lower compared to A and C. The larger air absorption and more importantly the smaller fractions of the diffraction cones that are intersected by the detector increase the uncertainties on the number of counted photons. For geometries A and C, complete Debye rings are recorded up to  $Q \approx 38 \text{ nm}^{-1}$ . In this respect it becomes clear that detectors with a large active area will increase the SNR for longer scattering vectors as a larger fraction of their diffraction cones can be captured.

Although the SNR ratios shown in Figure 2-13 provide a meaningful insight into the advantages of one configuration over the other, the SNR for the different sources will change dramatically depending on the type of sample. More intense Cu sources will be favored for thin samples or samples with limited X-ray absorption, while for highly attenuating or thick materials, selecting the higher Mo-K $\alpha$  or Ag-K $\alpha$  energy will be a more suited approach.

### **2.3.4. Angular range**

The active area of a 2D detector is of importance for capturing a large range of diffraction signals simultaneously. This Q-range depends on the distance and position of the detector to the sample for a specific excitation energy. In most configurations the position of the detector was chosen so as to keep a similar Q-range, independent of the source-detector combination or geometry, with a maximum momentum transfer of around 38 nm<sup>-1</sup> (see Table 2-4). In the authors' experience it is not necessary to extend this Q-range further as the multitude of reflections at larger scattering vectors leads to peak overlap and for investigations related to paint materials, a distinction between most common pigments can be made at smaller Q values.

### **2.3.5. Dead time**

In addition to the exposure time, there is also a period in between measurements during which no acquisitions can be made (called dead time) but which is required for detector readout and motor movements. The dead time is added on top of the acquisition time for each recorded position, sometimes greatly extending the total scanning time. For the scanning setups employing the SMART 1000 CCD detector, its readout time of 10 s represents a major limiting factor. For configurations using the hybrid detectors, the dead time is determined by the motor movements that typically take 2.5 s per start-stop operation for the imaging

experiments performed in this work. A significant reduction in dead time is possible by employing a continuous movement rather than a start-stop movement of the main motor stage during scanning (so-called sweep mode).

From the figures-of-merit discussed above it becomes clear that configuration 9 is ideally suited for illustrating the potential of MA-XRF/MA-XRPD scanning on the 15<sup>th</sup>/16<sup>th</sup> c. manuscript. Indeed, for weakly attenuating samples the high SNR and short dead time of this configuration allow for fast imaging of macroscopic areas. Although this configuration features a relatively coarse spatial resolution, this is still more than adequate for visualizing fine decorative details. For more absorbing artefacts or when the angular resolution becomes crucial, respectively configuration 12 or 14 can be used.

## 2.4. CASE STUDY

### 2.4.1. Illuminated 15<sup>th</sup>/16<sup>th</sup> century manuscript

To illustrate the capabilities of a combined MA-XRF/MA-XRPD scanning system, elemental and compound-specific distributions were simultaneously collected on a 15<sup>th</sup>/16<sup>th</sup> century illuminated parchment. The entire margin decoration was imaged with configuration 9 over a period of 8.4 hours (map size:  $137.6 \times 22.8 \text{ mm}^2$ ; pixel size:  $0.4 \times 0.4 \text{ mm}^2$ ; dwell time per point: 0.2 s), while a small detail was imaged in high detail with configuration 11 over a period of 20.6 hours (map size:  $8 \times 8 \text{ mm}^2$ ; pixel size:  $0.1 \times 0.1 \text{ mm}^2$ ; dwell time per point: 10 s). Twelve crystalline species were revealed to be present, as shown in Figure 2-14.

From the photographs it is clear that the gold paint is present on both the front and back side of the sheet of parchment. This is reflected in the gold MA-XRPD distribution showing the cartouches and the gold used for the scrollwork. The Au-M MA-XRF map on the other hand only shows the gold that is used on the front side, i.e. the side of the XRF detector. The use of a monochromatic Cu-K $\alpha$  excitation energy will only give rise to low energy M-lines of heavy elements such as Au, Hg and Pb. Higher energy L-lines that usually are not so strongly influenced by absorption effects of overlaying layers are not emitted. For the more energetic Fe-K lines a contribution from the back side of the manuscript to the Fe-K MA-XRF map is detected (Figure 2-14). A strong Ca-K XRF signal was found throughout most of the manuscript; as visualized with MA-XRPD, this corresponds to calcite ( $\text{CaCO}_3$ ) and gypsum ( $\text{CaSO}_4 \cdot 2\text{H}_2\text{O}$ ). The presence of calcite originates from chalk which was abundantly used during the preparation of parchment. Gypsum has presumably been used as a substrate for a not yet identified organic pink colorant (e.g. in the pink flowers).



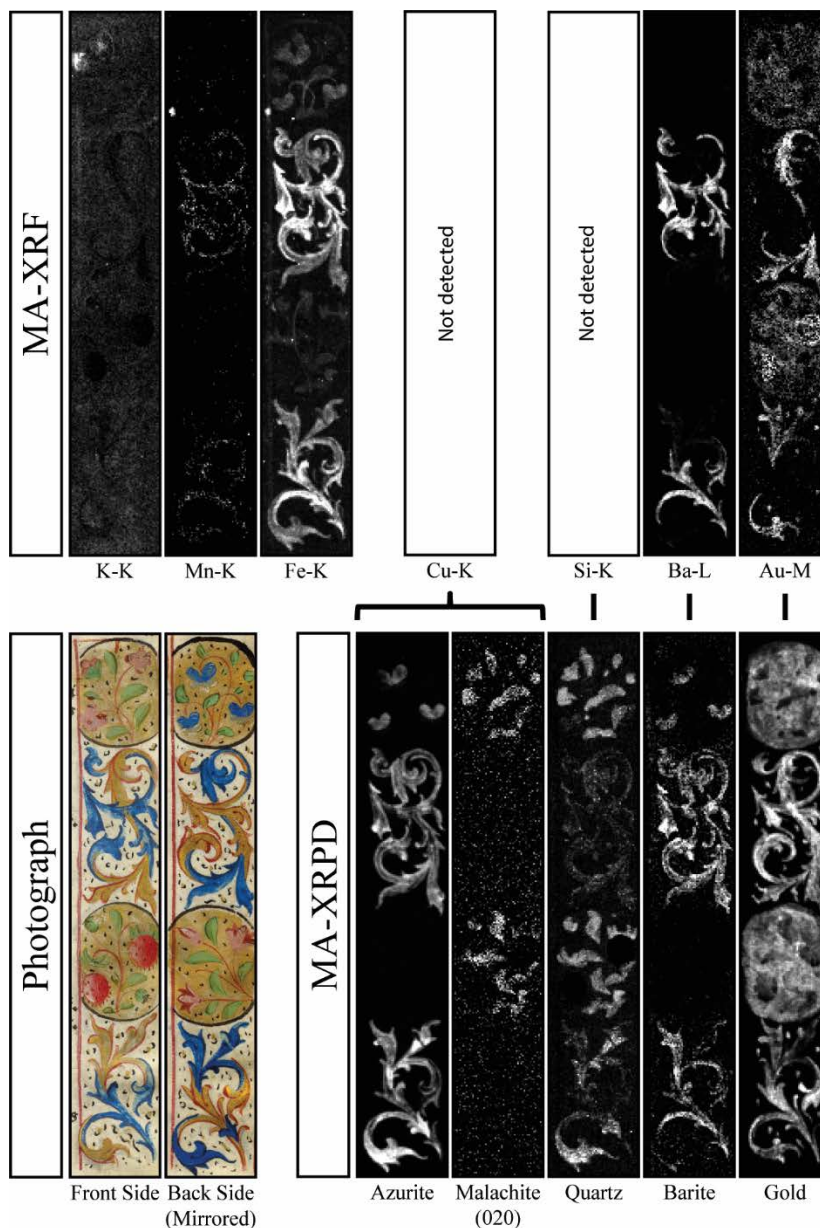


Figure 2-14. (bottom left) Photographs of the scanned region for both the front and back side of the illuminated manuscript. Element-specific (top row, MA-XRF) and phase-specific (bottom row, MA-XRPD) distribution images acquired with configuration 9. Whiter tones indicate a higher scaling parameter (MA-XRPD) or fluorescence intensity (MA-XRF). Caption continues on the next page.

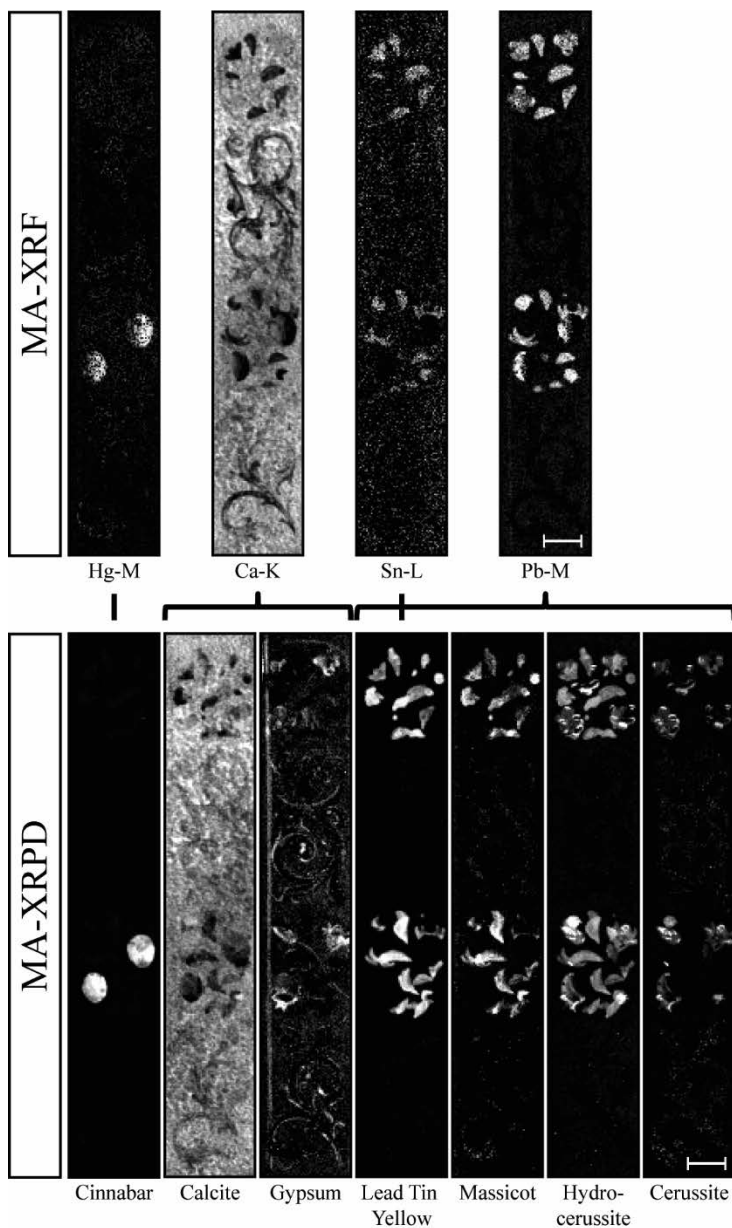


Figure 2-14. Continued. Azurite:  $2\text{CuCO}_3 \cdot \text{Cu}(\text{OH})_2$ ; malachite:  $\text{CuCO}_3 \cdot \text{Cu}(\text{OH})_2$ ; quartz:  $\text{SiO}_2$ ; barite:  $\text{BaSO}_4$ ; gold:  $\text{Au}^0$ ; cinnabar:  $\text{HgS}$ ; calcite:  $\text{CaCO}_3$ ; gypsum:  $\text{CaSO}_4 \cdot 2\text{H}_2\text{O}$ ; lead tin yellow:  $\text{Pb}_2\text{SnO}_4$ ; massicot:  $\text{o-PbO}$ ; hydrocerussite:  $2\text{PbCO}_3 \cdot \text{Pb}(\text{OH})_2$  and cerussite:  $\text{PbCO}_3$ . Map size:  $137.6 \times 22.8 \text{ mm}^2$ ; pixel size:  $0.4 \times 0.4 \text{ mm}^2$ ; dwell time per point: 0.2 s.

The high specificity of the MA-XRPD technique allows for the identification of four Pb-containing crystalline compounds: lead tin yellow type I, massicot, hydrocerussite and cerussite. From the Sn-L and Pb-M MA-XRF distributions an indirect identification of lead tin yellow can be made, however the distinction between type I ( $\text{Pb}_2\text{SnO}_4$ ) and type II ( $\text{Pb}(\text{Si},\text{Sn})\text{O}_3$ ) based on XRF data alone cannot be made. A similar problem arises for hydrocerussite ( $2\text{PbCO}_3 \cdot \text{Pb}(\text{OH})_2$ ), cerussite ( $\text{PbCO}_3$ ) and massicot ( $\text{o-PbO}$ ), all of which will contribute to the Pb-M MA-XRF distribution. MA-XRPD unambiguously identified lead tin yellow type I to be present in the manuscript, co-localized with massicot and lead white in the green leaves throughout all four cartouches. It is noteworthy that the lead white consists solely of hydrocerussite. Although lead tin yellow type I, besides Naples yellow ( $\text{Pb}_2\text{Sb}_2\text{O}_6(\text{O},\text{OH})$ ) and orpiment ( $\text{As}_2\text{S}_3$ ), was a commonly used yellow in manuscripts, the presence of massicot is noteworthy (see Figure 2-15).

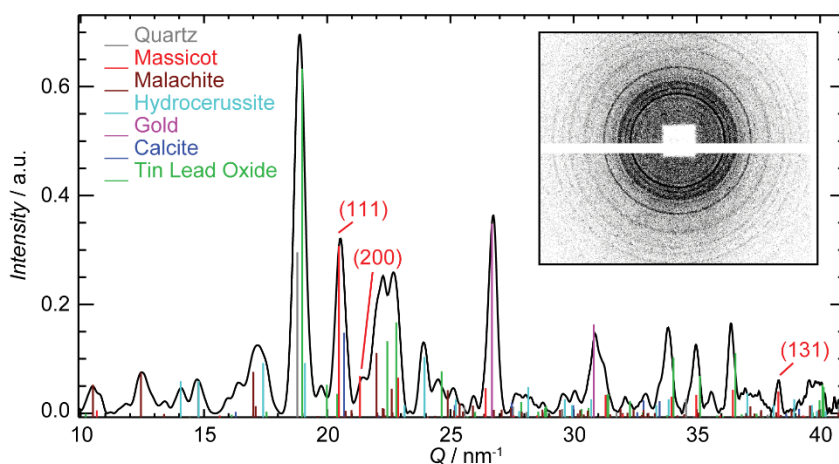


Figure 2-15. X-ray diffractogram of a single point located in the green leaves collected with configuration 9 using an exposure time of 200 ms. Selected reflections used for the identification of massicot ( $\text{o-PbO}$ ) have been highlighted.

Massicot, the yellow lead(II) oxide, is mostly found as an impurity to natural or synthesized red lead [31] but has very rarely been used as a yellow pigment on

manuscripts or paintings [32]. PbO, together with SnO<sub>2</sub>, has also been detected when lead tin yellow type I is synthesized following historical recipes, although it is unclear if this is litharge (*t*-PbO) or massicot (*o*-PbO) [33]. A different type of lead white, containing both cerussite and hydrocerussite was used for the pink flowers and the white highlights in the cartouches. For the highlights on the strawberries, calcite was added as an extender to the same type of lead white (see Figure 2-16).

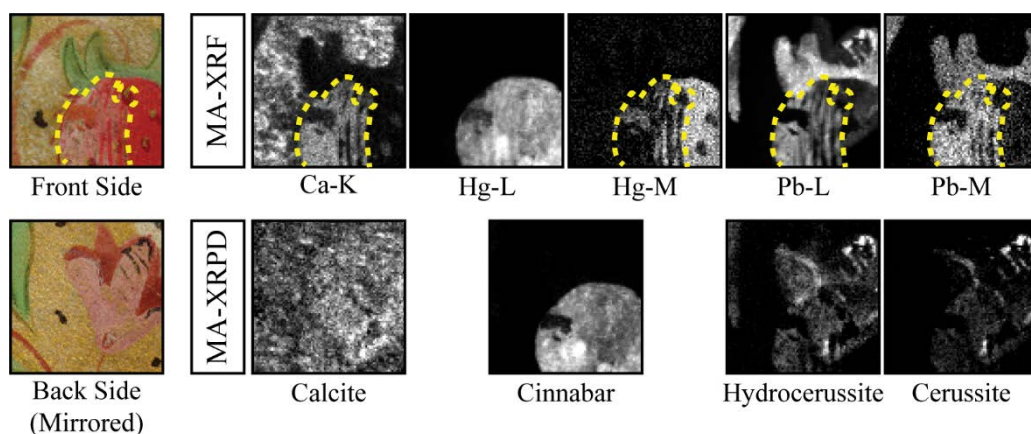


Figure 2-16. (left) Photographs of the scanned strawberry detail and the corresponding area of the back side of the illuminated manuscript. Element-specific (top row, MA-XRF) and compound-specific (bottom row, MA-XRPD) distribution images acquired with configuration II. Whiter tones indicate a higher scaling factor (MA-XRPD) or fluorescence intensity (MA-XRF). The yellow dashed area indicates the white highlight on the strawberry. Map size:  $8 \times 8 \text{ mm}^2$ ; pixel size:  $0.1 \times 0.1 \text{ mm}^2$ ; dwell time per point: 10 s; total scan time: 20.6 h.

The Ca-K signal visible on the left side of the strawberry in Figure 2-16 (yellow dashed line) cannot originate from the chalk used during preparation of the parchment as this would be absorbed by the overlaying vermilion used for the red color. Indeed, the right side of the strawberry, not covered by the white

highlight, shows a strong absorption of the emitted Ca-K fluorescence. This indicates that calcite will most likely have been added as an extender to the lead white used for the white highlight [34]. This distinction in the different usage of chalk is not possible to make based on the calcite MA-XRPD distribution as the information of the two chalk layers is superimposed in the final image.

Two copper carbonates, malachite ( $\text{CuCO}_3 \cdot \text{Cu}(\text{OH})_2$ ) and azurite ( $2\text{CuCO}_3 \cdot \text{Cu}(\text{OH})_2$ ), were used throughout the decorations. No Cu-K MA-XRF distribution image could be obtained because of the too low excitation energy of configuration 9 (Cu- $K_\alpha$ ). In order to effectively separate the diffraction peaks of malachite from those of cinnabar (HgS), it was necessary to map the intensity of the isolated malachite (020) reflection (Figure 2-17). This shows malachite to be only present in the green leaves (as shown in Figure 2-14).

Indeed, the most intense reflection of malachite ( $\bar{2}01$ ) is completely covered by the strong HgS reflection ( $10\bar{2}$ ) (see Figure 2-17C). The distribution image obtained with whole pattern fitting therefore suggests that malachite is present in the strawberries (Figure 2-17A). The diffractogram taken in a single point in one of the green leaves shows two isolated reflections of malachite: (020) and (120) (Figure 2-17D). The latter is however completely overlapped with several azurite reflections ((002), (011) and (100), not shown). A more accurate distribution of malachite can therefore be obtained by using only the isolated malachite (020) reflection (Figure 2-17B).

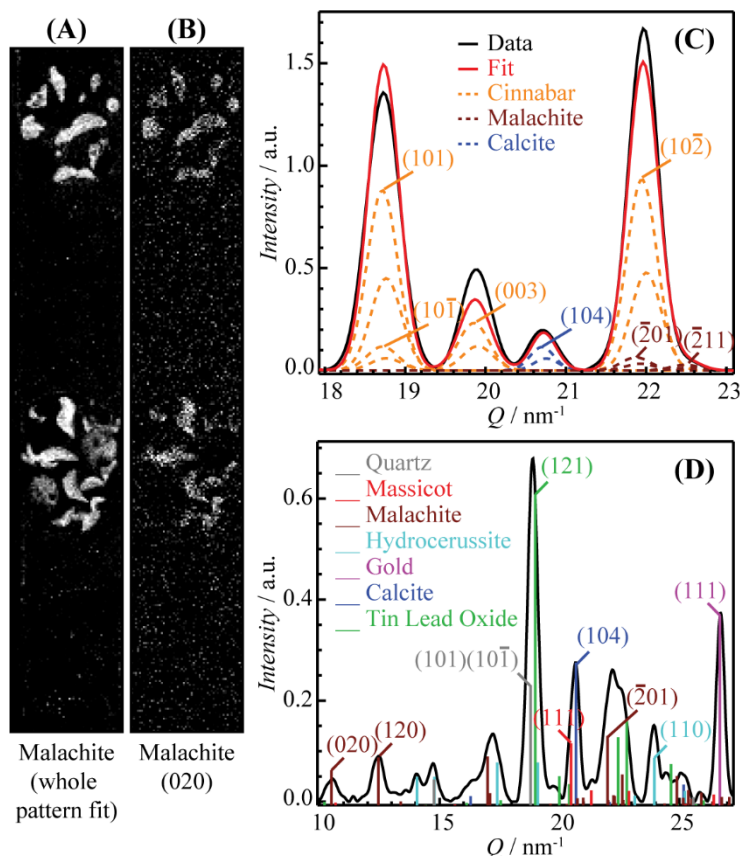


Figure 2-17. Phase-specific distribution of malachite obtained with (A) whole pattern fitting and (B) using only the isolated malachite (020) reflection. Whiter tones indicate a higher intensity. (C) Diffraction pattern of a selected  $Q$ -range showing the overlap between the strongest reflection of malachite ( $\bar{2}01$ ) and an intense cinnabar reflection ( $10\bar{2}$ ). The contributions of the different compounds to the fit are shown by the dashed curves. The Miller indices for the  $K_{\text{el}}$  reflections are given. (D) Diffraction pattern of a single pixel located in one of the green leaves showing the (020) reflection of malachite collected with configuration 9 and an exposure time of 200 ms. The Miller index of a characteristic reflection for each phase is shown.

The second copper carbonate, azurite, was used for the blue color of the decorative scrollwork and the blue flowers in one of the top cartouches as can be

seen in the azurite MA-XRPD map in Figure 2-14. Azurite is a frequently used blue pigment in European painting [35]. The pigment is of mineralogical origin and is therefore often intermixed with impurities that can be retained during the refinement process. Some of the more common impurities of azurite are malachite, cuprite, and the iron oxides hematite and goethite [36,37]. Although the Fe-K MA-XRF distribution (Figure 2-14) closely follows the azurite MA-XRPD distribution, no evidence for hematite or goethite could be found with diffraction. The limited sensitivity of XRPD compared to XRF may be the cause of this. No cuprite and possibly only some traces of malachite are found to be present in the azurite-rich areas.

Next to the common impurities also the presence of unusual crystallites associated with azurite are of interest in provenance studies. In this case, both barite and quartz are found together with azurite, see Figure 2-18. The Ba-L MA-XRF distribution is clearly linked to the blue color present on the front side of the parchment while the barite MA-XRPD map correlates very well to the azurite distribution. Other studies have reported barite as an impurity for azurite in paintings [38] and illuminated manuscripts [39,40]. Although barium sulfate has also been used as an artist's pigment, its earliest occurrence as a pigment was not before 1783 [41].

Quartz ( $\text{SiO}_2$ ), a less common impurity for azurite [36,39], shows some correlation with the azurite distribution (see quartz MA-XRPD), but also appears at first sight, to be strongly linked to the green pigment. However, a more detailed consideration reveals an unresolved overlap between the XRPD signals of  $\text{SiO}_2$  and  $\text{Pb}_2\text{SnO}_4$  (see Figure 2-17D). Unfortunately, there is no isolated XRPD reflection for quartz that can be used to obtain an artefact-free distribution.

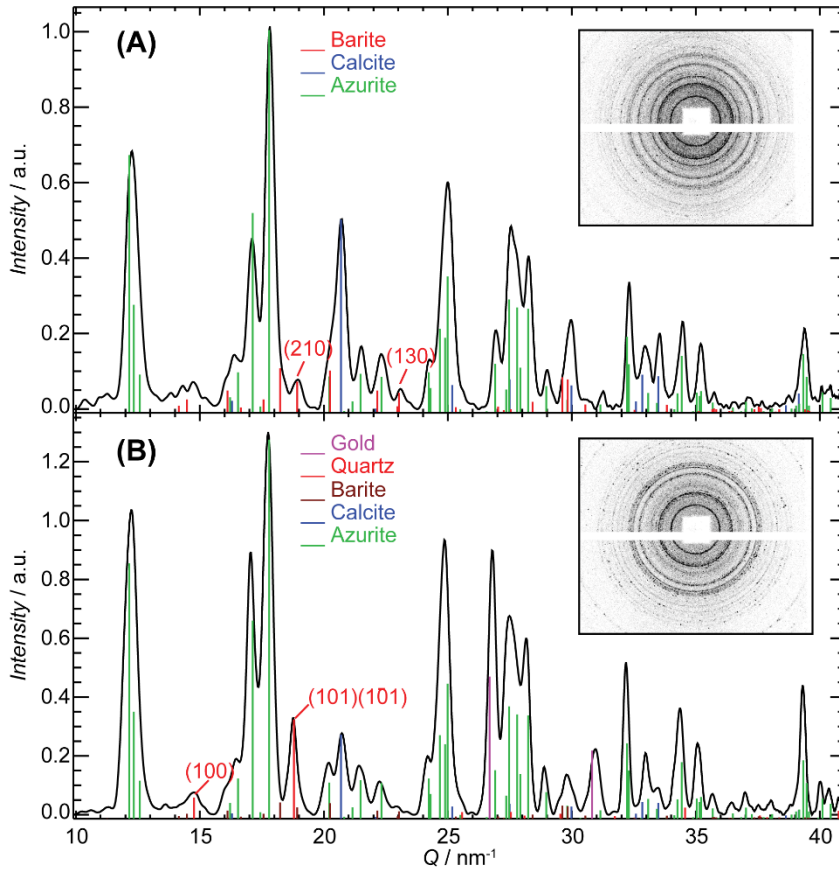


Figure 2-18. X-ray diffractogram of a single point located in the blue scrollwork collected with configuration 9 using an exposure time of 200 ms. Selected reflections used for the identification of (A) barite ( $\text{BaSO}_4$ ) and (B) quartz ( $\text{SiO}_2$ ) have been highlighted.



## 2.5. CONCLUSIONS

The capabilities of combined MA-XRF/MA-XRPD imaging using laboratory instrumentation have been demonstrated on a sheet of illuminated parchment while employing a short dwell time of only 200 ms per point. A large array of crystalline materials was successfully identified and their spatial distribution visualized in a noninvasive manner, providing valuable information on the artistic techniques and materials employed. Not only the different instrumentation (X-ray source, optic and area detector) but also the geometry has an important impact on the performance of MA-XRPD systems. All configurations show different (dis)advantages and the instrument best suited for a specific analysis will depend on the experimental requirements.

The highly-specific distributions obtained with MA-XRPD greatly complement MA-XRF images of the same artistic artefact. However, care should be taken with the interpretation of the MA-XRPD images since overlap of diffraction signals, especially in complex mixtures, can result in incorrect distributions. While the sampling depth for MA-XRF strongly depends on the emitted fluorescence energy and the presence/absence of overlaying layers, for MA-XRPD in transmission mode, information is obtained from all layers as the X-ray beam penetrates the entire layer structure of the manuscript. On the one hand the information present in the compound-specific distributions is therefore much less hampered by absorption from covering layers. On the other hand, a superimposed image from crystalline compounds present on both sides of the manuscript will be obtained, making interpretation of the images sometimes difficult. This aspect is addressed in greater detail in Chapter 5.

An important limitation of the discussed MA-XRPD systems is the restriction on the type of sample that can be analyzed. In transmission mode, the X-ray beam

has to penetrate the entire object which imposes limitations on the thickness of the various covering layers or the type of substrate material that can be present. Furthermore, the weight of the entire object needs to be supported by the motorized stages during the scanning operation, excluding panel and large canvas paintings. Since information is mostly limited to inorganic materials complementary methods that probe organic species such as MA-rFTIR and hyperspectral imaging are required to get a more comprehensive view of painted artworks. Nonetheless MA-XRPD using laboratory instrumentation holds a promising future and the recent efforts that were undertaken to construct a mobile MA-XRPD system for on-site examination of (essentially) flat art objects are illustrated in Chapter 3.

### **ACKNOWLEDGMENTS**

The authors thank the persons involved at Incoatec GmbH, imXPAD SAS and Dectris Ltd. for loaning us some of their products over the past years. We acknowledge financial support from BELSPO (Brussels) S2-ART, the NWO (The Hague) Science4Arts ‘ReVisRembrandt’ project and GOA Project Solarpaint (University of Antwerp Research Council).

## REFERENCES

- [1] Dik, J.; Janssens, K.; Van Der Snickt, G.; van der Loeff, L.; Rickers, K.; Cotte, M. *Anal. Chem.* **2008**, *80*, 6436-6442.
- [2] Alfeld, M.; Janssens, K.; Rickers, K.; Thijsse, B.; Dik, J. *Zeitschrift für Kunstgeschichte und Konservierung* **2011**, *25*, 157-163.
- [3] Alfeld, M.; Van der Snickt, G.; Vanmeert, F.; Janssens, K.; Dik, J.; Appel, K.; van der Loeff, L.; Chavannes, M.; Meedendorp, T.; Hendriks, E. *Appl. Phys. A: Mater. Sci. Process.* **2013**, *III*, 165-175.
- [4] Alfeld, M.; Janssens, K.; Dik, J.; de Nolf, W.; van der Snickt, G. *J. Anal. At. Spectrom.* **2011**, *26*, 899-909.
- [5] Alfeld, M.; Pedroso, J. V.; Hommes, M. V.; Van der Snickt, G.; Tauber, G.; Blaas, J.; Haschke, M.; Erler, K.; Dik, J.; Janssens, K. *J. Anal. At. Spectrom.* **2013**, *28*, 760-767.
- [6] Dooley, K. A.; Conover, D. M.; Glinsman, L. D.; Delaney, J. K. *Angew. Chem.-Int. Edit.* **2014**, *53*, 13775-13779.
- [7] Ravaud, E.; Pichon, L.; Laval, E.; Gonzalez, V.; Eveno, M.; Calligaro, T. *Appl. Phys. A: Mater. Sci. Process.* **2016**, *122*, 7.
- [8] Alfeld, M.; Mulliez, M.; Martinez, P.; Cain, K.; Jockey, P.; Walter, P. *Anal. Chem.* **2017**, *89*, 1493-1500.
- [9] Romano, F. P.; Caliri, C.; Nicotra, P.; Di Martino, S.; Pappalardo, L.; Rizzo, F.; Santos, H. C. *J. Anal. At. Spectrom.* **2017**, *32*, 773-781.
- [10] Alberti, R.; Frizzi, T.; Bombelli, L.; Gironde, M.; Aresi, N.; Rosi, F.; Miliani, C.; Tranquilli, G.; Talarico, F.; Cartechini, L. *X-Ray Spectrom.* **2017**, *46*, 297-302.
- [11] Alfeld, M.; Broekaert, J. A. C. *Spectrochim. Acta, Part B* **2013**, *88*, 211-230.
- [12] Alfeld, M.; de Viguerie, L. *Spectrochim. Acta, Part B* **2017**, *136*, 81-105.
- [13] Delaney, J. K.; Zeibel, J. G.; Thoury, M.; Littleton, R.; Palmer, M.; Morales, K. M.; de la Rie, E. R.; Hoenigswald, A. *Appl. Spectrosc.* **2010**, *64*, 584-594.

- [14] Ricciardi, P.; Delaney, J. K.; Facini, M.; Zeibel, J. G.; Picollo, M.; Lomax, S.; Loew, M. *Angew. Chem.-Int. Edit.* **2012**, *51*, 5607-5610.
- [15] Cucci, C.; Delaney, J. K.; Picollo, M. *Acc. Chem. Res.* **2016**, *49*, 2070-2079.
- [16] Legrand, S.; Alfeld, M.; Vanmeert, F.; De Nolf, W.; Janssens, K. *Analyst* **2014**, *139*, 2489-2498.
- [17] Bertrand, L.; Robinet, L.; Thoury, M.; Janssens, K.; Cohen, S. X.; Schoder, S. *Appl. Phys. A: Mater. Sci. Process.* **2012**, *106*, 377-396.
- [18] Janssens, K.; Alfeld, M.; Van der Snickt, G.; De Nolf, W.; Vanmeert, F.; Radepont, M.; Monico, L.; Dik, J.; Cotte, M.; Falkenberg, G.; Miliani, C.; Brunetti, B. G. In *Annual Review of Analytical Chemistry, Vol 6*, Cooks, R. G.; Pemberton, J. E., Eds.; Annual Reviews: Palo Alto, 2013, pp 399-425.
- [19] Kumakhov, M. A.; Komarov, F. F. *Physics Reports-Review Section of Physics Letters* **1990**, *191*, 289-350.
- [20] MacDonald, C. A.; Owens, S. M.; Gibson, W. M. *J. Appl. Crystallogr.* **1999**, *32*, 160-167.
- [21] Bjeoumikhov, A.; Bjeoumikhova, S.; Wedell, R. *Part. Part. Syst. Charact.* **2005**, *22*, 384-390.
- [22] Hertlein, F.; Oehr, A.; Hoffmann, C.; Michaelsen, C.; Wiesmann, J. *Part. Part. Syst. Charact.* **2006**, *22*, 378-383.
- [23] De Nolf, W. *Imaging of crystalline phase distributions by means of scanning and tomographic X-ray powder diffraction*. Ph. D., University of Antwerp, Antwerp, 2013.
- [24] James, M. R. In *Catalogue of manuscripts and early printed books from the libraries of William Morris, Richard Bennett, Bertram fourth earl of Ashburnham, and other sources, now forming portion of the library of J. Pierpont Morgan*; Chiswick press: London, 1906.
- [25] Van der Snickt, G.; De Nolf, W.; Vekemans, B.; Janssens, K. *Appl. Phys. A* **2008**, *92*, 59-68.

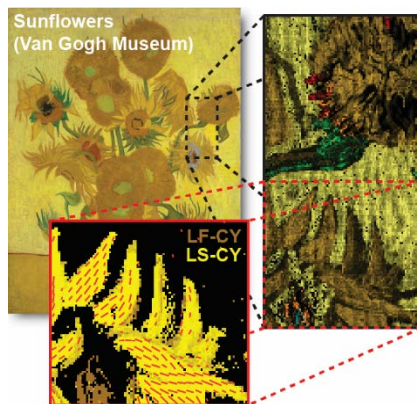
- [26] Lachmann, T.; van der Snickt, G.; Haschke, M.; Mantouvalou, I. *J. Anal. At. Spectrom.* **2016**, *31*, 1989-1997.
- [27] De Nolf, W.; Janssens, K. *Surf. Interface Anal.* **2010**, *42*, 411-418.
- [28] De Nolf, W.; Vanmeert, F.; Janssens, K. *J. Appl. Crystallogr.* **2014**, *47*, 1107-1117.
- [29] Downs, R. T.; Hall-Wallace, M. *Am. Mineral.* **2003**, *88*, 247-250.
- [30] Sole, V. A.; Papillon, E.; Cotte, M.; Walter, P.; Susini, J. *Spectrochim. Acta, Part B* **2007**, *62*, 63-68.
- [31] Burgio, L.; Clark, R. J. H.; Gibbs, P. J. *J. Raman Spectrosc.* **1999**, *30*, 181-183.
- [32] Kühn, H. In *Artists' Pigments - A Handbook of Their History and Characteristics*, Roy, A., Ed.; Archetype Publications: London, 1993, pp 83-112.
- [33] Agresti, G.; Baraldi, P.; Pelosi, C.; Santamaria, U. *Color Res. Appl.* **2016**, n/a-n/a.
- [34] Gonzalez, V.; Calligaro, T.; Wallez, G.; Eveno, M.; Toussaint, K.; Menu, M. *Microchem. J.* **2016**, *125*, 43-49.
- [35] Gettens, R. J.; Fitzhugh, E. W. In *Artists' Pigments - Handbook of Their History and Characteristics*, Roy, A., Ed.; Archetype Publications: London, 1993, pp 23-36.
- [36] Aru, M.; Burgio, L.; Rumsey, M. S. *J. Raman Spectrosc.* **2014**, *45*, 1013-1018.
- [37] Burgio, L.; Clark, R. J. H.; Hark, R. R. *Proc. Natl. Acad. Sci. U S A* **2010**, *107*, 5726-5731.
- [38] Salvado, N.; Buti, S.; Aranda, M. A. G.; Pradell, T. *Anal. Methods* **2014**, *6*, 3610-3621.
- [39] Edwards, H. G. M.; Farwell, D. W.; Perez, F. R.; Villar, S. J. *Appl. Spectrosc.* **1999**, *53*, 1436-1439.
- [40] Smieska, L. M.; Mullett, R.; Ferri, L.; Woll, A. R. *Appl. Phys. A* **2017**, *123*, 484.
- [41] Feller, R. L. In *Artists' Pigments - A Handbook of Their History and Characteristics*, Feller, R. L., Ed.; Archetype Publications: London, 1985, pp 47-64.

---

# Chapter 3 – Visualizing Chrome Yellow Subtypes

---

The discoloration rate of chrome yellow (CY), a class of synthetic inorganic pigments ( $\text{PbCr}_{1-x}\text{S}_x\text{O}_4$ ) frequently used by Van Gogh and his contemporaries, strongly depends on its sulfate content and on its crystalline structure (either monoclinic or orthorhombic). MA-XRPD imaging of selected areas on Van Gogh's 'Sunflowers' (Van Gogh Museum,



Amsterdam) revealed the presence of two CY subtypes: the light-fast monoclinic  $\text{PbCrO}_4$  (LF-CY) and the light-sensitive monoclinic  $\text{PbCr}_{1-x}\text{S}_x\text{O}_4$  ( $x \approx 0.5$ ; LS-CY). The latter was encountered in large parts of the painting indicating their higher risk for past or future darkening. Additionally, preferred orientation of LS-CY allows to observe a significant ordering of the elongated crystallites along the direction of Van Gogh's brush strokes.

This chapter is a modified version of a published paper: Reprinted with permission from **Vanmeert, F.**; Hendriks, E.; Van der Snickt, G.; Monico, L.; Dik, J.; Janssens, K. "Chemical Mapping by Macroscopic X-ray Powder Diffraction (MA-XRPD) of Van Gogh's Sunflowers: Identification of Areas with Higher Degradation Risk" In: *Angew. Chem.-Int. Edit.* **2018**, 57 (25), 7418-7422. DOI: 10.1002/anie.201713293. Copyright 2018 John Wiley and Sons.

### 3.1. INTRODUCTION

Chrome yellows (CYs), a class of inorganic pigments frequently employed by Vincent van Gogh and his contemporaries, are known to undergo darkening upon exposure to light of wavelengths shorter than 530 nm [1]. Both their original color and their tendency to darken depend on the chemical composition and crystalline structure: orange-yellow CY has a  $\text{PbCrO}_4$  composition (encountered in nature as the mineral crocoite) while partial substitution of  $\text{CrO}_4^{2-}$  by  $\text{SO}_4^{2-}$  ions yields lighter-toned CY ( $\text{PbCr}_{1-x}\text{S}_x\text{O}_4$ , with  $0 < x < 0.8$ ) [2,3]. For  $0 \leq x < 0.5$ , CY has a monoclinic crystal structure; for  $x \geq 0.5$  the solid has an orthorhombic unit cell. Since  $\text{SO}_4^{2-}$  ions are smaller than  $\text{CrO}_4^{2-}$  ions, with increasing  $x$ , the lattice parameters of both monoclinic and orthorhombic  $\text{PbCr}_{1-x}\text{S}_x\text{O}_4$  gradually decrease; a phenomenon typical of solid solution materials [4-6]. This lattice contraction is readily measurable by means of X-ray powder diffraction (XRPD). Transformation from the monoclinic to the orthorhombic structure also causes its solubility to increase [5]. Dissolved chromate ions may oxidize molecules in their environment and hereby become reduced themselves, forming a superficial, dark (olive to brown) coating of (non-crystalline)  $\text{Cr}^{\text{III}}$  compounds on the bright yellow paint [7,8]. Orthorhombic forms of  $\text{PbCr}_{1-x}\text{S}_x\text{O}_4$  are extremely light sensitive; the tendency of monoclinic  $\text{PbCr}_{1-x}\text{S}_x\text{O}_4$  to darken under the influence of light is considerably less but it increases with  $x$  [3]. Next to these different chrome yellow types, another Pb and Cr-containing pigment called chrome orange ( $\text{PbCrO}_4 \cdot \text{PbO}$ , found in nature as phoenicochroite) is used by Van Gogh.

On *Sunflowers* (1889, Van Gogh Museum, NL), a series of ca. 20 noninvasive point measurements by means of in situ vibrational spectroscopy, in combination with Raman and Fourier Transform Infrared microspectroscopy and synchrotron (SR) microdiffraction investigations on two minute paint samples available from this painting, showed that different subtypes of CY were used by Van Gogh when

creating this painting: the 'regular' light-fast (LF)  $\text{PbCrO}_4$  and the light-sensitive (LS) S-rich CY varieties [9]. In the two paint micro samples, also evidence for superficial formation of  $\text{Cr}^{\text{III}}$  was encountered associated with  $\text{PbCr}_{1-x}\text{S}_x\text{O}_4$  ( $x \approx 0.4 - 0.5$ ).

In order to gain a deeper insight into possible color changes in the yellow areas of *Sunflowers* and to pinpoint those areas most prone to show discolorations, either in the past or in the future, it was considered highly relevant (a) to determine which and how many CY subtypes (in terms of their sulfate-content and crystal structure) were present and (b) to visualize their distribution and gather other relevant information on their use by Van Gogh in this iconic painting.



## 3.2. EXPERIMENTAL SECTION AND METHODS

### 3.2.1. MA-XRF

MA-XRF maps were collected using an in house-built instrument consisting of a measuring head that is moved over the painting surface by means of an XY-motorized stage [10]. This motorized stage features a minimum step size of 10  $\mu\text{m}$  and a maximum travel range of 600  $\times$  600  $\text{mm}^2$  (hor.  $\times$  vert., Newport Corporation, Irvine, CA, US). The measuring head consists of a Rh-target X-ray tube (MOXTEK “Magnum”, 10 W, MOXTEK Inc., UT, US) and four 50  $\text{mm}^2$  Vortex silicon drift detectors (SII, Northridge, CA, US), as shown in Figure 3-1A. The beam size, defined by means of a collimator, was around 0.5 mm. During the scans, 0.5 mm steps were taken in X and Y directions while the collection time per pixel was 200 ms.

### 3.2.2. MA-XRPD

The MA-XRPD instrument employs a low power Ag-anode X-ray micro source (44 W, I $\mu$ S-Ag<sup>HB</sup>, Incoatec GmbH, DE) that delivers a monochromatic (Ag-K $\alpha$ ; 22.16 keV) and focused X-ray beam (focal spot diameter: 112 (3)  $\mu\text{m}$ ; output focal distance: 21.6 (1) cm; divergence: 3.8 (3) mrad). A PILATUS 200K detector (Dectris Ltd., CH) collects diffraction patterns in transmission mode: the detector is placed perpendicular to the source at the output focal distance. The painting *Sunflowers* was put in a custom-made easel and positioned in front of the area detector at a distance of ~11 cm (see Figure 3-1B). XYZ motorized stages (max. travel ranges: 10 cm  $\times$  25 cm  $\times$  10 cm, Newport Corporation, Irvine, CA, US) were used to carefully move the artwork during the imaging experiment (ca. 1  $\text{mm s}^{-1}$ ). Calibration of several instrumental parameters was performed with a LaB<sub>6</sub> standard for powder diffraction (SRM 660, NIST). The analytical characteristics of the MA-XRPD system are described in Chapter 2 (configuration I2).

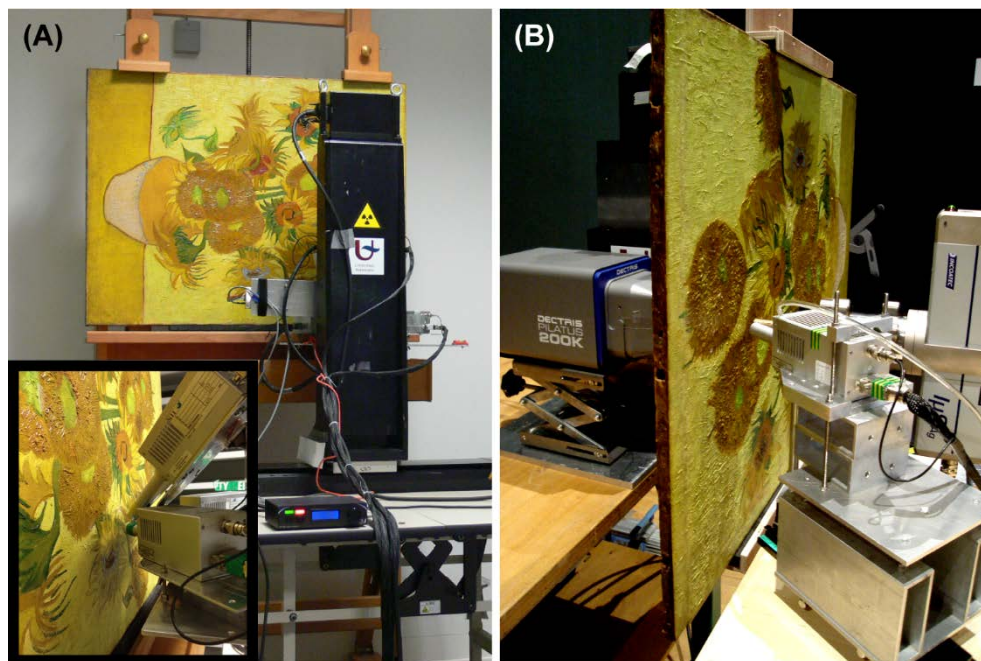


Figure 3-1. Photographs of the (A) MA-XRF and (B) MA-XRPD imaging investigations on *Sunflowers* (1889, F458, Van Gogh, Van Gogh Museum, NL). The inset of (A) shows the measuring head of the MA-XRF instrument.

The various MA-XRPD mapping experiments on *Sunflowers* were made with a dwell time of 10 seconds per pixel. The step size used and total size of the analyzed areas are shown in Table 3-1.

**Table 3-1. MA-XRPD scan parameters of the analyzed areas**

Area	Step Size (mm <sup>2</sup> )	Map Size (cm <sup>2</sup> )	# points	Dwell Time (s point <sup>-1</sup> )	Total Time (h)
A	1 × 1	9.2 × 18.2	17019	10	58.7
B	2.5 × 2.5	24.5 × 9.25	3762	10	16.0
C	2.5 × 2.5	24.5 × 9.25	3762	10	16.0
D	1 × 1	8.5 × 6.7	5848	10	20.2

### 3.2.3. MA-XRPD data processing

The same whole pattern fitting procedure as the one outlined in section 2.2.7 was used to obtain compound-specific distribution maps for the different analyzed areas on *Sunflowers*. For phoenicochroite a region-of-interest (ROI) over the ( $\bar{3}11$ ) reflection was used to visualize its distribution. This was necessary because of strong overlap of phoenicochroite with crocoite, minium and vermilion. In order to differentiate between various CY types, the shift in the diffraction peaks of  $\text{PbCr}_{1-x}\text{S}_x\text{O}_4$  which is induced by the gradual decrease of the lattice parameters with increasing sulfate substitution is used. The procedure used to link the observed shift in the diffraction signals to the different degrees of sulfate substitution is described in section 3.2.4.

### 3.2.4. Peak shift and displacement

#### 3.2.4.1. Single CY compound

Diffraction patterns for different monoclinic solid solutions were calculated based on the crystal structure of crocoite [11] and the reported unit cell dimensions of several  $\text{PbCr}_{1-x}\text{S}_x\text{O}_4$  with different  $\text{SO}_4^{2-}$  substitution degrees ( $x = 0, 0.11, 0.24, 0.40$  and  $0.46$ ) [5], as shown in Figure 3-2A. Since no atomic positions for the solid solution series are known,  $\text{S}^{\text{VI}}$  was assumed to occupy the same position as  $\text{Cr}^{\text{VI}}$ . The calculated diffraction patterns of the solid solutions are in good agreement with the  $\text{PbCrO}_4$  reference, which is offset by a single displacement parameter (Figure 3-2B). This parameter is necessary to shift the positions of the diffraction peaks to match those of the solid solutions; the shift in peak position is the result of the lattice contraction that occurs when the smaller  $\text{SO}_4^{2-}$  replace the  $\text{CrO}_4^{2-}$  ions. The displacement parameter shows a linear correlation with the  $\text{SO}_4^{2-}$  content within the  $\text{PbCr}_{1-x}\text{S}_x\text{O}_4$  structure (Figure 3-2C). The different relative intensity of the calculated diffraction signals was not modeled as no  $\text{S}^{\text{VI}}$  is added

to the monoclinic  $\text{PbCrO}_4$  reference structure during the refinement procedure; only the displacement, scaling and width parameter of  $\text{PbCrO}_4$  are refined. Since the correlation between the diffraction peak shift and the displacement parameter is also influenced by the distance between the diffraction camera and the painting, slightly different displacement values are found for the different  $\text{PbCr}_{1-x}\text{S}_x\text{O}_4$  solid solutions in the different analyzed areas, see Table 3-2.

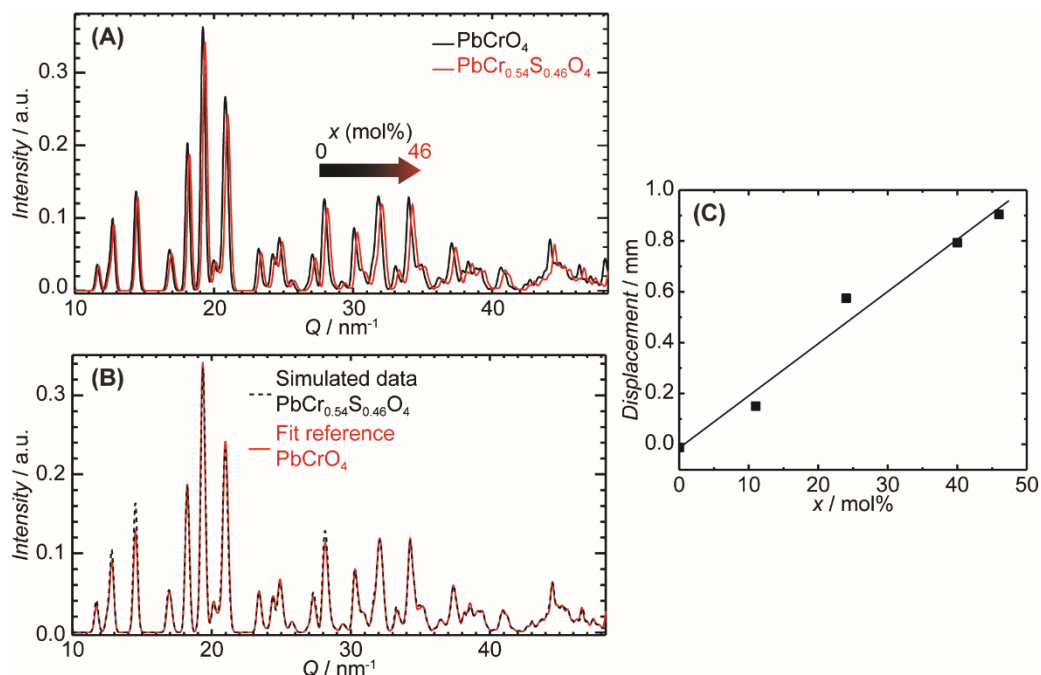


Figure 3-2. A) Calculated diffraction intensity in function of the momentum transfer ( $Q$ ) for the monoclinic CY subtypes:  $\text{PbCrO}_4$  and  $\text{PbCr}_{0.54}\text{S}_{0.46}\text{O}_4$ . B) Fit of the calculated diffraction intensity for  $\text{PbCr}_{0.54}\text{S}_{0.46}\text{O}_4$  with the  $\text{PbCrO}_4$  reference. C) Correlation between the calculated displacement parameter of monoclinic  $\text{PbCrO}_4$  and the degree of sulfate substitution ( $x$ ) using experimental parameters of area C.

When  $x$  exceeds 0.4 - 0.5 a transformation from the monoclinic to the orthorhombic structure, similar to  $\text{PbSO}_4$ , is observed. During synthesis of the

co-precipitates orthorhombic  $\text{PbCr}_{1-x}\text{S}_x\text{O}_4$  with  $x \approx 0.9$  is typically formed when increasing amounts of sulfate are added [4,5]. In analogy to the monoclinic co-precipitates, a shift of the diffraction peak position for  $\text{PbCr}_{0.1}\text{S}_{0.9}\text{O}_4$  compared to anglesite ( $\text{PbSO}_4$ ) is observed because of the smaller unit cell dimensions of the latter. However, since the orthorhombic  $\text{PbCr}_{1-x}\text{S}_x\text{O}_4$  type was not encountered on *Sunflowers*, only co-precipitates with  $x < 0.5$  are discussed in the following sections.

**Table 3-2. Calculated displacement values for two  $\text{PbCr}_{1-x}\text{S}_x\text{O}_4$  solid solutions ( $x = 0$  and  $x = 0.46$ ) for the different areas analyzed with MA-XRPD.**

Area	$\text{PbCr}_{1-x}\text{S}_x\text{O}_4$	
	$x = 0.00$	$x = 0.46$
	Displacement (mm)	
A	-0.01	0.98
B	-0.01	0.88
C	-0.01	0.91
D	-0.01	0.88

#### 3.2.4.2. Mixtures of two CYs

When overlapping layers (or a mixture) of two different CY types are present, both compounds are expected to appear in the diffraction data. However, because of the small shift in peak position the angular resolution of the MA-XRPD instrument is not able to separate the diffraction peaks originating from both CYs. On the other hand, when using the same  $\text{PbCrO}_4$  reference to fit the simulated diffraction data for the CY mixture, the refined shift depends linearly on the relative weight fractions of the two CYs (Figure 3-3). The obtained displacement value for the CY mixture will lie between the displacement values obtained for the single CYs and depends on the weight ratios of the CY subtypes. This

abundance-displacement relationship will be used later in this chapter, e.g. in Figure 3-10 to create the color scale of the false color image (shown below the histograms). Figure 3-3C shows that the width of the combined CY diffraction peaks is somewhat broader than for the individual components. This broadening effect is however very limited and is smaller than the typical point-by-point variation, especially when only a low amount of CY is present.

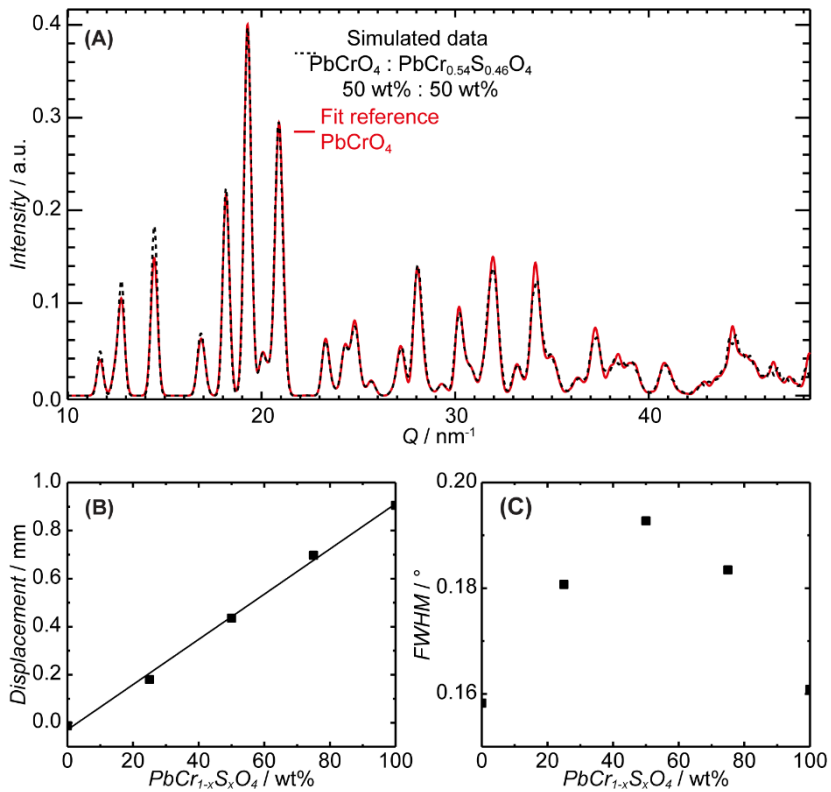


Figure 3-3. A) Calculated diffraction intensity in function of the momentum transfer ( $Q$ ) for a 50:50 wt% mixture of  $\text{PbCrO}_4$  and  $\text{PbCr}_{0.54}\text{S}_{0.46}\text{O}_4$  (dashed line) and the fit using only  $\text{PbCrO}_4$  (red line). The refined shift and width of the  $\text{PbCrO}_4$  reference are shown in B and C. B) Displacement; and C) width parameter of the  $\text{PbCrO}_4$  reference used for fitting several calculated mixtures of  $\text{PbCrO}_4$  and  $\text{PbCr}_{0.54}\text{S}_{0.46}\text{O}_4$  using experimental parameters of area C.

### 3.2.4.3. Influence of displacement and layer thickness

The shift in diffraction peak position can also be caused by a displacement of the sample or individual paint layers to the calibrated distance of the instrument [12] and will be discussed in Chapter 5. In this chapter, this effect is limited because of the (relatively) long distance between the painting and the detector (~11 cm) and the limited displacement-like shift (< 1 mm). In order to further reduce the influence of the displacement of the painting and of the CY paint layers on the measured peak shift, the displacements of beeswax, used for relining, and hydrocerussite, present in the ground layer, were used as internal markers. Both compounds are present throughout the entire analyzed areas and are not expected to show different unit cell dimensions when compared to those reported in literature.

### 3.2.5. Preferred orientation

Intensity profiles in function of the azimuthal angle  $\gamma$  were integrated between  $9.03 \leq 2\theta \leq 9.58$  and  $9.58 \leq 2\theta \leq 10.20$ , respectively for reflection (200) and (120) of  $\text{PbCr}_{1-x}\text{S}_x\text{O}_4$ . To reduce signal noise, the diffraction images were binned 4x4 before  $2\theta$ -integration. The resulting  $2\theta$  integrated intensity profiles were fitted using a constant background and two Gaussians (one for each intensity maximum). In the vector plots shown further on in this chapter (Figure 3-13) the lengths of the vectors are proportional to the averaged refined intensity of both Gaussians and are normalized to unity. The directions of the vectors stand orthogonal to the refined azimuthal positions of the two Gaussians and show the projected [001] direction of the LS-CY crystallites onto the paint surface.

### 3.3. RESULTS AND DISCUSSION

#### 3.3.1. Pigment Identification

Considering that S-poor and S-rich subtypes of CY show a different atomic Pb:Cr ratio, it is useful to evaluate the distribution of these elements and their co-localization throughout the *Sunflowers* painting as determined by macroscopic X-ray fluorescence imaging (MA-XRF). Both the composite false color map (Figure 3-4B) and the Cr- $K_{\alpha}$  vs. Pb- $L_{\alpha}$  XRF intensity scatter plot (Figure 3-4C) qualitatively suggest that two or more CY subtypes may be present: light-fast  $PbCrO_4$  (LF-CY), light-sensitive  $PbCr_{1-x}S_xO_4$  ( $x \approx 0.5$ ; LS-CY) and mixtures or superimposed areas with other pigments. However, the detected XRF intensity is not only determined by the atomic Pb:Cr ratio but is also influenced by other factors such as the local paint thickness or the presence of Pb or Cr-containing admixture pigments (e.g., red lead,  $Pb_3O_4$ ; lead white,  $PbCO_3$  and/or  $2PbCO_3 \cdot Pb(OH)_2$ ; viridian,  $Cr_2O_3 \cdot 2H_2O$ ; chromium green,  $Cr_2O_3$  and chrome orange,  $PbCrO_4 \cdot PbO$ ). Furthermore, MA-XRF does not allow for sensitive and reliable mapping of sulfur because of strong absorption of the low energy S-K X-rays and overlap with Pb-M fluorescence lines.

Thus, a different approach was taken to more directly determine the different CY subtypes present in *Sunflowers* and create highly-specific images of their distribution. This involves the use of transmission mode macroscopic X-ray powder diffraction (MA-XRPD) scanning [13]. It involves irradiating a small spot (diameter < 0.5 mm) of the paint surface while the painting is carefully moved through the X-ray beam, allowing to collect XRPD data at all locations in the scanned area. On *Sunflowers*, three regions, each of the order of  $10 \times 20$  cm<sup>2</sup> and featuring a variety of yellow tonalities, were examined in this manner (see Figure 3-4A and Table 3-1). Although care should be taken when exposing



photosensitive pigments to energetic X-rays, the dose deposited onto the painting during the MA-XRPD analyses was  $\sim 10^7$  times smaller compared to typical SR- $\mu$ -XRPD investigations [14].

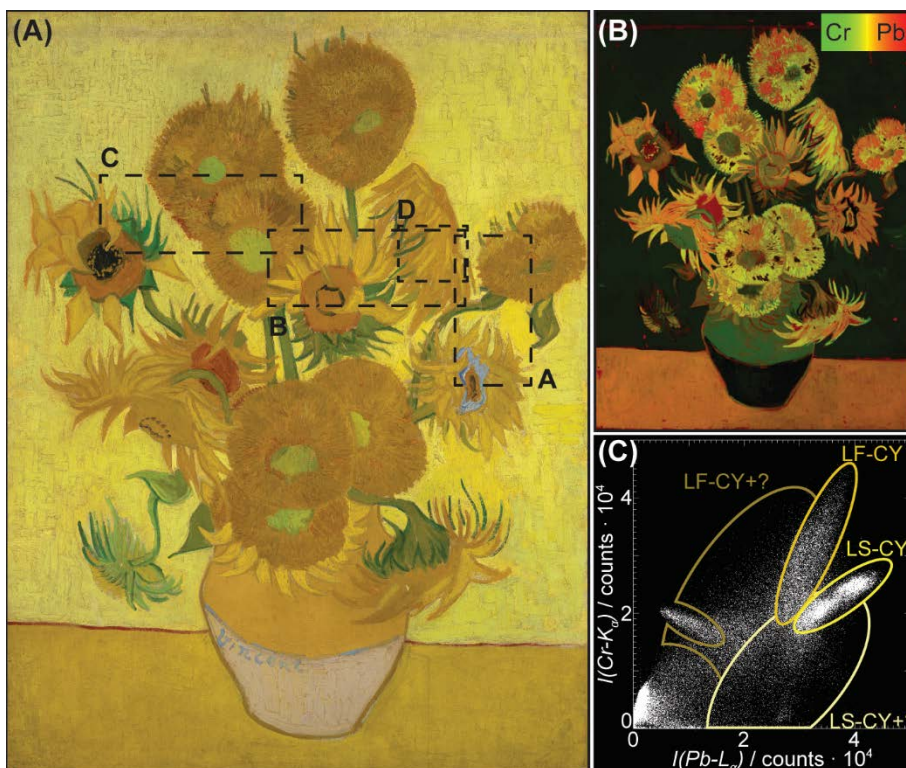


Figure 3-4. A) Photograph of *Sunflowers* by Vincent Van Gogh (1889, F458, Van Gogh Museum, Amsterdam, NL) with dashed boxes marking the different areas analyzed with MA-XRPD. B) RG composite MA-XRF map of Pb/Cr. C) Cr-K $\alpha$  vs. Pb-L $\alpha$  XRF intensity scatter plot of the entire painting with colored outlines indicating different CY subtypes. LF-CY+? and LS-CY+? indicate CY overlapped or mixed with other pigments.

In Figure 3-5 (and in Figure 3-6, **Figure 3-7** and Figure 3-8) the MA-XRPD maps of hydrocerussite (lead white,  $2\text{PbCO}_3 \cdot \text{Pb}(\text{OH})_2$ ), zincite (zinc white,  $\text{ZnO}$ ), copper aceto-arsenate (emerald green,  $\text{Cu}(\text{CH}_3\text{COO})_2 \cdot 3\text{Cu}(\text{AsO}_2)_2$ ) and of lead

chromate (chrome yellow, monoclinic  $\text{PbCr}_{1-x}\text{S}_x\text{O}_4$ ) illustrate how the pigment materials can be readily correlated to the visual aspect of the paint: while in general, zincite is only present in the pale-yellow background, lead white, present in the ground of the canvas, is much more evenly distributed. Emerald green was used for painting the light and dark green stems of the sunflowers, sometimes mixed with CY. CY is present in both the upper, darker flower as well as in the lower, lighter colored one and is present in small amounts in the background. Black parts in the lead white and beeswax maps show where the paint layer very strongly absorbed the primary radiation (e.g., the orange corolla of the upper flower, applied by Van Gogh with mm-thick paint) so that no useful XRPD signals could be recorded in transmission. In other areas, thinner paint layers are present that could readily be analyzed with XRPD. Several orange highlights in the flowers contain chrome orange ( $\text{PbCrO}_4\cdot\text{PbO}$ , Figure 3-5G), while (photo-degradation prone, see Chapter 6) minium ( $\text{Pb}_3\text{O}_4$ ) and vermilion ( $\text{HgS}$ ) have been used in orange-red and brown-red features (visible in Figure 3-5F and Figure 3-6H). Ultramarine blue (lazurite,  $\text{Na}_4\text{Ca}_4\text{Al}_6\text{Si}_6\text{O}_{24}\text{S}_2$ ) is present in the very dark color used in the hearts of two of the analyzed flowers (Figure 3-5H). This pigment is expected to have also been used in the lighter blue color; however its low scattering power limits its detection by XRPD (as shown in Chapter 4). Although mostly present in the pale-yellow background, zinc white was also used in the light blue contour and in the yellow petals of at least one flower (Figure 3-7C). Finally, barite ( $\text{BaSO}_4$ ) and goethite ( $\alpha\text{-FeOOH}$ ) are rarely encountered and are indicative of retouches (Figure 3-5I; goethite distribution not shown). All identified pigments are consistent with *in situ* Raman investigations on selected points (see Supporting Information, section 3.5) and make up the palette used by Van Gogh during his period in Arles [15].

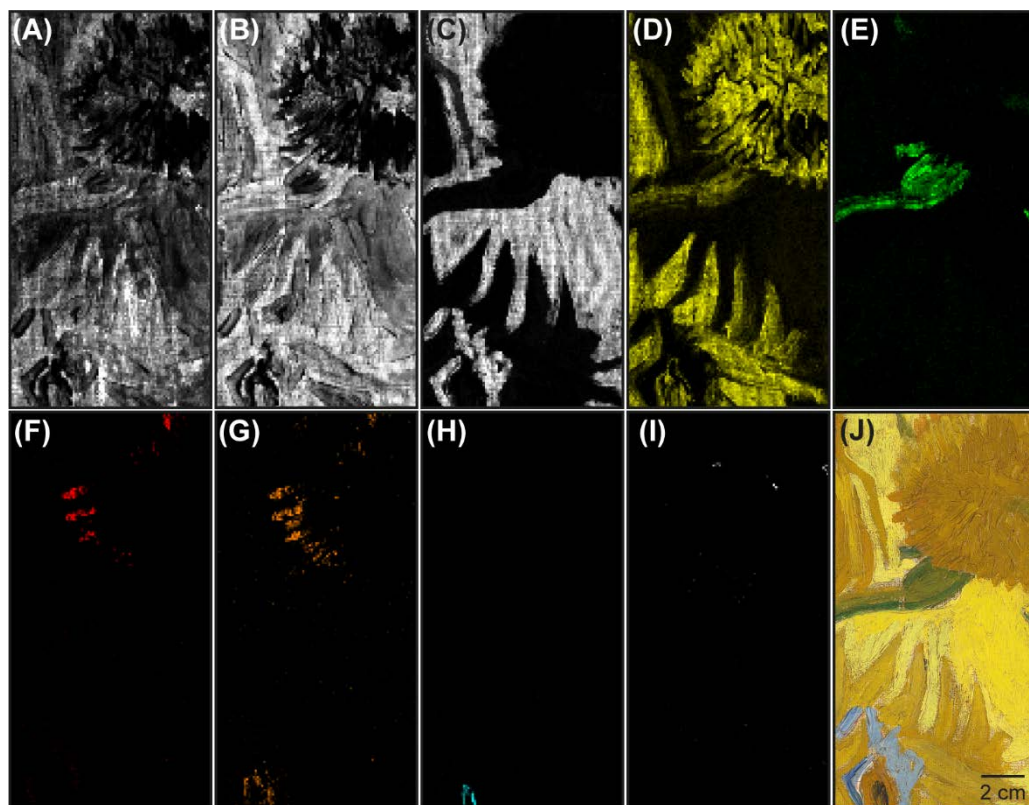


Figure 3-5. Compound-specific MA-XRPD distributions of A) beeswax; B) hydrocerussite; C) zincite; D) chrome yellow; E) emerald green; F) minium; G) ROI chrome orange ( $\bar{3}11$ ) and minium ( $211$ ); H) lazurite; I) barite. Brighter color indicates a larger peak area (G) or a higher scaling parameter (others). Map size:  $92 \times 182 \text{ mm}^2$ ; Pixel size:  $1 \times 1 \text{ mm}^2$ . J) Photograph of area A.

It is highly relevant to note that in the scanned areas no evidence of orthorhombic CY subtypes ( $\text{PbCr}_{1-x}\text{S}_x\text{O}_4$  with  $x > 0.5$ ) was found, consistent with previous investigations [9]. Thus, only contributions for monoclinic CY types were included in the XRPD pattern fitting model. In first instance, this sufficed to visualize the sum distribution of all monoclinic CY types ( $\text{PbCr}_{1-x}\text{S}_x\text{O}_4$  with  $x < 0.5$ ), as shown in Figure 3-5-8D.

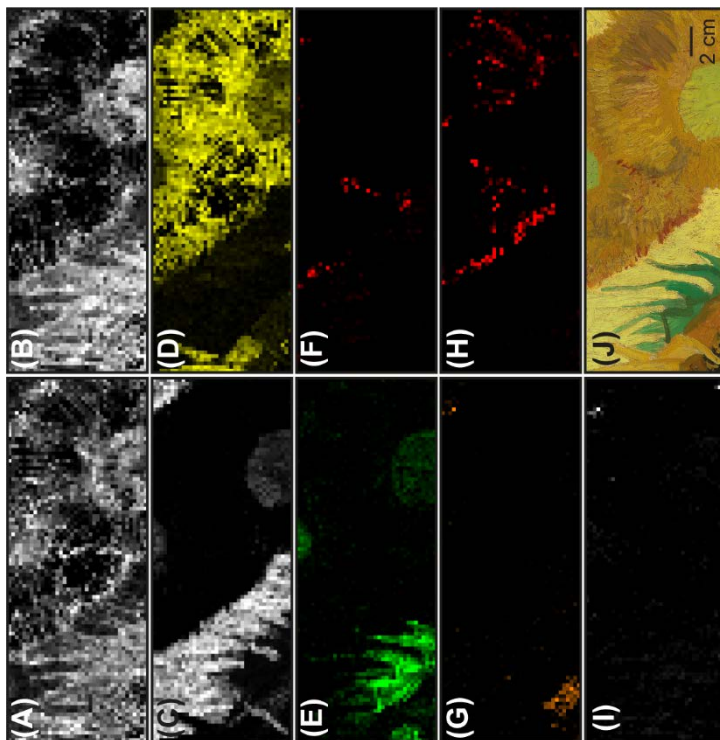


Figure 3-6. Compound-specific distribution maps of A) beeswax; B) hydrocerussite; C) zincite; D) chrome yellow; E) emerald green; F) minium; G) ROI chrome orange ( $\bar{3}u$ ); H) vermilion; and I) barite. Brighter color indicates a larger peak area (G) or a higher scaling parameter (others). Map size:  $245 \times 92.5 \text{ mm}^2$ ; Pixel size:  $2.5 \times 2.5 \text{ mm}^2$ . J) Photograph of area C.

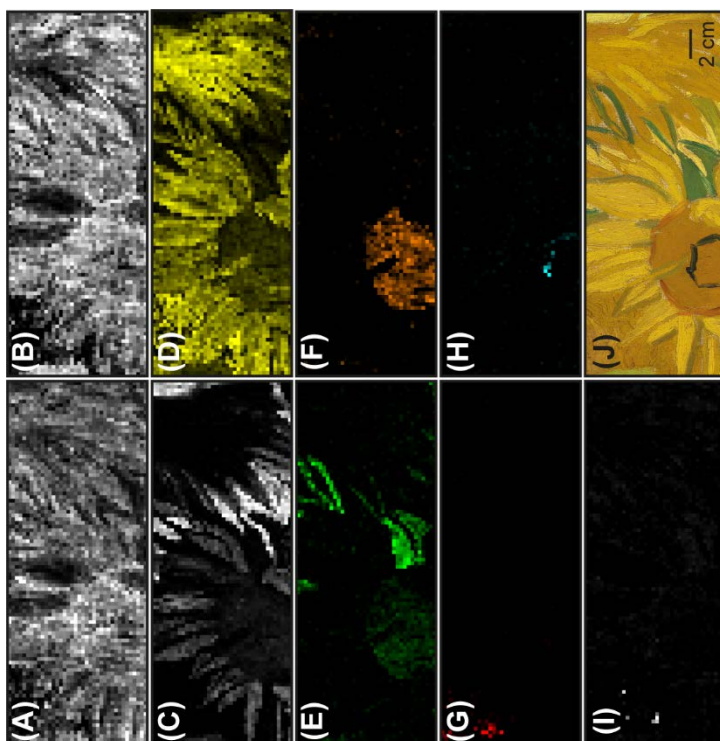


Figure 3-7. Compound-specific distribution maps of A) beeswax; B) hydrocerussite; C) zincite; D) chrome yellow; E) emerald green; F) ROI chrome orange ( $\bar{3}u$ ); G) lazurite; H) vermilion; and I) barite. Brighter color indicates a larger peak area (F) or a higher scaling parameter (others). Map size:  $245 \times 92.5 \text{ mm}^2$ ; Pixel size:  $2.5 \times 2.5 \text{ mm}^2$ . J) Photograph of area B.

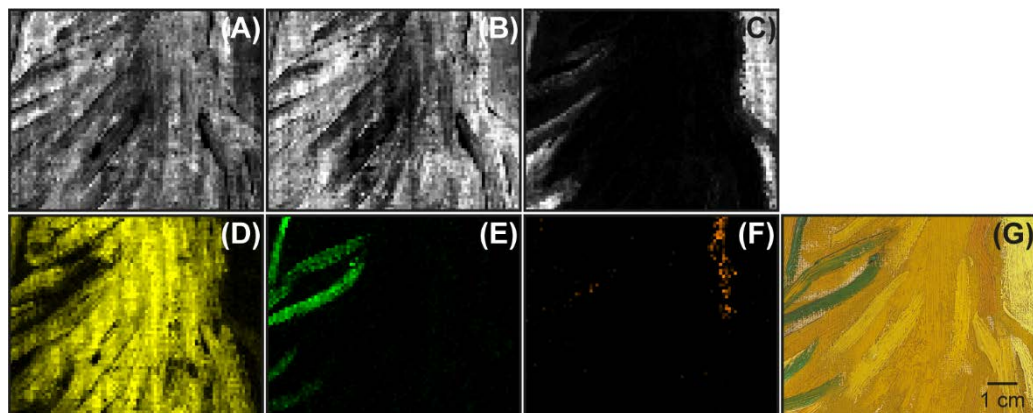


Figure 3-8. Compound-specific distribution maps of A) beeswax; B) hydrocerussite; C) zincite; D) chrome yellow; E) emerald green; and F) ROI chrome orange ( $\bar{3}\mu$ ). Brighter color indicates a larger peak area (F) or a higher scaling parameter (others). Map size:  $85 \times 67 \text{ mm}^2$ ; Pixel size:  $1 \times 1 \text{ mm}^2$ . G) Photograph of area D.

### 3.3.2. Chrome yellow subtypes

To differentiate between the various monoclinic  $\text{PbCr}_{1-x}\text{S}_x\text{O}_4$  subtypes (each characterized by a distinct  $x$  value), a careful comparison was made between the experimental  $2\theta$  (or  $Q$ ) positions of their diffraction lines and the reported peak positions of  $\text{PbCrO}_4$  [11]. The gradual shrinking of the cell dimensions of monoclinic CY, resulting from the increasing substitution of chromate by sulfate ions, is reflected in a shift of the diffraction lines of  $\text{PbCr}_{1-x}\text{S}_x\text{O}_4$  towards higher  $2\theta$  (or  $Q$ ) values (Figure 3-9) [5].

Such a shift, however, can also be caused by a slightly longer distance between the irradiated paint and the XRPD camera. Both shifts are contained within the displacement parameter obtained during data refinement. A correction for displacements caused by the (rough) paint surface and for variations in the thickness of the underlying layers was applied using the displacement parameters

obtained for beeswax, more or less homogeneously applied during lining of the painting in 1927, and lead white, present in the ground (see section 3.2.4.3). In this manner the corrected displacement parameter for CY at all analyzed locations (several thousand per scanned area, see Table 3-1) can be considered to reflect the unit cell contraction and thus the CY subtype at each location.

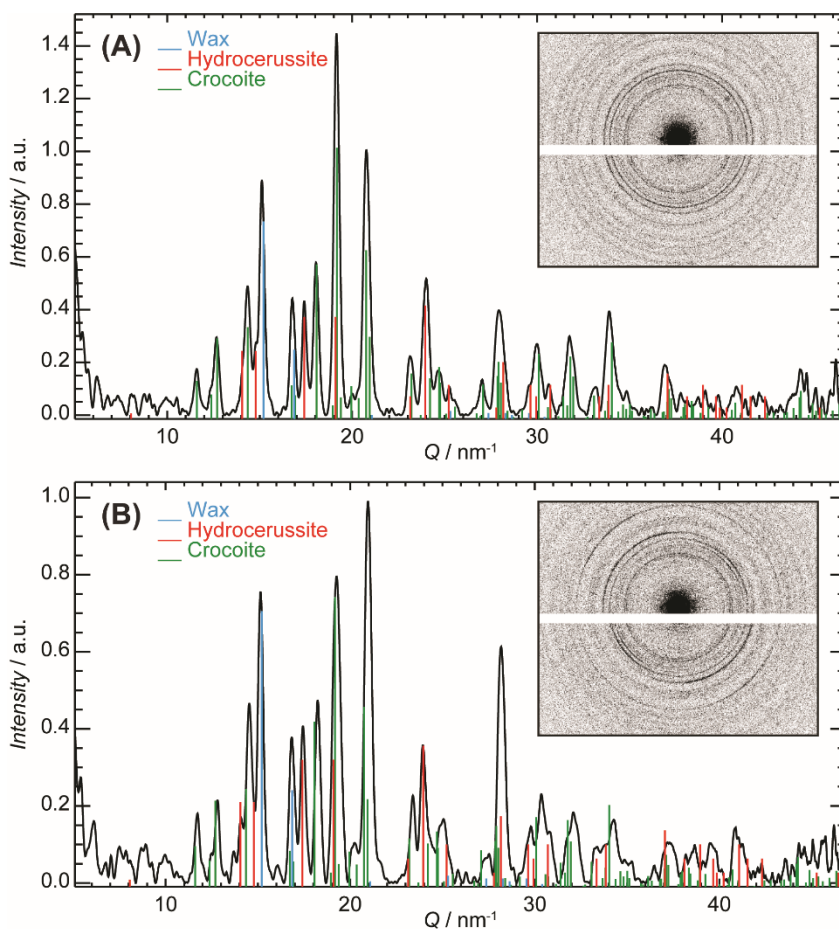


Figure 3-9. X-ray diffractograms and diffraction images of single data points located in a region containing A) the monoclinic  $\text{PbCrO}_4$  and B) the monoclinic  $\text{PbCr}_{1-x}\text{S}_x\text{O}_4$  ( $x \approx 0.5$ ). A clear shift of the diffraction signals for the latter is visible compared to the  $\text{PbCrO}_4$  (crocoite) reference.

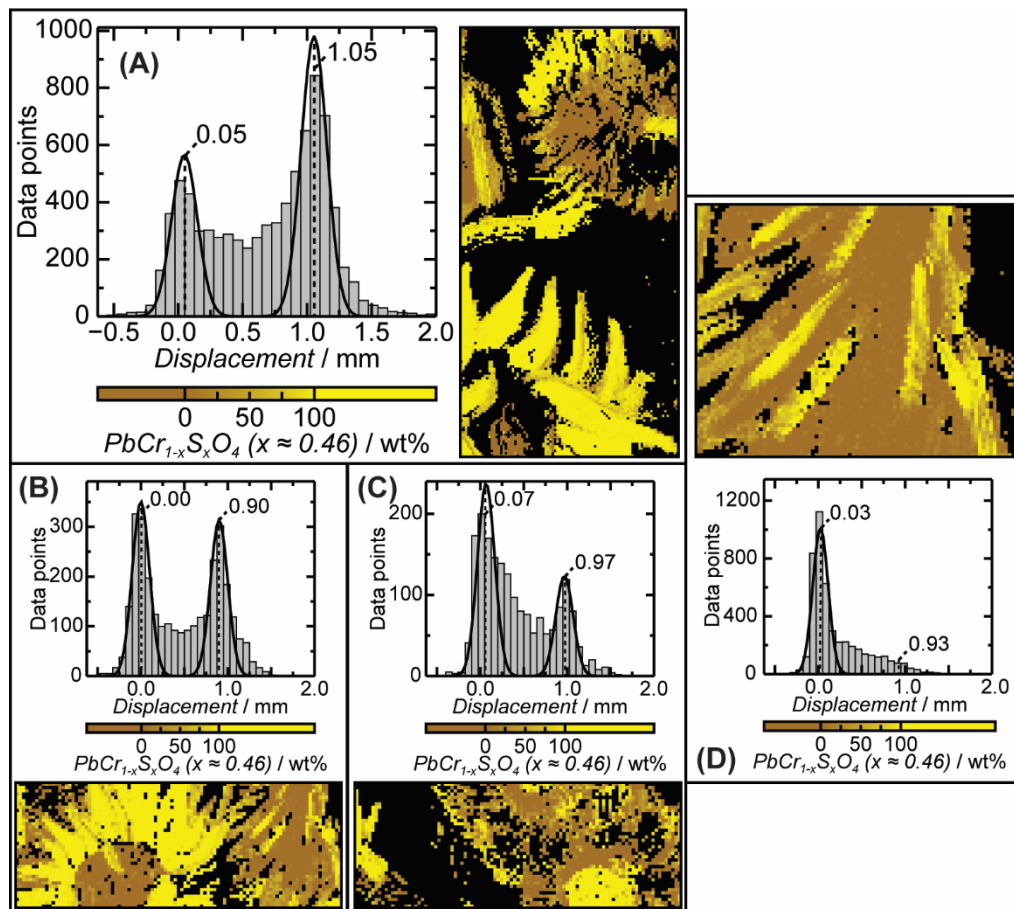


Figure 3-10. A) Histogram showing the corrected displacement for the  $\text{PbCrO}_4$  reference caused by substitution of  $\text{CrO}_4^{2-}$  by  $\text{SO}_4^{2-}$ . A threshold based on the  $\text{PbCrO}_4$  scaling parameter was used to remove data points with no or uncertain displacement information. The false color image shows the distinction between  $\text{PbCrO}_4$  (ochre-yellow) and  $\text{PbCr}_{1-x}\text{S}_x\text{O}_4$  (yellow) employing the color scale shown below the histogram for area A. Same for B) area B; C) area C; and D) area D.

In Figure 3-10, the set of corrected displacement parameter values of  $\text{PbCrO}_4$  for areas A, B, C and D are shown in the form of 2D color-coded distributions and frequency histograms. The bimodal nature of the histograms clearly points to the presence of two distinct CY types in *Sunflowers*: monoclinic  $\text{PbCrO}_4$  ( $x = 0$ ,

crocoite, LF-CY) and  $\text{PbCr}_{1-x}\text{S}_x\text{O}_4$  ( $x \approx 0.5$ , LS-CY). This is in agreement with previous results obtained from only selected points on this painting [9]. Indeed the calculated diffraction peak displacement values for the monoclinic  $\text{PbCr}_{1-x}\text{S}_x\text{O}_4$  end members ( $x = 0$  and  $x \approx 0.5$ ) match very well with the experimental histogram distributions; the calculated values for  $x = 0$  and  $x \approx 0.5$  are respectively -0.01 and 0.98 mm, -0.01 and 0.88 mm, -0.01 and 0.91 mm, and -0.01 and 0.88 mm for areas A, B, C and D, see Table 3-2. The small deviations between measured and calculated displacement values can be attributed to the (imperfectly corrected) thickness variations of the CY paint layer (and/or of underlying paint layers).

In case a mixture or overlapping brush strokes of the two CY subtypes was analyzed, intermediate displacement values are obtained (as visible in the histograms of Figure 3-10). Indeed, the displacement value shows a linear trend as a function of the relative CY weight fractions (as shown in section 0). In area D (Figure 3-10D) a single clear distribution for  $\text{PbCrO}_4$  is encountered because of its dominant presence; the higher displacement values corresponds to locations where bright-yellow  $\text{PbCr}_{1-x}\text{S}_x\text{O}_4$  ( $x \approx 0.5$ ) brush strokes were applied on top of 'regular'  $\text{PbCrO}_4$ .

From the above considerations, we can conclude that in *Sunflowers*, next to LF-CY ( $\text{PbCrO}_4$ ) also extensive areas were painted by Van Gogh with a single LS-CY subtype ( $\text{PbCr}_{1-x}\text{S}_x\text{O}_4$ ;  $x \approx 0.5$ ). Indeed, in the combined examined areas (excluding the pale-yellow background), 33% of the painting surface is covered with the LS-CY, comparable to LF-CY (31%), see Table 3-3. As LS-CY is also the CY subtype present in the pale-yellow background, and the light-yellow table area (not analyzed with MA-XRPD) [9], it becomes clear that this is the dominant CY subtype used by Van Gogh in this version of *Sunflowers*.



**Table 3-3. Area fractions of LF-CY and/or LS-CY**

Area	LF-CY <sup>a</sup> (%)	LS-CY <sup>a</sup> (%)	no CY <sup>b</sup> (%)
A	18	32	51
B	40	43	18
C	31	25	45
D	60	21	19
Overall <sup>c</sup>	31	33	36

<sup>a</sup> excluding the pale-yellow background

<sup>b</sup> including the pale-yellow background

<sup>c</sup> excluding area D (area D is included in area B)

In Table 3-3 the area that contains either LF-CY or LS-CY was estimated from the relative abundance of the two subtypes (see section 0). The surface area of data points that contain only one CY subtype are included in the respective CY area fraction, while for pixels that contain a LF-LS mixture, the relative abundance of the two CYs was used to divide the pixel area between the two subtypes.

The false color images of Figure 3-10 permit to identify the regions on *Sunflowers* that contain LS-CY, so that they can be more closely monitored in the future. Monoclinic  $\text{PbCrO}_4$  is mostly present in orange-yellow/ochre areas, such as the corollas, while LS-CY is present in the bright yellow tones, e.g. the yellow petals and the yellow regions in the corollas. However, in the case of mixtures or overlaying paint strokes such a visual distinction cannot be so easily made. For example, in the orange flower hearts, LF-CY is present together with emerald green and chrome orange (Figure 3-7) and in several areas in the corollas it is found together with vermilion or minium, possibly together with some LS-CY (Figure 3-6). The latter is also found together with emerald green in the stem of the sunflowers and in the intricate pigment mixtures used for the green flower hearts (that also contain emerald green and zinc white, Figure 3-6). Mixtures or overlapping layers of both CY types are found in the orange-yellow/ochre

contours of the yellow petals and throughout the orange corollas. In area D overlapping layers of LS-CY on top of yellow-orange LF-CY are present, while in a single stroke of orange paint the presence of overlapping layers of both CY types together with chrome orange is revealed (Figure 3-8). Finally in the red tones of one of the flowers (Figure 3-6) and in several orange strokes (Figure 3-5), probably a mixture of both CY's together with minium, vermillion or chrome orange was used (see Supporting Information, section 3.5 for additional Raman results).

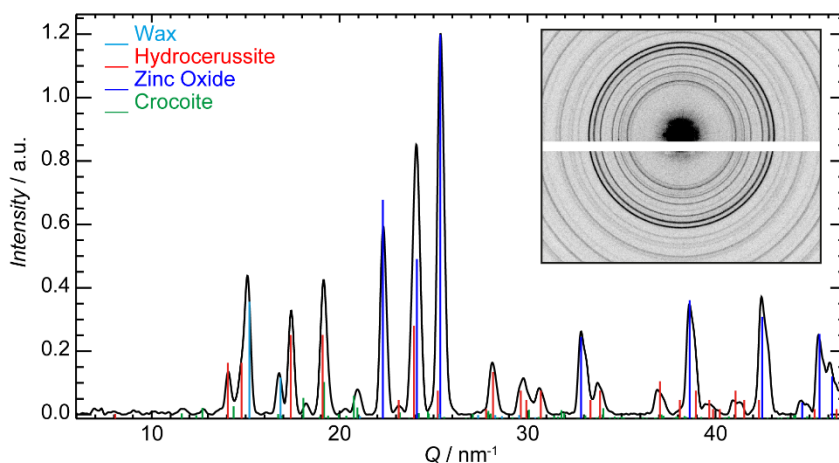


Figure 3-11. Averaged X-ray diffractogram and diffraction image obtained in the pale-yellow background.

Although LS-CY is found in small amounts together with zinc white in the pale-yellow background, it is not visible in the false color images of Figure 3-10. The low diffraction intensity observed hampers (automated) identification of LS-CY (Figure 3-11). This issue is further complicated by the strong degree of preferred orientation visible in the 2D XRPD patterns of LS-CY.

### 3.3.3. Preferred orientation of LS-CY

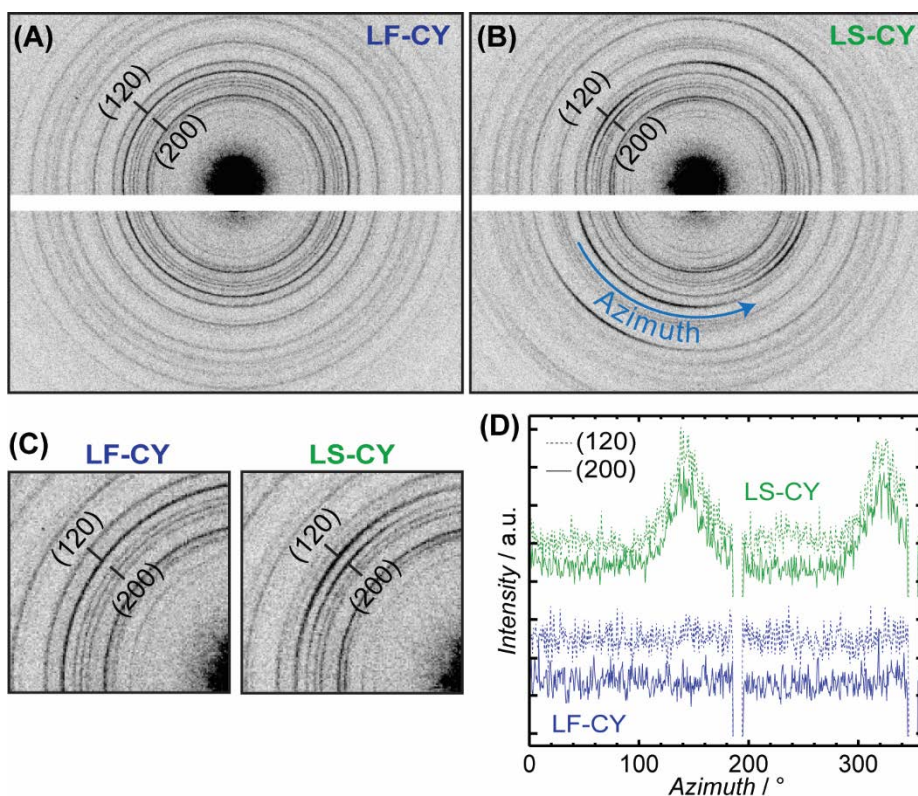


Figure 3-12. Diffraction images for areas rich in A) LF-CY and B) LS-CY and C) zoomed images showing the reflections (200) and (120) of monoclinic  $\text{PbCr}_{1-x}\text{S}_x\text{O}_4$ . D)  $2\theta$ -integrated diffraction intensity as a function of the azimuth ( $\gamma$ ) for reflections (200), full lines, and (120), dashed lines.

In an ideal powder all crystallites are assumed to be randomly oriented giving rise to homogenous Debye rings. When particular orientations are preferred over others, anisotropic diffraction signals are obtained and some reflections may even completely disappear.

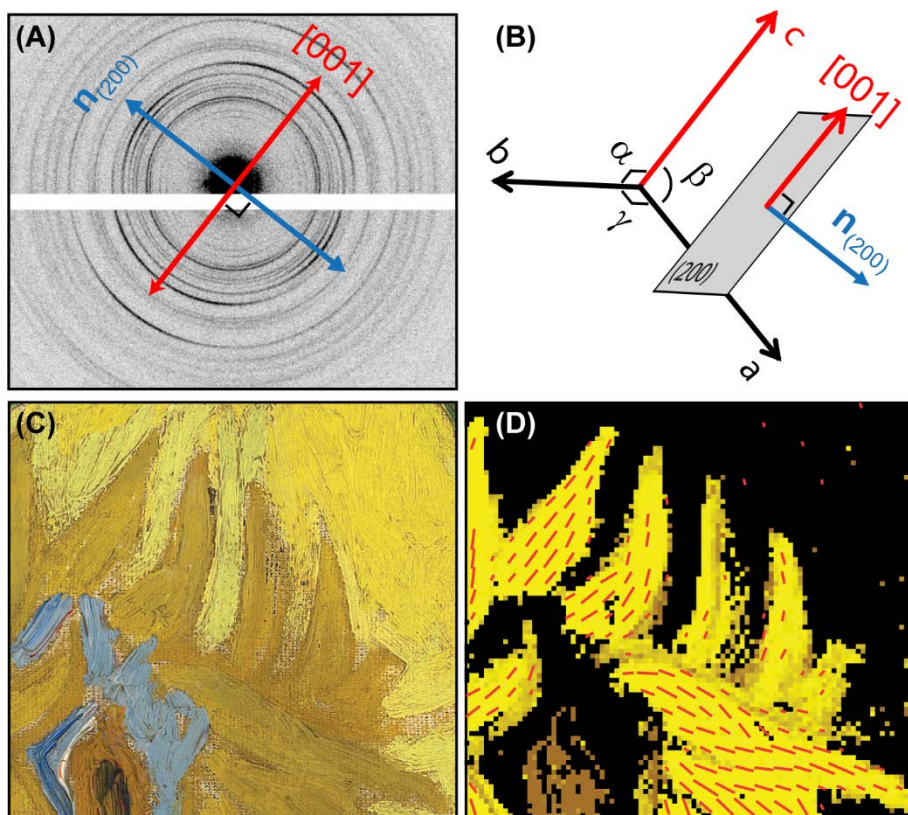


Figure 3-13. A) Surface normal,  $\mathbf{n}_{(200)}$ , oriented along the preferred orientation direction and the  $[001]$  direction projected onto the diffraction image collected in a LS-CY rich region. B) Schematic illustration of a monoclinic  $\text{PbCr}_{1-x}\text{S}_x\text{O}_4$  unit cell showing the  $(200)$  plane with surface normal,  $\mathbf{n}_{(200)}$ , and direction  $[001]$ . C) Photograph image of a detail of *Sunflowers* showing the brush strokes made by Van Gogh. D) Vector plot showing the projected  $[001]$  direction of LS-CY crystallites onto the paint surface (red lines).

In the diffraction images obtained on *Sunflowers*, it can be seen that LF-CY produces homogenous Debye rings (i.e., no preferred orientation, Figure 3-12A), while the diffraction circles of LS-CY show clear intensity maxima arising from preferred orientation of the LS-CY crystallites (see  $(120)$  and  $(200)$  reflections in Figure 3-12B). As shown in Figure 3-12D, both the  $(120)$  and  $(200)$  reflections of

LS-CY exhibit intensity maxima at the same azimuthal angle  $\gamma$  (at  $\gamma = 143^\circ$  and  $\gamma = 322^\circ$ ) indicating that the projections of the normal vectors of these planes are oriented in a similar manner onto the surface of the area detector, and thus onto the painting surface. Since the normals of the (200) and (120) planes (i.e., the [100] and [120] directions) are orthogonal to the [001] direction, it is possible to employ the observed preferred orientation to determine the projected orientation of the c-axis of the LS-CY crystals in Van Gogh's brush strokes (see Figure 3-13A and B). As shown in Figure 3-13D (field of red lines) this orientation follows the brush stroke direction of the yellow petals (Figure 3-13C).

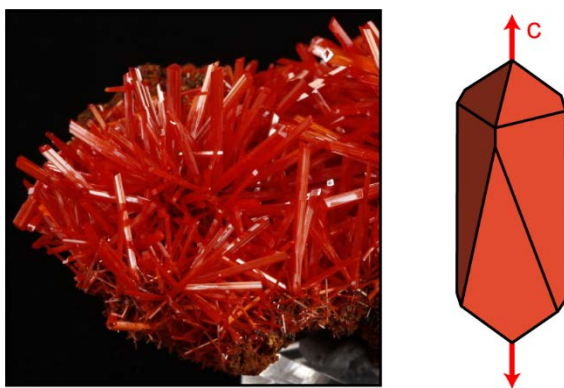


Figure 3-14. Photograph of the mineral crocoite and schematic morphology of a single crocoite crystal.

Crocoite crystals found in nature typically have long prismatic or rod-like shapes, elongated along the c-axis ([001] direction) as shown Figure 3-14. Synthesized CYs with a monoclinic  $\text{PbCr}_{1-x}\text{S}_x\text{O}_4$  composition similarly feature long rod-like shaped crystals [2,5]. We assume that the orientation of the elongated crystal rods becomes established during the (energetic) application of the viscous paint and may potentially be a unique feature characterizing Van Gogh's paint handling. Although for a more complete understanding of the three-dimensional orientation of the LS-CY grains the painting would need to be analyzed under

multiple angles, it seems reasonable to assume that these long crystals preferably lay flat in the paint layer ([001] in-plane) and are not standing upright ([001] out-of-plane). The lack of preferred orientation for LF-CY might indicate a different crystallite size of the pigment material or a different viscosity of these paint.

### 3.4. CONCLUSIONS

The ability to noninvasively visualize the distribution of different subtypes of the CY pigment that are chemically and in terms of color fairly similar, even when present in mixtures with multiple other pigments, allowed for the clear identification of two distinct types of monoclinic CY used by Van Gogh in *Sunflowers*: light-fast  $\text{PbCrO}_4$  and light-sensitive  $\text{PbCr}_{1-x}\text{S}_x\text{O}_4$  ( $x \approx 0.5$ ). The latter is present throughout more than 50% of the CY regions. Nowhere in the examined areas, orthorhombic CY varieties, very prone to light induced darkening, were encountered. Both CYs were often found mixed with other pigments, some of which (e.g., zinc white) are believed to influence the CY darkening phenomenon [9,16]. These findings permit to highlight the areas of the painting with increased risk of darkening and which should be carefully monitored in the future. Visualization of different CYs and their admixed pigments can also assist in digital reconstruction of the original colors used by Van Gogh [17,18]. Data on the preferred orientation of LS-CY crystallites can be linked to the direction of Van Gogh's brushstrokes. In future work, exploring this new type of microscopic information can yield new ways to characterize paint materials and may possibly allow to differentiate between original paint and later alterations realized with chemically identical or very similar materials.

## 3.5. SUPPORTING INFORMATION

### 3.5.1. Raman Spectroscopy

Raman analyses were performed in selected spots (n. 35 in total) inside the painting areas scanned by MA-XRPD by employing a portable spectrometer Xantus-2 (Rigaku Corporation, JP). The instrument is equipped with a CCD cooled by a Peltier system. Spectra were recorded with a diode laser source emitting at 785.0 nm (spot diameter: ~0.2 mm) in the 2000-200  $\text{cm}^{-1}$  energy range. The maximum laser power at the painting surface was 8 mW. The exposure time varied between 1 and 2 s, using 1-5 accumulations and about 7-10  $\text{cm}^{-1}$  spectral resolution.

#### 3.5.1.1. Raman results from areas A, B and C

In line with earlier studies [9] and the MA-XRPD results (Figure 3-5 and Figure 3-10A), Raman investigations permitted to identify LF-CY (monoclinic  $\text{PbCrO}_4$ ) in the ochreish areas (Figure 3-S-1: pts 03-06) and LS-CY ( $\text{PbCr}_{1-x}\text{S}_x\text{O}_4$ ,  $x \approx 0.5$ ) in the light-yellow petals (points 07-08). The differentiation among the two CY types was possible through the sulfate symmetric stretching mode ( $976 \text{ cm}^{-1}$ ) in combination with the broadening and the wavenumber shift toward higher values for both the chromate symmetric stretching band (from  $841$  to  $844 \text{ cm}^{-1}$ ) and the chromate bending modes (from  $357$  to  $365 \text{ cm}^{-1}$ ) [5,6]. In two locations (points 04-05), Raman measurements show that LF-CY occurs along with minium (signal at  $548 \text{ cm}^{-1}$ ), whereas in another spot (point 06) it is present with vermilion (weak signal at  $253 \text{ cm}^{-1}$ ). The spectrum recorded from an orange-yellow petal (point 10) shows the characteristic signals of LS-CY and chrome orange (CO). The latter compound was found in a mixture with LF-CY in the orange-ochre corolla of a flower (point 09). In the darker and paler blue areas



surrounding this corolla (points 01-02), only the presence of ultramarine could be detected by Raman spectroscopy (band at  $548\text{ cm}^{-1}$ ).

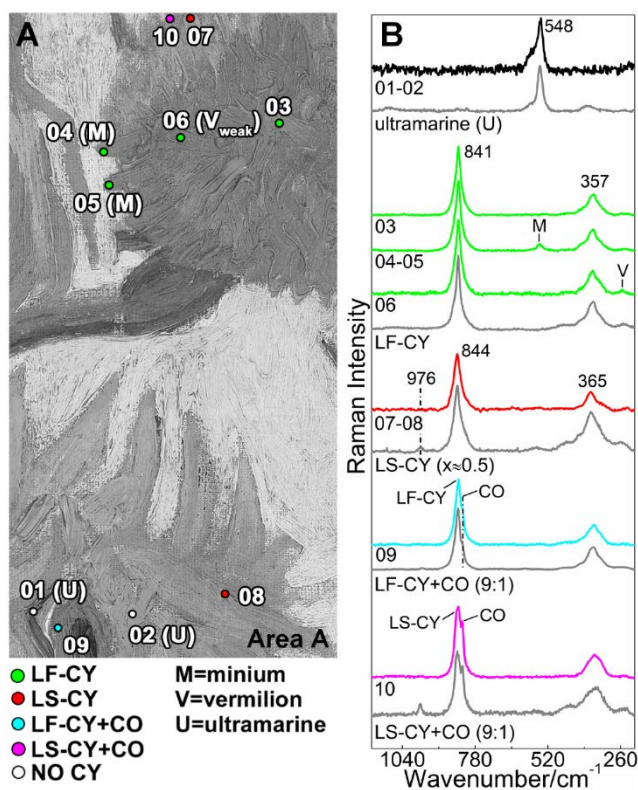


Figure 3-S-1. A) Distribution of Raman spots showing (green) LF-CY (monoclinic  $\text{PbCrO}_4$ ); (red) LS-CY ( $\text{PbCr}_{1-x}\text{S}_x\text{O}_4$ ,  $x \approx 0.5$ ); (cyan) LF-CY+chrome orange (CO); and (magenta) LS-CY+CO. V and M denote the spots where chrome yellow is mixed with vermilion or minium, while white circles indicate the locations where only ultramarine (U) was identified (Figure 3-5 and Figure 3-10A for the corresponding MA-XRPD maps). B) Selection of the Raman spectra acquired from the spots reported in A) and from the corresponding reference compounds (gray lines) [01-02: blue corolla; 03-05(M) and 06(V): ochre-yellow and ochre petals; 07-08: light-yellow petals; 09: orange-ochre corolla; 10: orange-yellow petals].

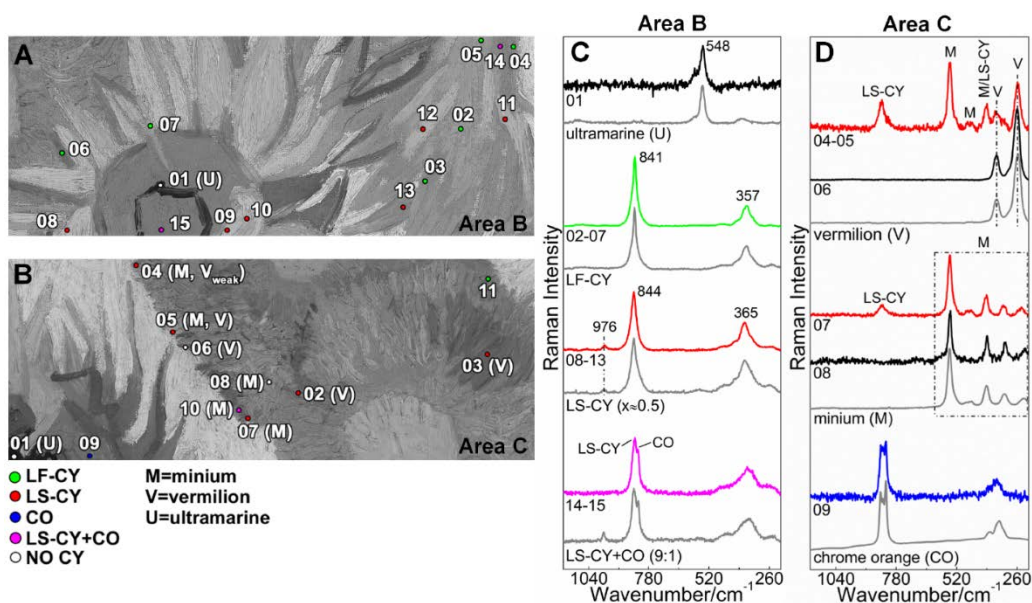


Figure 3-S-2. A,B) Distribution of Raman spots showing (green) LF-CY (monoclinic  $\text{PbCrO}_4$ ); (red) LS-CY ( $\text{PbCr}_{1-x}\text{S}_x\text{O}_4$ ,  $x \approx 0.5$ ); (blue) chrome orange (CO); and (magenta) LS-CY+ CO. V and M denote the spots where chrome yellow is mixed with vermilion and/or minium, while white circles indicate the locations where only ultramarine (U), vermilion (V) or minium (M) were identified (see Figure 3-6 and Figure 3-7 and Figure 3-10B-C for the corresponding MA-XRPD maps). C,D) Selection of the Raman spectra acquired from the spots reported in A,B) and from the corresponding reference compounds (gray lines).

Consistent with the MA-XRPD maps (Figure 3-6 and Figure 3-7 and Figure 3-10B-C) and the results obtained from area A (Figure 3-S-1), Raman investigations of areas B and C show that LF-CY is present in the ochre-yellow tones (Figure 3-S-2A,C: points 02-07; Figure 3-S-2B,D: point 11), while LS-CY is the main constituent of the light-yellow petals (Figure 3-S-2A,C: points 08-13; Figure 3-S-2B,D: points 02-05 and 07). Chrome orange was identified in the orange corolla of a flower (Figure 3-S-2B,D: point 09). This compound was found in mixture with LS-CY in the orange-yellow areas (Figure 3-S-2A,C: points 14-15;

Figure 3-S-2B,D: point 10). In selected ochre-reddish petals (Figure 3-S-2B,D), LS-CY was identified together either with vermilion (points 02-03) or minium (points 07 and 10), while in two other red-orangeish areas the same compound was mixed with both vermilion and minium (points 04-05). Pure vermilion (point 06) or minium (point 08) could be detected in two distinct red petals. In the dark blue corolla areas of the two flowers (Figure 3-S-2A-C: points 01), only ultramarine was identified by Raman spectroscopy.

### **ACKNOWLEDGEMENTS**

The authors acknowledge financial support from BELSPO (Brussels) S2-ART, the NWO (The Hague) Science4Arts ‘ReVisRembrandt’ project, the GOA Project Solarpaint (University of Antwerp Research Council) and the Interreg Smart\*Light project. Raman analyses were performed using the European MOLAB platform, financially supported by the Horizon 2020 Programme (IPERION CH Grant 654028). The authors thank the staff of the Van Gogh Museum for their collaboration.

## REFERENCES

- [1] Monico, L.; Janssens, K.; Cotte, M.; Romani, A.; Sorace, L.; Grazia, C.; Brunetti, B. G.; Miliani, C. *J. Anal. At. Spectrom.* **2015**, *30*, 1500-1510.
- [2] Kühn, H.; Curran, M. In *Artists' Pigments - A Handbook of Their History and Characteristics*, Feller, R. L., Ed.; Archetype Publications: London, 1985.
- [3] Monico, L.; Janssens, K.; Miliani, C.; Van der Snickt, G.; Brunetti, B. G.; Cestelli Guidi, M.; Radepont, M.; Cotte, M. *Anal. Chem.* **2013**, *85*, 860-867.
- [4] Crane, M. J.; Leverett, P.; Shaddick, L. R.; Williams, P. A.; Klopogge, J. T.; Frost, R. L. *Neues Jahrb. Mineral. Monatsh.* **2001**, 505-519.
- [5] Monico, L.; Janssens, K.; Miliani, C.; Brunetti, B. G.; Vagnini, M.; Vanmeert, F.; Falkenberg, G.; Abakumov, A.; Lu, Y.; Tian, H.; Verbeeck, J.; Radepont, M.; Cotte, M.; Hendriks, E.; Geldof, M.; van der Loeff, L.; Salvant, J.; Menu, M. *Anal. Chem.* **2013**, *85*, 851-859.
- [6] Monico, L.; Janssens, K.; Hendriks, E.; Brunetti, B. G.; Miliani, C. *J. Raman Spectrosc.* **2014**, *45*, 1034-1045.
- [7] Tan, H. Y.; Tian, H.; Verbeeck, J.; Monico, L.; Janssens, K.; Van Tendeloo, G. *Angew. Chem.-Int. Edit.* **2013**, *52*, 11360-11363.
- [8] Monico, L.; Van der Snickt, G.; Janssens, K.; De Nolf, W.; Miliani, C.; Verbeeck, J.; Tian, H.; Tan, H.; Dik, J.; Radepont, M.; Cotte, M. *Anal. Chem.* **2011**, *83*, 1214-1223.
- [9] Monico, L.; Janssens, K.; Hendriks, E.; Vanmeert, F.; Van der Snickt, G.; Cotte, M.; Falkenberg, G.; Brunetti, B. G.; Miliani, C. *Angew. Chem.-Int. Edit.* **2015**, *54*, 13923-13927.
- [10] Alfeld, M.; Janssens, K.; Dik, J.; de Nolf, W.; van der Snickt, G. *J. Anal. At. Spectrom.* **2011**, *26*, 899-909.
- [11] Effenberger, H.; Pertlik, F. *Z. Kristallogr.* **1986**, *176*, 75-83.

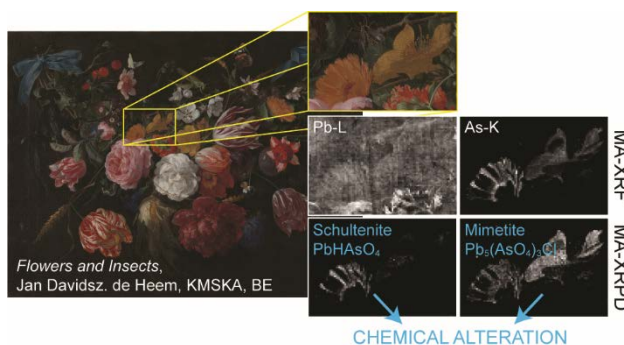
- [12] Chiari, G.; Sarrazin, P.; Heginbotham, A. *Appl. Phys. A: Mater. Sci. Process.* **2016**, *122*.
- [13] Legrand, S.; Vanmeert, F.; Van der Snickt, G.; Alfeld, M.; De Nolf, W.; Dik, J.; Janssens, K. *Heritage Sci.* **2014**, *2*, 13.
- [14] Bertrand, L.; Schoder, S.; Anglos, D.; Breese, M. B. H.; Janssens, K.; Moini, M.; Simon, A. *Trac-Trends Anal. Chem.* **2015**, *66*, 128-145.
- [15] Geldof, M.; Megens, L.; Salvant, J. In *Van Gogh's studio practice*, Vellekoop, M.; Geldof, M.; Hendriks, E.; Jansen, L.; de Tagle, A., Eds.; Mercatorfonds, 2013, pp 238-255.
- [16] Roy, A.; Hendriks, E. *Natl. Gallery Tech. Bull.* **2017**, *37*, 60-77.
- [17] Kirchner, E.; van der Lans, I.; Ligterink, F.; Geldof, M.; Ness Proano Gaibor, A.; Hendriks, E.; Janssens, K.; Delaney, J. *Color Res. Appl.* **2018**, *43*, 158-176.
- [18] Kirchner, E.; van der Lans, I.; Ligterink, F.; Geldof, M.; Megens, L.; Meedendorp, T.; Pilz, K.; Hendriks, E. *Color Res. Appl.* **2018**, *43*, 311-327.

---

# Chapter 4 – *In Situ* Determination of Degradation Products

---

*In this chapter, MA-XRPD is used for the analysis of three 17<sup>th</sup> century still life paintings: two paintings by Jan Davidsz. de Heem (1606-1684) and one copy painting after De Heem by an unknown artist.*



*MA-XRPD allowed to reveal and map the presence of in situ formed alteration products. For this purpose both transmission and reflection modes of MA-XRPD are discussed and estimates for the information depth and sensitivity for various pigments have been made. The possibility of MA-XRPD to allow for noninvasive identification and visualization of alteration products is considered a significant advantage and unique feature of this method. MA-XRPD can thus provide highly relevant information for assessing the conservation state of artworks and could guide possible future restoration treatments.*

This chapter is a modified version of a submitted paper: **Vanmeert, F.**; De Keyser, N.; van Loon, A.; Klaassen, L.; Noble, P.; Janssens, K. “Transmission and reflection mode macroscopic X-ray powder diffraction (MA-XRPD) imaging for the noninvasive visualization of paint alterations in still life paintings by Jan Davidsz. de Heem” In: *Anal. Chem.* **2019**

## 4.1. INTRODUCTION

In the field of cultural heritage, the identification of paint materials (e.g., organic dyes, inorganic pigments and binding media) plays a vital role in solving questions regarding restoration, conservation, dating, authentication of works of art and understanding an artist's *modus operandi*. Furthermore, to evaluate an object's conservation state additional information regarding the *in situ* formation of secondary products is required. Degradation phenomena, and the subsequent discoloration or loss of structural integrity of paint layers that they entail, are often the result of intricate physicochemical processes that are taking place within or at the surface of paint layers. They are triggered by either internal factors, such as the co-presence of mutually incompatible pigment or pigment/binder mixtures, or external factors, such as environmental conditions (relative humidity, light, and temperature), biological activity, volatile organic compounds, pollution or human interventions, or both [1].

In order to gain more profound insights into the nature and relative importance of these phenomena as well as characterize the layer build-up of painted works of art, typically (a small number of) minute paint samples are collected from an artwork. After preparation as cross-sections, these can then be investigated with multiple nondestructive analytical (point-based and microimaging) techniques, such as scanning electron microscopy coupled to energy dispersive X-ray spectroscopy (SEM-EDX) [2], micro Raman [3] and micro Fourier transform infrared ( $\mu$ -FTIR) spectroscopy [4]. In recent years, also various forms of synchrotron radiation based X-ray techniques have been employed for this purpose [5,6]. Frequently, a combination of these techniques is employed to fully understand the underlying chemical processes that have taken place [7]. Although these samples can be a source of highly detailed stratigraphic

information [8] (see also Chapter 6), they originate from only a limited number of (possibly unrepresentative) locations on the artwork.

To expand the detailed analysis of these select samples to entire objects and to include artworks that might be prohibited from sampling, mobile nondestructive spectroscopic methods have been developed. These instruments better fit the constraints imposed by the precious artefacts under analysis. Since the start of their development around 20 years ago, these mobile devices, specifically portable X-ray fluorescence (XRF) and portable Raman spectrometers, are now commonly used on various cultural heritage objects (e.g., paintings, manuscripts, wall paintings, ceramics, sculptures) [9]. In recent years a new trend towards both elemental and chemical imaging techniques capable of visualizing the (often) heterogeneous composition of painted objects on a macroscopic scale can be noted [10]. In this respect, macroscopic (MA-)XRF and visible/near infrared (VNIR) reflectance imaging have so far been the most used spectroscopic imaging techniques, respectively delivering distribution images based on elemental or molecular features [11,12]. Their significance to the cultural heritage field is evidenced by their numerous applications [13-15]. To a lesser extent, also macroscopic FTIR scanning in reflection mode (MA-rFTIR), as well as macroscopic X-ray powder diffraction scanning (MA-XRPD), both capable of delivering detailed chemical information on respectively organic and inorganic species, have been recently described [16-18]. While frequently employed for imaging of microscopic cross-sections, *in situ* Raman imaging on the macro scale remains quite rare [9,19].

In the present chapter, the nature and relevance of the information obtainable by means of reflection and transmission mode MA-XRPD is discussed for paintings in which chemical degradation processes have taken place in the past. For this purpose, the differences and similarities among three 17<sup>th</sup> century oil on canvas



paintings are studied: *Flowers and Insects* (1660-1670), Royal Museum of Fine Arts Antwerp, and *Festoon of Fruit and Flowers* (1660-1670), Rijksmuseum Amsterdam, by Jan Davidsz. de Heem (1606-1684), and a copy painting after De Heem, *Still Life with Fruit and a Lobster* (1665-1700), Rijksmuseum Amsterdam, by an unknown artist, see Figure 4-1. These works were part of a study into the painting techniques of still life paintings by De Heem [20]. Therefore, complementary information was available to correlate with the data obtained with MA-XRPD. In addition to the distribution of various inorganic crystalline pigments, also various alteration products that formed *in situ* on the surface of the paintings or inside the paint layer structure could be identified and mapped. In this context it is relevant to briefly consider the sensitivity and information depth of MA-XRPD for various inorganic pigments in both experimental modes.

## 4.2. EXPERIMENTAL SECTION AND METHODS

### 4.2.1. Still Life paintings

*Flowers and Insects* is a well-preserved oil painting on canvas by the 17<sup>th</sup> century Dutch painter Jan Davidsz. de Heem dated between 1660-1670 (Royal Museum of Fine Arts in Antwerp). It depicts a garland fastened with two blue ribbons displaying various types of flowers, such as tulips, Persian roses, orange marigolds and morning glories, cherries and insects. *Festoon of Fruit and Flowers* by Jan Davidsz. de Heem (Rijksmuseum), executed on a plain weave canvas, has been wax resin lined. This festoon, held together by a blue ribbon, comprises a multitude of fruits, flowers and insects. Below the central pomegranate, a large lemon with greyish-yellow skin is visible. Above the pomegranate, several apricots are part of the composition. The painting *Still life with Fruit and a Lobster* (Rijksmuseum) is part of a series of copies after the signed original in the Gemäldegalerie Alte Meister in Dresden, dated around 1669. Formerly, it was considered an autograph old copy of the master, however there were some substantial differences noted between the painting technique of this painting and Jan Davidsz. de Heem [21]. The still life displays a red lobster meticulously surrounded by a festoon and a wan-li dish filled with fruits on a purplish velvet tablecloth. The yellowish appearance of this painting is the result of a discolored coat of varnish.

In total, four different areas were analyzed with MA-XRF/MA-XRPD in transmission and/or reflection mode as shown in Figure 4-1. Step sizes between 1 and 2 mm in both horizontal and vertical directions with a typical dwell time of 10 s point<sup>-1</sup> were employed to reduce the total scan times (see Table 4-1 for details on all area scans).

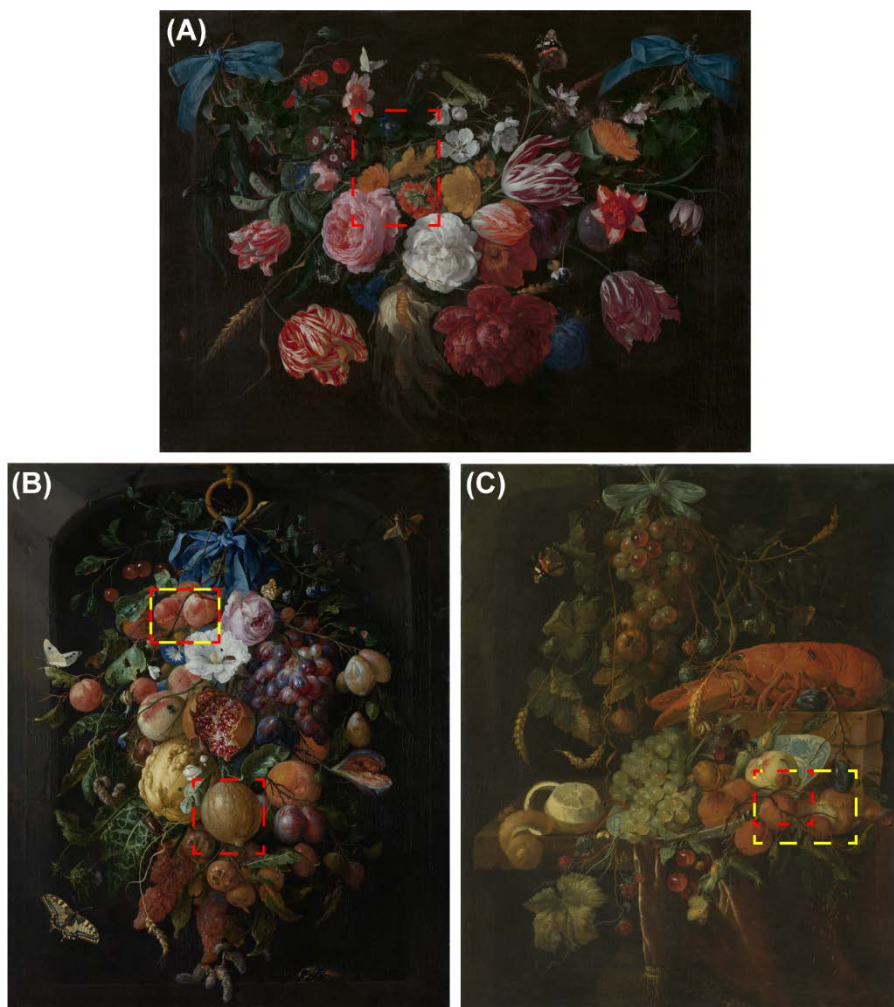


Figure 4-1. (A) Jan Davidsz. de Heem, *Flowers and Insects*, 49 × 67 cm, oil on canvas, 1660-1670, Royal Museum of Fine Arts Antwerp (inv. no. 54), BE, © KMSKA, Lukas - Art in Flanders VZW, Photo: Dominique Provost, (B) Jan Davidsz. de Heem, *Festoon of Fruit and Flowers*, 73.4 × 59.6 cm, oil on canvas, 1660-1670, Rijksmuseum (inv. no. SK-A-138), NL, © Rijksmuseum, and (C) unknown artist, copy after Jan Davidsz. de Heem, *Still Life with Fruit and a Lobster*, 70 × 59 cm, oil on canvas, 1665–1700, Rijksmuseum (inv. no. SK-A-139), NL, © Rijksmuseum. Dashed boxes mark the areas imaged with MA-XRF/MA-XRPD in transmission (red) and reflection mode (yellow).

**Table 4-1. MA-XRF/MA-XRPD scan parameters for the analyzed areas**

<i>Painting Area</i>	Scan Size <sup>a</sup> (mm <sup>2</sup> )	Step Size <sup>a</sup> (mm <sup>2</sup> )	Dwell Time (s point <sup>-1</sup> )	Total Time (h)	Geometry
<i>Flowers and Insects</i>					
Persian Rose	98 × 131	1 × 1	15	64.5	Transmission
<i>Festoon of Fruits and Flowers</i>					
Lemon	93 × 97.5	1.5 × 1.5	10	17.3	Transmission
Apricots	ca. 89 × 69	1.5 × 1.5	10	11.5	Transmission
	ca. 89 × 69	1.4 × 2	10	8.7	Reflection
<i>Still Life with Fruit and a Lobster</i>					
Apricots	ca. 72 × 66	1.5 × 1.5	10	7.4	Transmission
	131 × 92	1 × 2	5	14.9	Reflection

<sup>a</sup> horizontal × vertical

#### 4.2.2. MA-XRF/MA-XRPD instrument

The imaging experiments were carried out using a mobile MA-XRF/MA-XRPD scanning instrument operating in transmission and reflection mode, see Figure 4-2.

In transmission mode, a low power X-ray micro source (44 W, I $\mu$ S-Ag<sup>HB</sup>, Incoatec GmbH, DE) was employed, delivering a monochromatic (Ag-K $\alpha$ ; 22.16 keV) and focused X-ray beam with a photon flux of 1.1 10<sup>7</sup> photon s<sup>-1</sup> (focal spot diameter: 112 (3)  $\mu$ m; output focal distance: 21.6 (1) cm; divergence: 3.8 (3) mrad). Diffraction patterns were recorded with a PILATUS 200K area detector (Dectris Ltd., CH) placed perpendicular to the source at the backside of the painting, see Figure 4-2A-B. The distance between the painting and the area detector was around 11.5 cm, while the distance between the X-ray source collimator and the painting was around 3 cm. The area detector is placed at the output focal distance, so that the diameter of the resulting beam footprint on the painting is around 0.4 mm. For more details, see configuration I2 in Chapter 2.

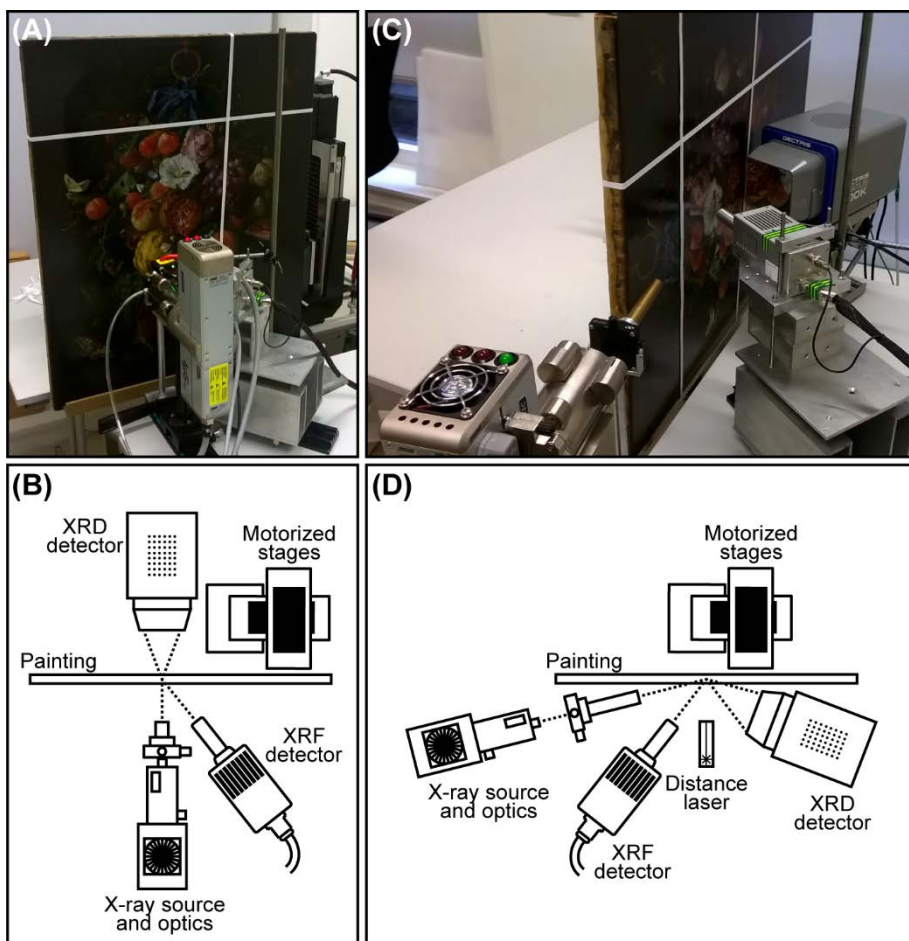


Figure 4-2. Photographs and schematics of the MA-XRF/MA-XRPD scanning instrument in (A-B) transmission and (C-D) reflection mode.

In reflection mode, it becomes difficult to detect diffraction signals at small  $2\theta$  angles because of geometrical constraints. For this reason a similar X-ray micro source (30 W,  $1\mu\text{S-Cu}$ , Incoatec GmbH, DE), but with a lower primary excitation energy ( $\text{Cu-K}\alpha$ ; 8.04 keV) was used as this results in larger scattering angles for the same crystalline material. The source specifications in reflection mode are the following: focal spot diameter of  $313(5)\ \mu\text{m}$ , output focal distance of 39.8 (1) cm, divergence of 2.6 (4) mrad and flux of  $7.0 \cdot 10^8\ \text{photons s}^{-1}$ . An incident angle of  $8^\circ$

was chosen between the primary X-ray beam and the painting's surface, resulting in an enlarged beam footprint of around 2 mm in the horizontal direction; in the vertical direction the beam dimension is around 0.3 mm. As shown in Figure 4-2C-D, the PILATUS detector was positioned on the front side of the artwork with an angle below 30° between the area detector and the painting at a distance of around 0.5 cm from the painted surface. To reduce the effects of local topography and curvature of the painting's surface on the collected diffraction data, the distance between the artwork and the instrument was automatically adjusted with a laser distance sensor (Baumer GmbH, DE) at each measurement point in the scanning process.

In both modes the instrument was equipped with a Vortex-Ex SDD detector (SII, US), collecting X-ray fluorescence radiation from the front side of the painting. The artworks were placed on an easel and mounted on top of three motorized stages to allow for the scanning movement (max. range: 10 cm × 25 cm × 10 cm, Newport Corporation, US). Calibration of several instrumental parameters was performed with a LaB<sub>6</sub> standard for powder diffraction (SRM 660, NIST) or with a calcite paint layer for respectively the transmission and reflection mode.

### 4.2.3. Data processing

Processing of the diffraction data and visualization of the crystalline phase distributions was performed using the XRDU software following the procedure that has been described in section 2.2.7. The diffraction data collected in transmission mode on *Flowers and Insects* and *Still Life with Fruit and a Lobster* has been corrected for minor misalignment of the painting to improve the quality of the distribution images. For this purpose, the apparent shifts in the  $2\theta$  pattern of respectively hydrocerussite and cerussite were used as internal markers to track and correct for the small displacements of the painting relative to the XRD detector (see Eq. 5-1 in Chapter 5) [22]. The PyMca software package was used for

processing of the X-ray fluorescence spectral data [23]. To improve the readability of the final MA-XRF and MA-XRPD distribution images, pixels at the outer edges of the gray scale histograms were avoided by stretching the linear distribution of the white levels using GIMP 2.

#### **4.2.4. Relative sensitivity and information depth**

Depending on the geometry of the MA-XRF/MA-XRPD instrument, information from different depths below the paint surface is obtained. For this reason the information depth of MA-XRPD in transmission and reflection mode has been estimated for various pigments. Additionally, the relative diffracted intensity has been estimated to obtain an indication of the relative sensitivity of the MA-XRF/MA-XRPD instrument for various painters' materials.

##### **4.2.4.1. Relative diffracted intensity**

The relative diffracted intensity ( $RI_{(hkl)}$ ) for various pigments in their respective paint mixtures has been estimated for both transmission and reflection mode. For each pigment the diffracted intensity of the most intense reflection (or multiple reflections if they have a similar scattering angle),  $I_{(hkl)\alpha}$ , was compared to the pigment exhibiting the highest diffracted intensity,  $I_{(hkl)max}$ .

$$RI_{(hkl)\alpha} = \frac{I_{(hkl)\alpha}}{I_{(hkl)max}}$$

The intensity for a given reflection of pigment  $\alpha$  is given by the well-known equation for the intensity diffracted from a crystal phase  $\alpha$  in a multi-component sample; in this case, a crystalline pigment  $\alpha$  in the presence of linseed oil [24]. This intensity is corrected for attenuation of both the primary and the diffracted beam inside the paint sample ( $A_{(hkl)\alpha}$ ), which is different for both experimental modes [25].

$$I_{(hkl)\alpha} = K_e K_{(hkl)\alpha} \frac{v_\alpha}{\mu_m \rho_m} A_{(hkl)\alpha} \quad \text{Eq. 4-1}$$

Here,  $v_\alpha$  is the volume fraction of phase  $\alpha$  in the paint mixture. The attenuation coefficient and density of the mixture (i.e., pigment + oil) depend on the oil absorption of the pigment and are given by respectively  $\mu_m$  and  $\rho_m$ .

$$\mu_m = \omega_\alpha \mu_\alpha + (1 - \omega_\alpha) \mu_{oil}$$

$$\rho_m = \frac{1}{\frac{\omega_\alpha}{\rho_\alpha} + \frac{1 - \omega_\alpha}{\rho_{oil}}}$$

Here,  $\omega_\alpha$  is the weight fraction of phase  $\alpha$  in the paint mixture, while the density of the pigment and oil are respectively given as  $\rho_\alpha$  and  $\rho_{oil}$ . The attenuation coefficients for the pigments ( $\mu_\alpha$ ) and linseed oil ( $\mu_{oil}$ ) were taken from the XCOM database (NIST) [26]. A general structure for linseed oil ( $C_{57}H_{98}O_6$ ), consisting of the triglyceride with linoleic,  $\alpha$ -linoleic and oleic acid, was used. Averaged oil absorption values were taken from the Color of Art Pigment Database (<http://www.artiscreation.com>, accessed October 2018). While  $K_e$  is a constant for a specific experimental system,  $K_{(hkl)\alpha}$  is a constant for a given reflection  $hkl$  of pigment  $\alpha$ :

$$K_{(hkl)\alpha} = \frac{F_{(hkl)\alpha}^2 m_{(hkl)\alpha} LP_{(hkl)\alpha}}{U_\alpha^2}$$

in which  $F_{(hkl)\alpha}$  is the structure factor,  $m_{(hkl)\alpha}$  is the multiplicity and  $LP_{(hkl)\alpha}$  is the Lorentz-Polarization factor for reflection  $hkl$  of pigment  $\alpha$  and  $U_\alpha$  is the unit cell volume of pigment  $\alpha$ .



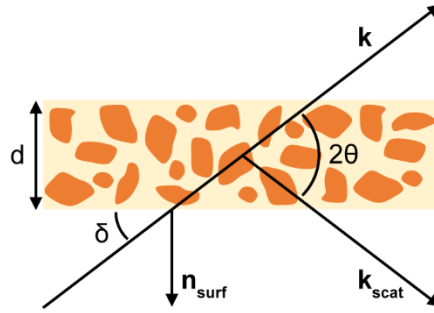


Figure 4-3. Schematic of the primary and diffracted X-ray beam, indicated by the scattering vectors  $\vec{k}$  and  $\vec{k}_{scat}$ , when passing through a simplified paint layer.

The attenuation factors,  $A_{(hkl)\alpha}$ , for transmission (Eq. 4-2) and reflection (Eq. 4-3) mode used in Eq. 4-1 are given by

$$A_{(hkl)\alpha} = C_{trans} \left[ \exp\left(-\frac{\mu_m \rho_m d}{\cos(2\theta)}\right) - \exp(-\mu_m \rho_m d) \right] \quad \text{Eq. 4-2}$$

$$C_{trans} = \left( \frac{\cos(2\theta)}{\cos(2\theta) - 1} \right)$$

$$A_{(hkl)\alpha} = C_{refl} \left[ 1 - \exp\left(-\mu_m \rho_m d \left( \frac{1}{\sin(\delta)} + \frac{1}{\sin(2\theta - \delta)} \right) \right) \right] \quad \text{Eq. 4-3}$$

$$C_{refl} = \left( \frac{\sin(2\theta - \delta)}{\sin(2\theta - \delta) + \sin(\delta)} \right)$$

and depend on the attenuation coefficient and density of the paint mixture, the diffraction angle ( $2\theta$ ) for reflection  $hkl$  of pigment  $\alpha$ , the thickness of the paint layer ( $d$ ) and the incident angle of the primary X-ray beam ( $\delta$ ) for reflection.

The volume fraction of the pigment ( $v_\alpha$ ) in function of its weight fraction ( $w_\alpha$ ) in the pigment-oil paint mixture is given by

$$v_\alpha = \frac{w_\alpha}{w_\alpha + (1 - w_\alpha) \frac{\rho_\alpha}{\rho_{oil}}}$$

## 4.2.4.2. Information depth

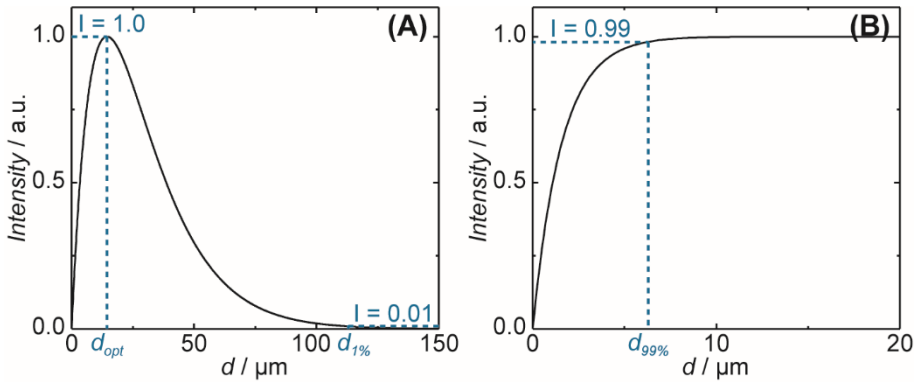


Figure 4-4. Normalized diffracted intensity in function of paint layer thickness ( $d$ ) for (A) transmission and (B) reflection mode.

**Transmission mode**

In transmission mode each paint material has a single thickness for which the highest diffracted intensity is observed, see Figure 4-4A. This ‘optimal thickness’ ( $d_{opt}$ ) can be written as

$$d_{opt} = \frac{\ln(\cos(2\theta))}{\mu_m \rho_m \left[ 1 - \frac{1}{\cos(2\theta)} \right]} \quad \text{Eq. 4-4}$$

Paint layers that exceed this thickness will yield lower diffracted intensities due to increasing attenuation by the sample.

The thickness of a paint layer for which only 1% of the optimal diffracted intensity remains has been defined as the ‘blocking thickness’ ( $d_{1\%}$ ), see Figure 4-4A, and can be calculated iteratively, as

$$d_{1\%} = -\frac{1}{\mu_m \rho_m} \ln \left[ -0.01 K_{opt} + \exp \left( -\frac{\mu_m \rho_m d_{1\%}}{\cos(2\theta)} \right) \right] \quad \text{Eq. 4-5}$$

$$K_{opt} = \exp \left( -\frac{\mu_m \rho_m d_{opt}}{\cos(2\theta)} \right) - \exp(-\mu_m \rho_m d_{opt})$$

Paint layers that exceed this thickness are assumed to absorb all diffracted intensity generated by the sample.

**Reflection mode**

In reflection mode an infinite thickness can be defined for which all primary and diffracted intensity is absorbed by the sample. Paint layers exceeding this thickness will not lead to an increase in the measured diffraction intensity. This ‘infinite thickness’ ( $d_{99\%}$ ) is formulated as the thickness for which the observed diffracted intensity is 99% of the intensity coming from a paint layer that is infinitely thick, see Figure 4-4B, and is given by

$$d_{99\%} = \frac{\ln(100)}{\mu_m \rho_m \left[ \frac{1}{\sin(2\theta - \delta)} + \frac{1}{\sin(\delta)} \right]} \quad \text{Eq. 4-6}$$

**Table 4-2. Relative diffraction intensities and blocking thickness values for the most intense reflection of different pigments and alteration products in transmission mode for Cu-K $\alpha$  and Ag-K $\alpha$  radiation**

Compound	Chemical Formula	Miller indices <sup>a</sup> (hkl)	Oil Absorption <sup>b</sup> (g/100g)	Cu-K $\alpha$		Ag-K $\alpha$			
				2 $\theta$ <sup>a</sup> ( $^{\circ}$ )	d $_{100}$ <sup>d</sup> (mm)	2 $\theta$ <sup>a</sup> ( $^{\circ}$ )	d $_{100}$ <sup>d</sup> (mm)	RI $_{20\mu\text{m}}$ <sup>c</sup> (%)	RI $_{20\mu\text{m}}$ <sup>c</sup> (%)
<i>Pigments</i>									
Bindheimite	Pb <sub>2</sub> Sb <sub>2</sub> O <sub>7</sub>	(222)	14	29.73	0.11	10.69	0.59	100%	100%
Emerald Green	3Cu(AsO <sub>2</sub> ) <sub>2</sub> .Cu(CH <sub>3</sub> COO) <sub>2</sub>	(100)	not given	9.10	0.46	9.88	1.04	95%	37%
Lead Tin Yellow	Pb <sub>2</sub> SnO <sub>4</sub>	(211)(121)	20.5	26.88	0.12	9.56	0.52	58%	53%
Zincite	ZnO	(101)	16	36.26	0.49	9.50	1.16	56%	27%
Cerussite	PbCO <sub>3</sub>	(111)	12.5	24.77	0.12	3.30	0.42	49%	42%
Cinnabar	HgS	(10-1)(101)	8.5	26.52	0.08	8.93	0.30	38%	54%
Minium	Pb <sub>3</sub> O <sub>4</sub>	(211)	7	26.36	0.07	9.69	0.25	36%	61%
Phoenicochroite	PbCrO <sub>4</sub> .PbO	(310)	26	26.29	0.15	9.78	0.62	32%	23%
Hydrocerussite	2PbCO <sub>3</sub> .Pb(OH) <sub>2</sub>	(10-5)	12.5	27.16	0.11	9.79	0.40	28%	26%
Anatase	TiO <sub>2</sub>	(101)	24	25.31	0.30	6.70	5.24	25%	12%
Crocoite	PbCrO <sub>4</sub>	(120)	26	27.19	0.17	10.58	0.74	23%	16%
Calcite	CaCO <sub>3</sub>	(104)	17.5	29.4	0.53	12.98	9.73	21%	9%
Orpiment	As <sub>2</sub> S <sub>3</sub>	(020)	not given	18.51	0.26	7.69	0.94	19%	9%
Rutile	TiO <sub>2</sub>	(110)	24	27.44	0.28	9.32	5.02	18%	9%
Realgar	As <sub>4</sub> S <sub>4</sub>	(120)	not given	16.38	0.26	11.24	0.83	15%	7%
Azurite	2CuCO <sub>3</sub> .Cu(OH) <sub>2</sub>	(111)	23	25.18	1.09	9.47	2.69	15%	6%
Malachite	CuCO <sub>3</sub> .Cu(OH) <sub>2</sub>	(-201)	22 <sup>e</sup>	31.30	1.01	9.12	2.52	13%	5%
Barite	BaSO <sub>4</sub>	(121) - (021) <sup>f</sup>	20	28.75	0.15	8.66	2.37	11%	8%

Table 4-2. Continued

Compound	Chemical Formula	Miller indices <sup>a</sup> (hkl)	Oil Absorption <sup>b</sup> (g/100g)	$2\theta^a$ (°)	Cu-K $\alpha$ d <sub>1%</sub> <sup>d</sup> (mm)	RI <sub>20<math>\mu</math>m</sub> <sup>c</sup> (%)	$2\theta^a$ (°)	Ag-K $\alpha$ d <sub>1%</sub> <sup>d</sup> (mm)	RI <sub>20<math>\mu</math>m</sub> <sup>c</sup> (%)
Gypsum	CaSO <sub>4</sub> ·2H <sub>2</sub> O	(021)	20	20.73	0.74	10%	11.98	13.46	4%
Hematite	Fe <sub>2</sub> O <sub>3</sub>	(104)	46	33.12	0.22	10%	7.49	3.73	7%
Lazurite	Na <sub>4</sub> Ca <sub>4</sub> Al <sub>6</sub> Si <sub>6</sub> O <sub>24</sub> S <sub>2</sub>	(133)(119)(220)	32.5	24.01	0.88	10%	5.93	16.30	3%
Goethite	$\alpha$ -FeOOH	(110)	35.5	21.27	0.23	9%	11.41	3.74	6%
Hydroxylapatite	Ca <sub>10</sub> (PO <sub>4</sub> ) <sub>6</sub> (OH) <sub>2</sub>	(211)(121)	50	31.76	0.68	7%	9.08	12.67	3%
<i>Alteration products</i>									
Arsenolite	As <sub>2</sub> O <sub>3</sub>	(222)	N/A	27.89	0.32	69%	9.49	0.77	30%
Schultenite	PbHAsO <sub>4</sub>	(-111)(020)	N/A	26.34	0.08	36%	10.04	0.27	36%
Palmierite	K <sub>2</sub> Pb(SO <sub>4</sub> ) <sub>2</sub>	(10-5)	N/A	28.42	0.12	29%	10.23	0.57	22%
Mimetite	Pb <sub>5</sub> (AsO <sub>4</sub> ) <sub>3</sub> Cl	(211)(121)	N/A	29.28	0.06	18%	10.53	0.21	29%
Anglesite	PbSO <sub>4</sub>	(121)	N/A	29.69	0.07	13%	7.52	0.26	12%
Syngenite	K <sub>2</sub> Ca(SO <sub>4</sub> ) <sub>2</sub> ·H <sub>2</sub> O	(-112)(220)	N/A	31.30	0.35	7%	11.24	6.67	5%

<sup>a</sup> for most intense reflection; in case more reflections have a similar  $2\theta$  value, all reflections for this scattering angle are used

<sup>b</sup> grams of oil per 100 grams of pigment; averaged values from "Color of Art Pigment Database", accessed October 2018

<sup>c</sup> calculated for a paint layer with a thickness of 20  $\mu$ m: pigment + linseed oil (when oil absorption is given)

<sup>d</sup> blocking thickness, see Eq. 4-5

<sup>e</sup> value for green verditer

<sup>f</sup> reflection used for respectively Cu-K $\alpha$  and Ag-K $\alpha$

**Table 4-3. Relative diffraction intensities and infinite thickness values for the most intense reflection of different pigments and alteration products in reflection mode for Cu-K $\alpha$  and Ag-K $\alpha$  radiation**

Compound	Chemical Formula	Miller indices <sup>a</sup> (hkl)	Oil Absorption <sup>b</sup> (g/100g)	Cu-K $\alpha$		Ag-K $\alpha$			
				$2\theta^a$ ( $^\circ$ )	$d_{99\%}^e$ ( $\mu\text{m}$ )	$RI_{20\mu\text{m}}^c$ (%)	$2\theta^a$ ( $^\circ$ )	$d_{99\%}^e$ ( $\mu\text{m}$ )	$RI_{20\mu\text{m}}^c$ (%)
<i>Pigments</i>									
Bindheimite	Pb <sub>2</sub> Sb <sub>2</sub> O <sub>7</sub>	(222)	14	29.73	7	100%	10.69	13	100%
Zincite	ZnO	(101)	16	36.26	35	87%	12.98	38	65%
Lead Tin Yellow	Pb <sub>2</sub> SnO <sub>4</sub>	(211)(121)	20.5	26.88	7	54%	9.69	8	34%
Minium	Pb <sub>3</sub> O <sub>4</sub>	(211)	7	26.36	4	49%	9.50	3	23%
Cinnabar	HgS	(10-1)(101)	8.5	26.52	5	44%	9.56	4	23%
Cerussite	PbCO <sub>3</sub>	(111)	12.5	24.77	7	43%	8.93	4	14%
Calcite	CaCO <sub>3</sub>	(104)	17.5	29.4	34	31%	10.58	201	39%
Phoenicochroite	PbCrO <sub>4</sub> .PbO	(310)	26	26.29	9	29%	9.47	8	15%
Azurite	2CuCO <sub>3</sub> .Cu(OH) <sub>2</sub>	(111)	23	25.18	65	29%	9.08	27	10%
Hydrocerussite	2PbCO <sub>3</sub> .Pb(OH) <sub>2</sub>	(10-5)	12.5	27.16	7	27%	9.78	6	15%
Malachite	CuCO <sub>3</sub> .Cu(OH) <sub>2</sub>	(-201)	22 <sup>8</sup>	31.30	67	27%	11.24	62	16%
Anatase	TiO <sub>2</sub>	(101)	24	25.31	18	25%	9.12	55	35%
Emerald Green	3Cu(AsO <sub>2</sub> ) <sub>2</sub> .Cu(CH <sub>3</sub> COO) <sub>2</sub>	(100)	not given	9.10	5	22%	3.30	/	/
Crocoite	PbCrO <sub>4</sub>	(120)	26	27.19	10	21%	9.79	11	14%
Rutile	TiO <sub>2</sub>	(110)	24	27.44	18	19%	9.88	81	32%
Emerald Green	3Cu(AsO <sub>2</sub> ) <sub>2</sub> .Cu(CH <sub>3</sub> COO) <sub>2</sub>	(-131) <sup>h</sup>	not given	33.41	29	19%	11.98	29	12%
Lazurite	Na <sub>4</sub> Ca <sub>4</sub> Al <sub>6</sub> Si <sub>6</sub> O <sub>24</sub> S <sub>2</sub>	(133)(119)(220)	32.5	24.01	51	17%	8.66	106	13%
Gypsum	CaSO <sub>4</sub> .2H <sub>2</sub> O	(021)	20	20.73	40	16%	7.49	/	/

Table 4-3. Continued

Compound	Chemical Formula	Miller indices <sup>a</sup> (hkl)	Oil Absorption <sup>b</sup> (g/100g)	2θ <sup>a</sup> (°)	Cu-Kα d <sub>99%</sub> <sup>e</sup> (μm)	RI <sub>20μm</sub> <sup>c</sup> (%)	2θ <sup>a</sup> (°)	Ag-Kα d <sub>99%</sub> <sup>e</sup> (μm)	RI <sub>20μm</sub> <sup>c</sup> (%)
Orpiment	As <sub>2</sub> S <sub>3</sub>	(020)	not given	18.51	13	15%	6.70	/	/
Orpiment	As <sub>2</sub> S <sub>3</sub>	(311) <sup>h</sup>	not given	33.00	17	13%	11.84	26	12%
Gypsum	CaSO <sub>4</sub> ·2H <sub>2</sub> O	(041) <sup>h</sup>	20	29.12	47	13%	10.47	269	13%
Hydroxylapatite	Ca <sub>10</sub> (PO <sub>4</sub> ) <sub>6</sub> (OH) <sub>2</sub>	(211)(121)	50	31.76	46	11%	11.41	321	13%
Realgar	As <sub>4</sub> S <sub>4</sub>	(120)	not given	16.38	11	11%	5.93	/	/
Hematite	Fe <sub>2</sub> O <sub>3</sub>	(104)	46	33.12	15	11%	11.88	104	28%
Barite	BaSO <sub>4</sub>	(121) - (021) <sup>i</sup>	20	28.75	10	10%	9.32	28	15%
Goethite	α-FeOOH	(111) <sup>h</sup>	35.5	36.72	16	8%	13.14	124	22%
Goethite	α-FeOOH	(110)	35.5	21.27	13	8%	7.69	/	/
Realgar	As <sub>4</sub> S <sub>4</sub>	(002) <sup>h</sup>	not given	28.22	9	4%	10.16	9	2%
<i>Alteration products</i>									
Arsenolite	As <sub>2</sub> O <sub>3</sub>	(222)	N/A	27.89	20	77%	10.04	13	31%
Schultenite	PbHAsO <sub>4</sub>	(-III)(020)	N/A	26.34	5	42%	9.49	4	19%
Mimetite	Pb <sub>5</sub> (AsO <sub>4</sub> ) <sub>3</sub> Cl	(211)(121)	N/A	29.28	4	33%	10.53	4	22%
Palmierite	K <sub>2</sub> Pb(SO <sub>4</sub> ) <sub>2</sub>	(10-5)	N/A	28.42	8	28%	10.23	10	22%
Anglesite	PbSO <sub>4</sub>	(121)	N/A	29.69	4	19%	10.68	6	14%
Syngenite	K <sub>2</sub> Ca(SO <sub>4</sub> ) <sub>2</sub> ·H <sub>2</sub> O	(-II2)(220)	N/A	31.30	23	8%	11.24	163	15%

<sup>a</sup> for most intense reflection; in case more reflections have a similar 2θ value, all reflections for this scattering angle are used

<sup>b</sup> grams of oil per 100 grams of pigment; averaged values from "Color of Art Pigment Database", accessed October 2018

**Table 4-3. Continued**

---

<sup>c</sup> values calculated for paint mixtures (pigment with linseed oil) when oil absorption is given; otherwise calculated for the mineral

<sup>d</sup> calculated for an incident angle of 8°

<sup>e</sup> infinite thickness, see Eq. 4-6

<sup>f</sup> calculated for a paint layer with a thickness of 20 μm (pigment + linseed oil)

<sup>g</sup> value for green verditer

<sup>h</sup> second most intense reflection (most intense reflection is smaller than 8 degrees 2θ for Ag-K<sub>α</sub>)

<sup>i</sup> reflection used for respectively Cu-K<sub>α</sub> and Ag-K<sub>α</sub>



## 4.3. RESULTS AND DISCUSSION

### 4.3.1. Overview of ground and pigment usage

Previous cross-section examination showed the presence of a double ground for the three paintings [20]. The first layer for *Flowers and Insects* and *Festoon of Fruit and Flowers* has a reddish-brown color and is mainly composed of fine grained red earth pigments and chalk, while the thicker second ground, with a warm greyish-brown color, contains a mixture of lead white, earth pigments and chalk. A different composition for the ground layers was found for *Still Life with Fruit and a Lobster*. Here, a coarsely grained first layer composed of chalk, red earth pigments and large lead white particles, is followed by a thinner grey layer with lead white and bone black particles.

To achieve the lifelike rendering of the different textures of the fruits and flowers, De Heem and his contemporaries disposed of a large set of painter's materials and artistic techniques. Table 4-4 provides a summary relating color, pictorial elements and main pigments employed in the paintings under investigation. Most of these data were previously obtained by means of MA-XRF in combination with microscopic observation and microanalysis of paint samples [20].

No large differences between the two original De Heem paintings and the copy painting were found in terms of pigment usage. Only in the foliage, some pigments were added in addition to those listed in Table 4-4: smalt was detected together with blue verditer in *Festoon of Fruit and Flowers*, while a mixture of a copper pigment with earth pigments was present in the foliage of *Still Life with Fruit and a Lobster*. However, both below and on top of the pictorial paint layers, more subtle distinctions could be revealed by means of MA-XRPD.

**Table 4-4. Overview of pigments used in the three still life paintings based on previous investigations [20]**

Color	Pictorial elements	Main inorganic pigment	Additional pigments/dyes
White	Roses, Irises, Lilies	Lead white $2\text{PbCO}_3 \cdot \text{Pb}(\text{OH})_2$ $\text{PbCO}_3$	Chalk
Red	Tulips, Carnations, Roses	Vermilion $\text{HgS}$	Red lakes, Lead white
Yellow	Lemons, Roses  Corn ear, Acorns	Orpiment $\text{As}_2\text{S}_3$  Yellow ochre $\text{FeO}(\text{OH})$	Lead tin yellow, Yellow lakes, Earth pigments  Yellow lakes
Orange	Peaches, Apricots, Marigolds	Realgar $\text{As}_4\text{S}_4$	Earth pigments, Orpiment, Vermilion
Blue	Ribbons, Cornflowers, Plums	Ultramarine $\text{Na}_4\text{Ca}_4\text{Al}_6\text{Si}_6\text{O}_{24}\text{S}_2$	
Green	Foliage	Blue verditer $2\text{CuCO}_3 \cdot \text{Cu}(\text{OH})_2$	Yellow lakes, Lead tin yellow
Black	Background	Carbon black C	Bone black

### 4.3.2. Transmission versus reflection mode

In transmission mode, the entire painting structure, from the varnish down to the individual paint layers, ground and canvas, is probed by the X-ray beam. In this way, only crystalline material that is either abundantly present throughout the layer structure (e.g., the main component of a thick ground), or that exhibits a high scattering power (e.g., pigments that contain heavy elements, such as Pb and Hg, see Table 4-2) will dominate the diffraction results.

In Figure 4-5, it can be seen that in transmission mode the distributions of lead white (mostly hydrocerussite,  $2\text{PbCO}_3 \cdot \text{Pb}(\text{OH})_2$ ) and chalk (calcite,  $\text{CaCO}_3$ ) are dominated by their presence in the double ground of *Festoon of Fruit and Flowers*: the first ground layer, rich in calcite, clearly shows the weave structure of the canvas, which is less pronounced in the distribution of hydrocerussite present in the second ground layer (calcite and hydrocerussite MA-XRPD maps).

Reflection mode MA-XRPD is more suited for gathering information on (thin) surface layers. In this mode, the X-ray beam impinges upon the painting under a small angle with the surface, resulting in a shallow probing depth: typically  $< 10 \mu\text{m}$  and  $< 50 \mu\text{m}$  for pigments containing respectively ‘heavy’ (e.g., Pb, Hg) and ‘light’ (e.g., Ca, Cu, Zn) elements, see Table 4-3. In this manner, the relative sensitivity for material at the top surface (e.g., pictorial and degradation layers) benefits greatly since the (often thick) ground layer is prevented from dominating the diffraction data.

Indeed, in reflection mode the calcite distribution highlights the green foliage, the acorns and paler areas of the apricots, where chalk has likely been used as a substrate for a yellow lake (calcite MA-XRPD map in Figure 4-5) [20]. In *Still Life with Fruit and a Lobster*, calcite is also found throughout the orange-brown shadow of the wooden box supporting the lobster and in the yellow of the peach,

strongly contrasting its near absence in transmission mode (calcite MA-XRPD maps in Figure 4-6). This indicates that while calcite is not or only sparingly used in the ground of the copy painting, it is a prominent constituent of (some of) the paint layers. A similar finding can be seen for cerussite ( $\text{PbCO}_3$ ), which was only poorly present in the transmission measurements of *Festoon of Fruit and Flowers*, but shows a clear presence in the reflection measurements (cerussite MA-XRPD maps Figure 4-5). In *Still Life with Fruit and a Lobster*, cerussite is abundantly present in the ground layer, but can be correlated to white visual details in reflection mode (cerussite MA-XRPD map in Figure 4-6).

The red vermilion (cinnabar,  $\text{HgS}$ ) has been used in the pictorial layers of the apricots and is visible in both transmission and reflection mode (cinnabar MA-XRPD maps in Figure 4-5 and Figure 4-6) because of its high scattering power (see Table 4-2). On the other hand, the blue color used in the three paintings for the blue ribbon and the morning glories or for the blue plums and the wan-li dish contains ultramarine, see lazurite MA-XRPD maps in Figure 4-5 and Figure 4-6, which, owing to its very low scattering power, is not visible in transmission mode.

Blue verditer, a synthetic copper carbonate ( $2\text{CuCO}_3 \cdot \text{Cu}(\text{OH})_2$ ), is present in the green foliage together with lead-tin yellow (type I,  $\text{Pb}_2\text{SnO}_4$ ) for the brighter greens (azurite and lead tin yellow MA-XRPD maps in Figure 4-5 and Figure 4-6) and is also more clearly visible in reflection mode. While synthetic blue verditer is crystallographically indistinguishable from azurite, light microscopy and SEM analysis revealed a distinct spherical particle shape that is different from the crushed crystal shards expected for the natural azurite pigment [20]. For *Festoon of Fruit and Flowers*, the final green color was obtained by mixing the blue verditer with smalt (Co MA-XRF map, not shown), and a yellow lake [20].

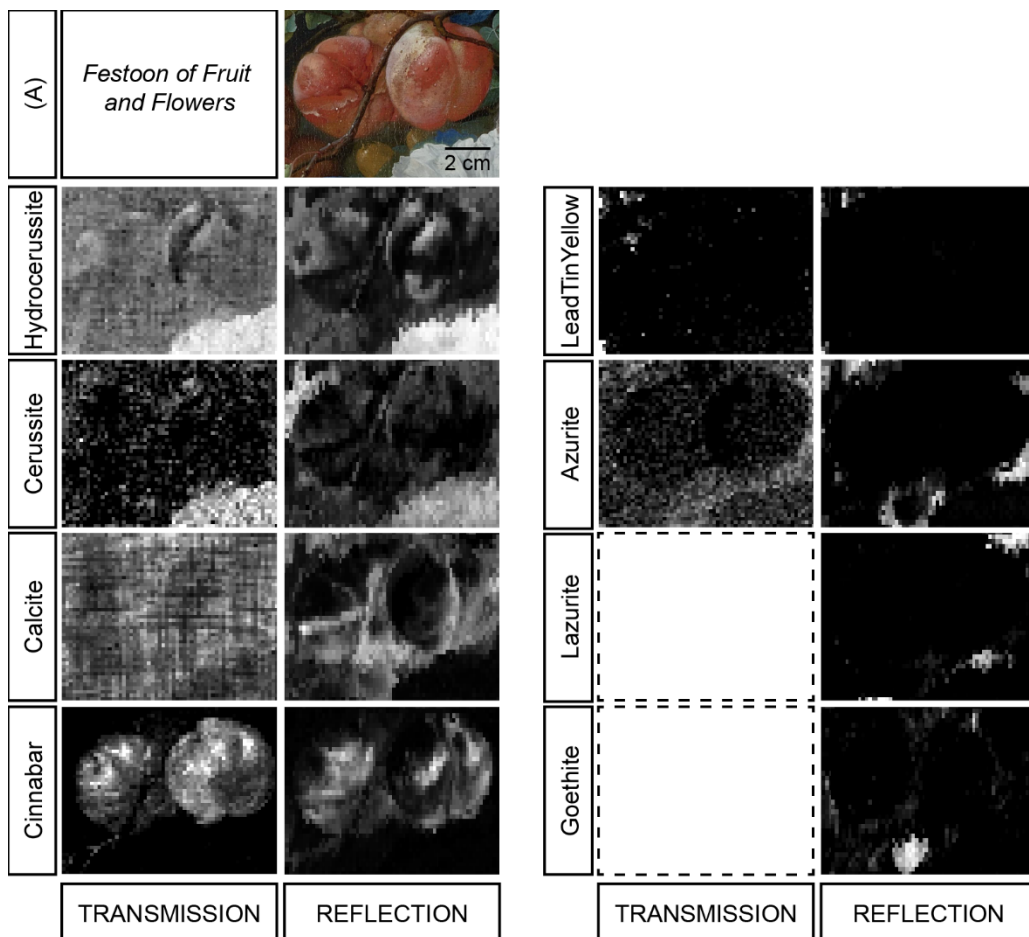


Figure 4-5. Compound-specific distribution images obtained with MA-XRPD from a detail of the apricots in *Festoon of Fruit and Flowers* in both transmission and reflection mode. Brighter colors indicate a higher scaling parameter. Empty dashed boxes indicate compounds that were not detected. Experimental parameters are given in Table 4-1. (A) Optical photograph of the analyzed area.

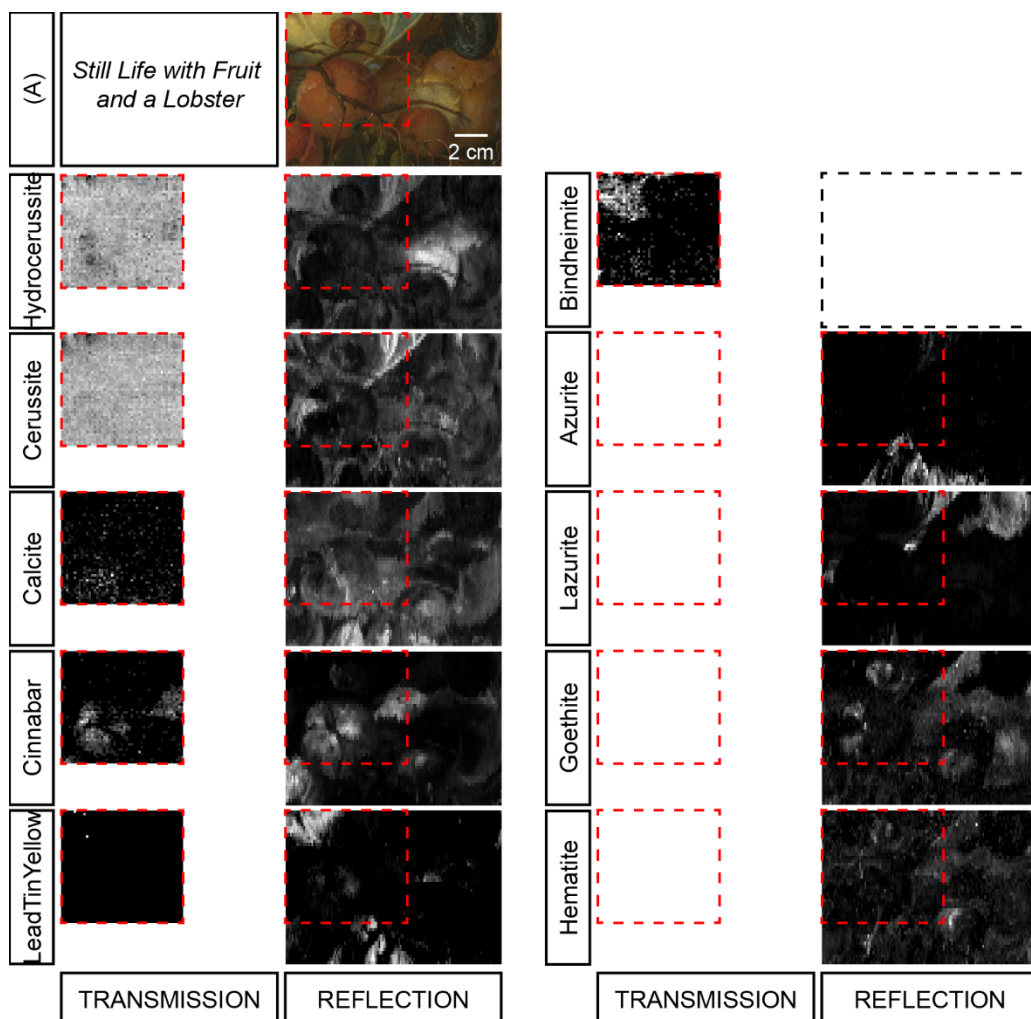


Figure 4-6. Compound-specific distribution images obtained with MA-XRPD from a detail of the apricots in *Still Life with Fruit and a Lobster* in both transmission and reflection mode. Brighter colors indicate a higher scaling parameter. Empty dashed boxes indicate compounds that were not detected. Experimental parameters are given in Table 4-1. (A) Optical photograph of the analyzed area.

Interestingly, Naples yellow, present in the peach of *Still Life with Fruit and a Lobster* (bindheimite MA-XRPD map in Figure 4-6), is not detected in the reflection measurements; in its turn, lead-tin yellow is now clearly present (lead tin yellow MA-XRPD map in Figure 4-6). Indeed, two different yellow layers were used to create the yellow color of the peach: a top layer containing lead-tin yellow, and an underlying layer containing Naples yellow (see Figure 4-S-1 in the Supporting Information) [27]. The difference in the results between the two geometries relates to the different information depth that is probed: the thickness of the upper paint layer, containing lead-tin yellow, is of the same thickness as the information depth in reflection mode ( $< 10 \mu\text{m}$ , see Table 4-3), so that Naples yellow from the underlying layer can no longer be detected. Care should thus be taken when interpreting results obtained in reflection mode, since overlying layers can easily block other pictorial or preparatory layers that lie underneath.

Additionally also earth pigments, such as yellow and red ochre (respectively goethite and hematite), were found in reflection mode, (goethite and hematite MA-XRPD maps in Figure 4-5 and Figure 4-6). While these iron-based pigments are also present in the ground layers, they were not detected with MA-XRPD in transmission mode. This could be the result of a low amount of crystalline material combined with the relatively low sensitivity of MA-XRPD for these iron-based pigments (see Table 4-2).

### 4.3.3. Degradation phenomena

#### 4.3.3.1. Lead arsenates

Arsenic is found in various fruits and flowers depicted throughout the different still life paintings (e.g., in the apricots, the marigold flower, the yellow Persian rose and the lemon) as shown by the As-K MA-XRF maps in Figure 4-7 and Figure 4-8. The presence of arsenic suggests that the artists made use of either the

yellow orpiment ( $\text{As}_2\text{S}_3$ ) or the orange-red realgar ( $\alpha\text{-As}_4\text{S}_4$ ). However, these arsenic sulfide pigments were not detected with MA-XRPD. Instead two rare lead arsenate minerals are encountered: schultenite ( $\text{PbHAsO}_4$ ) and mimetite ( $\text{Pb}_5(\text{AsO}_4)_3\text{Cl}$ ), see Figure 4-9. The presence of these unusual lead arsenates on the surface of these oil paintings is intriguing, as only a handful reports mention these compounds in works of art, and none concern oil paintings.

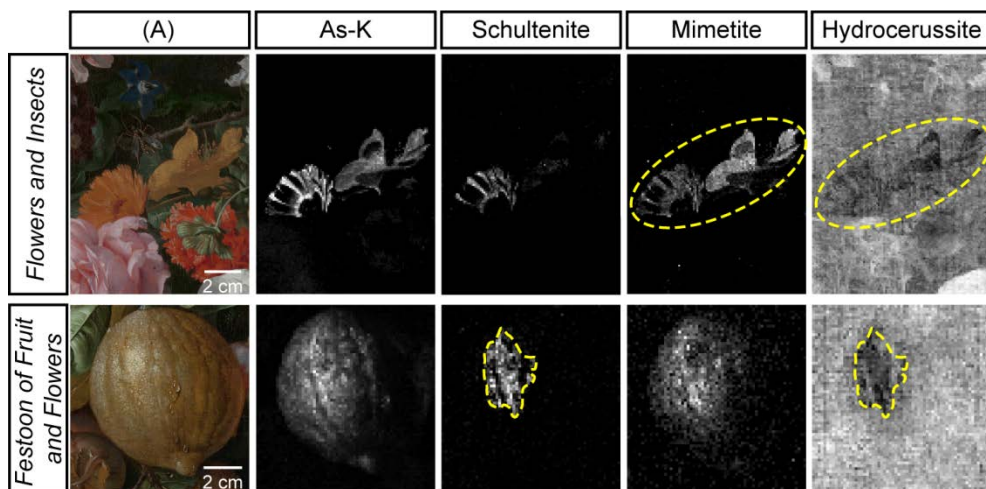


Figure 4-7. Details of (top) *Flowers and Insects* and (bottom) *Festoon of Fruit and Flowers* analyzed with MA-XRF/MA-XRPD in transmission mode. (A) Optical photographs. Elemental distribution images of As-K and compound-specific distribution images of schultenite, mimetite and hydrocerussite. Brighter colors indicate a higher fluorescence intensity (MA-XRF) or scaling parameter (MA-XRPD). Experimental parameters are given in Table 4-1.

Reports on the occurrence of the yellow mineral mimetite as a paint material are limited to three Hellenistic steles from Alexandria [28,29] and several murals [30-32]. In the heavily degraded murals of the church of St. Gallus in Northern Bohemia (13<sup>th</sup> century) mimetite is thought to be a degradation product formed from the interaction between orpiment and red lead ( $\text{Pb}_3\text{O}_4$ ) [33]. The occurrence



of schultenite seems even more unique, but has recently been reported as a degradation product of orpiment, together with arsenolite ( $\text{As}_2\text{O}_3$ ), on a colonial American polychromed chest on stand [34].

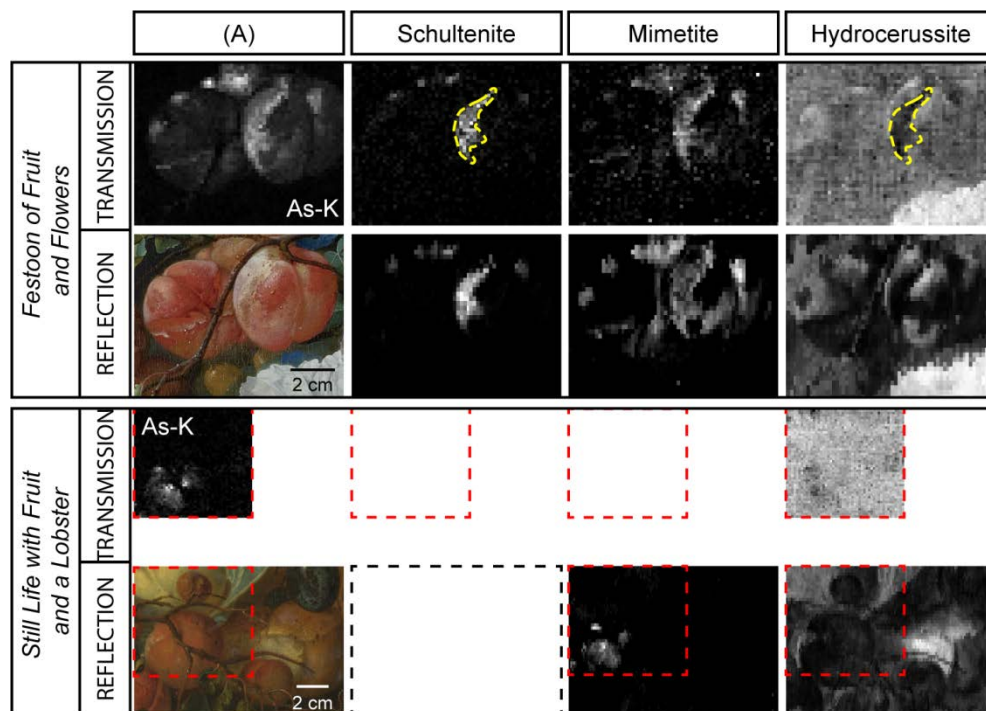


Figure 4-8. Details of (top) *Festoon of Fruit and Flowers* and (bottom) *Still Life with Fruit and a Lobster* analyzed with MA-XRF/MA-XRPD in transmission and reflection mode. (A) Optical photographs and As-K elemental distribution images. Compound-specific distribution images of schultenite, mimetite and hydrocerussite. Brighter colors indicate a higher fluorescence intensity (MA-XRF) or scaling parameter (MA-XRPD). Empty dashed boxes are shown when the respective compound was not detected. Experimental parameters are given in Table 4-1.

Both orpiment and realgar are known to be sensitive to light, causing a fading of their color [35]. This is the result of the photo-oxidation to arsenolite, either

directly as is the case for orpiment, or through an intermediate, pararealgar ( $\text{As}_4\text{S}_4$ ), for realgar [35-38]. Recently it was found that in a subsequent oxidation step arsenolite can be further transformed into soluble arsenates. In their turn, these soluble species can migrate throughout the whole paint system, e.g., into the varnish layer, towards the interface between the paint layers and the ground, until they precipitate with suitable divalent or trivalent cations, such as calcium, lead, copper, aluminum, magnesium and iron [34,39-42].

For this reason, both mimetite and schultenite encountered on the still life paintings are believed to be two of the possible end products of this multi-step alteration process for orpiment and/or realgar. Indeed, a paint sample taken from the lemon of *Festoon of Fruit and Flowers*, which exhibits a brownish appearance with whitish haze, revealed that lead arsenate needles have formed in the top surface of the paint as well as in the ground layer using SEM, ATR-FTIR and As-K edge XANES imaging [40]. It is noteworthy that in the still life paintings discussed here, the distribution of the two arsenates is quite different: schultenite is mainly formed in the lighter (highlighted) areas of the marigold, the lemon and the apricots, while mimetite has a more uniform distribution throughout the As-containing areas that have a greyish appearance (see Figure 4-7 and Figure 4-8). This suggests that the formation of both arsenate minerals takes place in distinct conditions and/or is starting from different parent minerals.

Indeed, depending on the local chemical environment inside the paint layers either mimetite or schultenite formation will be favored. While schultenite is stable only in very acidic environments and with relatively high  $\text{Pb}^{\text{II}}$  and  $\text{As}^{\text{V}}$  concentrations ( $K_{\text{sp},25^\circ\text{C}} \approx 10^{-23} - 10^{-24}$ ), the highly insoluble mimetite ( $K_{\text{sp},25^\circ\text{C}} \approx 10^{-76} - 10^{-83}$ ) can already be formed in slightly acidic conditions with very dilute levels of  $\text{Pb}^{\text{II}}$  and  $\text{As}^{\text{V}}$  [43,44]. The lead white used in the ground and/or paint layers, or

lead that was added as a siccative (e.g., lead oxide) can function as local sources of free  $Pb^{II}$  [45].

Although previous paint sample analysis of the lemon showed intact orpiment particles inside the yellow degraded paint layer [40], neither orpiment nor realgar could be detected by means of MA-XRPD in any of the investigated areas. The low sensitivity of MA-XRPD for the arsenic sulfides, see Table 4-2 and Table 4-3, might be insufficient to detect the diminished quantities of intact  $As_xY_x$  particles. Furthermore, the photo-oxidation products, pararealgar and arsenolite, most commonly associated with orpiment and realgar degradation, are not found. Since the sensitivity of XRPD to detect arsenic oxide is higher or in the same order as for the two lead arsenates, its absence indicates that (almost) all of the arsenic oxide has either undergone further oxidation or is present in the paint system in a dissolved ( $H_3AsO_3$ ) or amorphous form.

The severity of this degradation process, mainly due to its ability to easily migrate throughout the entire paint system, is evidenced in the transmission data on *Flowers and Insects* and *Festoon of Fruit and Flowers*. Indeed, in areas that reveal a strong presence of schultenite or mimetite, the lead white distribution shows a clear loss in intensity (see yellow dashed lines in Figure 4-7 and Figure 4-8). This is not an artefact because of an increase in attenuation of the primary or diffracted X-rays, but evidence of the depletion of lead white in the ground layer in favor of lead arsenate formation.

In the apricots of *Still Life with Fruit and a Lobster* and *Festoon of Fruit and Flowers*, the distribution of mimetite is either only or much more clearly visible in the reflection measurements (mimetite MA-XRPD maps in Figure 4-8), indicating that (most of the) mimetite has manifested itself closely to the surface of these paintings. Since in this case the degradation has taken place only in the

superficial paint layers, the lead white in the underlying ground does not seem to be affected.

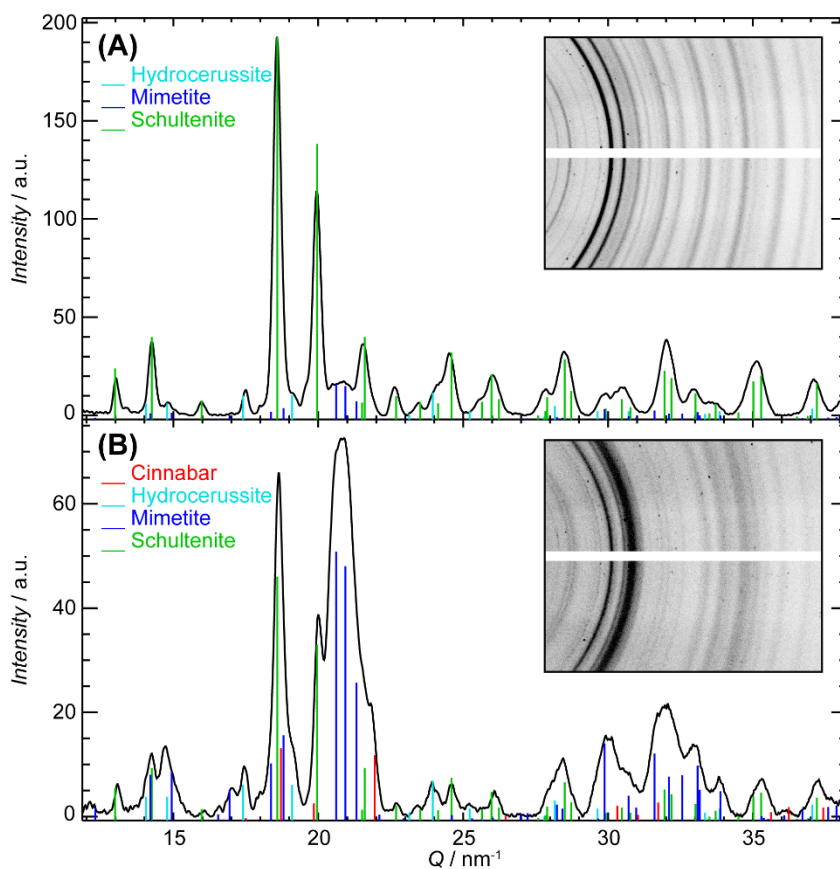


Figure 4-9. X-ray diffractograms and diffraction images of single data points showing the presence of (A) schultenite ( $\text{PbHAsO}_4$ ) and (B) mimetite ( $\text{Pb}_5(\text{AsO}_4)_3\text{Cl}$ ) in the apricots on *Festoon of Fruit and Flowers*.

#### 4.3.3.2. Sulfates

In reflection mode, various (uncommon) secondary sulfates, palmierite ( $K_2Pb(SO_4)_2$ ), syngenite ( $K_2Ca(SO_4)_2 \cdot H_2O$ ) and gypsum ( $CaSO_4 \cdot 2H_2O$ ), are found at the surface of the copy painting *Still Life with Fruit and a Lobster*, while only palmierite is visible on (the surface of) *Flowers and Insects* and *Festoon of Fruit and Flowers* made by De Heem, see Figure 4-10.

Both syngenite and gypsum are frequently encountered weathering products in black crusts and efflorescence layers on stone monuments and mural paintings and as a white haze on medieval (K-rich) glass [46-52]. Potassium and sulfate originate either from internal (e.g., potash glass, K-rich feldspar in granite) or external sources (e.g., fertilizers, K-rich cement, KOH solutions for polychromy removal, dust particles and air pollution) [46,47,53,54]. Depending on the available counter ions, sulfate salts with different composition will readily precipitate at the surface or inside cracks. The mention of syngenite in oil paintings seems very limited in literature: it has been found as a secondary salt in a red-orange Baroque bole ground used for the altar piece *Celebration of St. Roche* [55]. Only rarely, syngenite has been mentioned as a possible raw material in the plaster of a Chinese wall painting, together with calcite, quartz and gypsum [56]. Although gypsum can be an original material in oil paintings (e.g., as *gesso* ground in Southern European panel paintings, or mixed together with orpiment) [57], its widespread presence at the surface of *Still Life with Fruit and a Lobster* seems to indicate its formation as a secondary product.

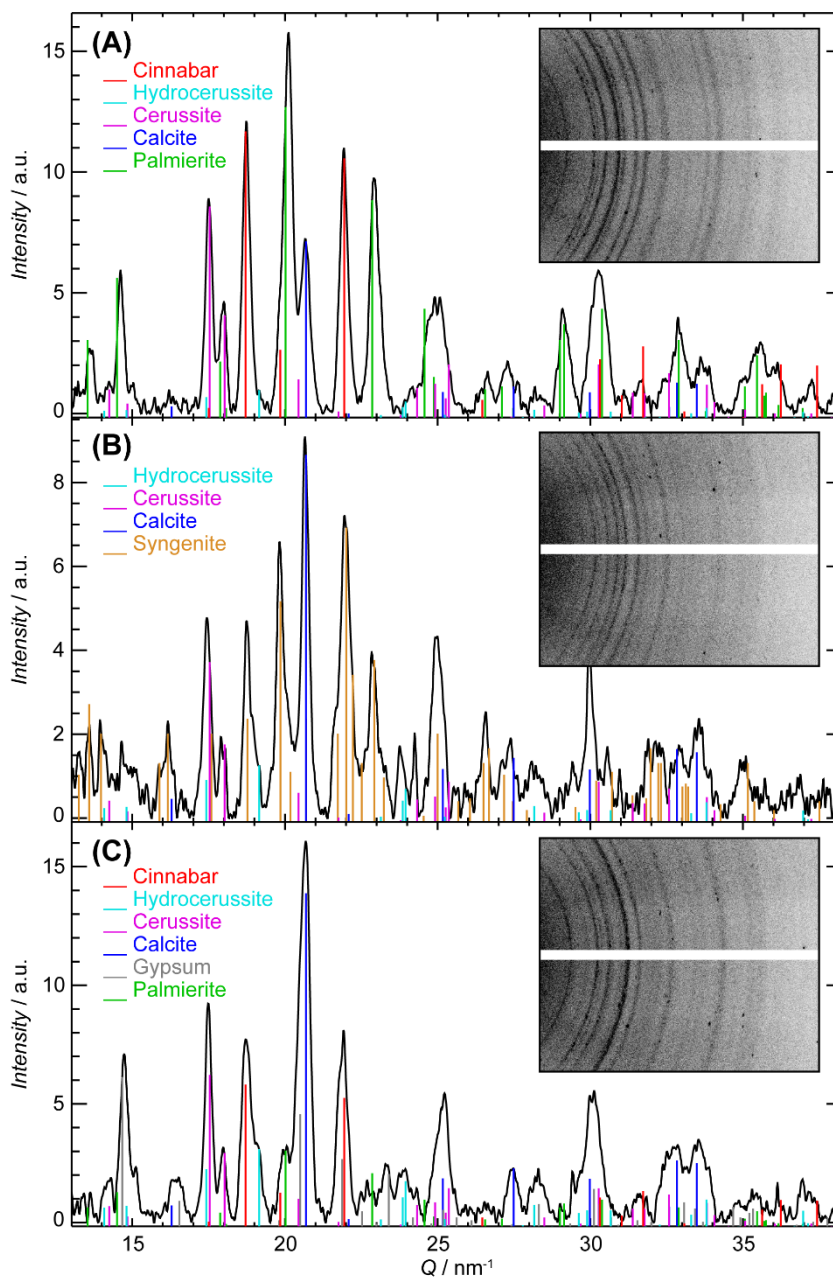


Figure 4-10. X-ray diffractograms and diffraction images of single data points showing the presence of secondary sulfates on *Still Life with Fruit and a Lobster*: (A) palmierite ( $\text{K}_2\text{Pb}(\text{SO}_4)_2$ ), (B) syngenite ( $\text{K}_2\text{Ca}(\text{SO}_4)_2 \cdot \text{H}_2\text{O}$ ) and (C) gypsum ( $\text{CaSO}_4 \cdot 2\text{H}_2\text{O}$ ).







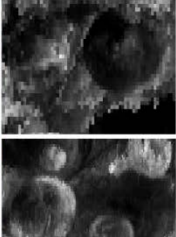
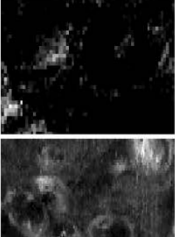
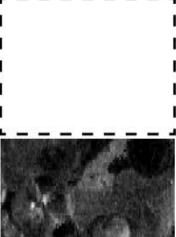






		(A)	K-K	Palmierite	Gypsum	Syngenite
Flowers and Insects	TRANSMISSION					
Festoon of Fruit and Flowers	REFLECTION					
Still Life with Fruit and a Lobster	REFLECTION					

Figure 4-II. Elemental and compound-specific distribution images obtained with MA-XRF/MA-XRPD in transmission or reflection mode from detailed areas of (top) *Flowers and Insects*, (middle) *Festoon of Fruit and Flowers*, and (bottom) *Still Life with Fruit and a Lobster*, showing potassium and several secondary formed (mixed) sulfates. Brighter colors indicate a higher fluorescence intensity (MA-XRF) or scaling parameter (MA-XRPD). Empty dashed boxes are shown when the respective compound was not detected. Experimental parameters are given in Table 4-. (A) Optical photographs of the analyzed areas.

Palmierite, sometimes associated with anglesite ( $\text{PbSO}_4$ ), has been found to a much lesser extent as a secondary sulfate on stone sculptures, medieval glass windows and wall paintings [53,58,59]. On the other hand, palmierite has been identified on several paintings from 17<sup>th</sup> century Old Masters such as Vermeer, Jordaens and Rembrandt [60]. The authors have also encountered palmierite in paint samples from works by Brueghel, Ensor and Rubens; in the latter it was found together with syngenite (unpublished data). The formation of palmierite has been proposed to follow a migration of  $\text{Pb}^{\text{II}}$ , originating from lead white, to the upper paint layers, where it can react with potassium from internal pigment

sources (e.g., smalt, lake substrates and earth pigments) and sulfate from either environmental  $\text{SO}_2$  or substrates such as alum,  $\text{KAl}(\text{SO}_4)_2 \cdot 12\text{H}_2\text{O}$  [60-62]. However, also lead driers could function as a source of free  $\text{Pb}^{\text{II}}$  ions.

In the results described here, the origin for the formation of these salts is twofold. On the one hand, palmierite formation has been confined to those regions where De Heem applied organic lakes. Indeed, in *Festoon of Fruit and Flowers* palmierite seems to have formed only in the orange-red lakes used for the apricots, while in *Flowers and Insects* this salt is present only in the purple primroses (palmierite MA-XRPD maps in Figure 4-II). Here, both potassium and sulfate ions likely originate from potash alum that is a frequently used substrate, especially for red lakes [63]. Surprisingly, while smalt, a K-rich glass already associated to palmierite formation [60,62], is used in the foliage of *Festoon of Fruit and Flowers*, palmierite did not form in this region, indicating the absence of a sulfate source, both internal and external. On the other hand, in *Still Life with Fruit and a Lobster*, syngenite is linked to the darker/shadow regions of the apricots and to the blue plums for which organic lakes have been used, while palmierite and gypsum are found throughout significant parts of the analyzed area (see Figure 4-II bottom row). In regions with a high palmierite signal, gypsum exhibits a low signal and *vice versa*, indicating a possible competition between the two double salts depending on the available internal ions ( $\text{Pb}^{\text{II}}$  or  $\text{Ca}^{\text{II}}$ ). The widespread presence of these two salts suggests that not only local sources, but also atmospheric  $\text{SO}_2$  has played a role in their formation. Next to the potash alum, other internal sources for potassium are present, such as smalt used in the foliage, or ultramarine used in the blue details (e.g. blue plum). This is evidenced by the extent at which potassium is present throughout the imaged areas (see K-K MA-XRF map in Figure 4-II).



## 4.4. CONCLUSIONS

The ability of MA-XRPD for noninvasive and highly specific chemical imaging of paintings has been illustrated on three 17<sup>th</sup> century flower still life paintings. MA-XRPD was used in both transmission and reflection mode. A large variety of inorganic pigments was visualized showing the various materials that were used for the original works by both Jan Davidsz. de Heem and the copy painting. Next to originally applied materials, MA-XRPD in reflection mode revealed several degradation products on (the surface of) the still life paintings. Two different arsenate minerals, schultenite and mimetite, were encountered. They are believed to be the endproducts of the multistep alteration pathway of the arsenic sulfides, orpiment and realgar, and show the strong tendency of arsenate ions to precipitate with Pb<sup>II</sup> ions. Other possible arsenates of Ca<sup>2+</sup>, Cu<sup>2+</sup> and Mg<sup>2+</sup> that have been reported in different art objects were not found [34,41,42,64]. This is consistent with recent findings of lead arsenate with MA-XRPD on other 17<sup>th</sup> century Dutch still life paintings by A. Mignon and M. Nelliuis (not yet published). It is noteworthy that the formation of schultenite is limited to both original paintings. It warrants further investigation that in the copy painting, with a more cerussite-rich lead white ground, this secondary mineral was not found. In addition, a superficial layer consisting of several secondary sulfate salts (palmierite, syngenite and gypsum) covers the entire analyzed area of *Still Life with Fruit and a Lobster*, while only select areas rich in lakes showed the presence of the mixed potassium lead sulfate on *Flowers and Insects* and *Festoon of Fruit and Flowers*. Although this difference could indicate that the copy was made with materials of apparently lower quality, more likely the specific restoration and conservation history of the paintings and the exposures to different atmospheres will have played a crucial role.

The chemical images shown in this study indicate the significant value that MA-XRPD can bring to the field of cultural heritage, not only for the identification of artist's materials, but also for the detection of degradation products and secondary compounds formed within precious works of art. The technique could therefore be a valuable new tool to follow restoration and cleaning treatments *in situ* and to guide sampling campaigns to strategic areas based on the macroscopic distributions of the alteration products. Especially for investigating discoloration phenomena on very delicate works of art on which sampling is often prohibited, such as illuminated manuscripts, MA-XRPD could play an important role. MA-XRPD therefore expands the suit of complementary analytical techniques that are at the disposal of conservation scientists, conservators and art historians.

## 4.5. SUPPORTING INFORMATION

### 4.5.1. Cross-section from *Still Life with Fruit and a Lobster*

The cross-section taken from the yellow part of the peach of *Still Life with Fruit and a Lobster* shows a build-up of four layers (Figure 4-S-1). The first layer contains lead white and bone black particles and is part of a double ground build-up. Unfortunately, the first ground layer is not present in this sample but other samples of this painting demonstrate a thick rich iron-based first ground. On top of the grey second ground layer (1), a layer of lead white mixed with Naples yellow and a few particles of vermilion is found (2). The presence of these pigments were demonstrated with scanning electron microscopy coupled to energy dispersive X-ray spectroscopy (SEM-EDX) analysis, indicating the presence of lead, antimony and mercury. In the third layer (3), SEM-EDX spectra showed the presence of lead and tin, pointing towards the yellow pigment lead tin yellow. Finally, a thick varnish layer (4) follows this layer.

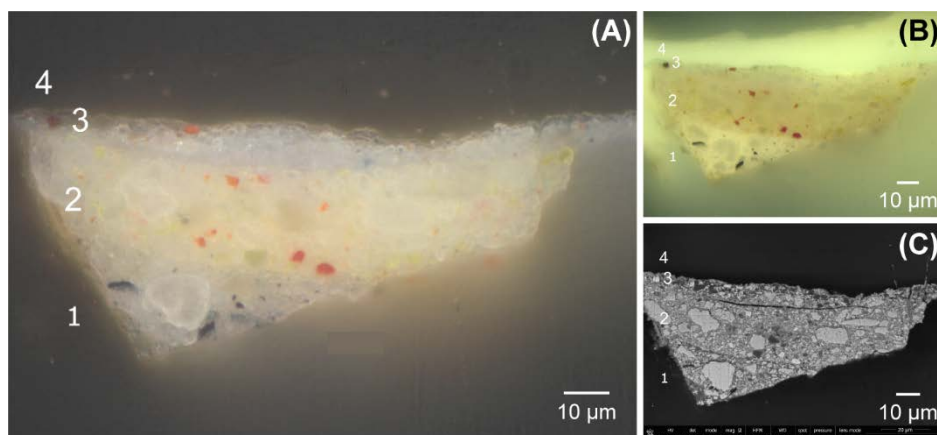


Figure 4-S-1. Light microscopic images (1000x magnification) in (A) Bright field and (B) UV365nm and (C) backscattered electron image of cross-section SK-A-I39\_03 taken in the yellow part of the peach of *Still Life with Fruit and a Lobster*.

## **ACKNOWLEDGMENTS**

The authors acknowledge financial support from BELSPO (Brussels) S2-ART and METOX projects, the NWO (The Hague) Science4Arts ‘ReVisRembrandt’ project and the GOA Project Solarpaint (University of Antwerp Research Council). The authors thank the Rijksmuseum, the Royal Museum of Fine Arts Antwerp, and their staff for the collaborations.

## REFERENCES

- [1] Coccato, A.; Moens, L.; Vandenabeele, P. *Heritage Sci.* **2017**, *5*.
- [2] Schreiner, M.; Melcher, M.; Uhler, K. *Anal. Bioanal. Chem.* **2007**, *387*, 737-747.
- [3] Bersani, D.; Lottici, P. P. *J. Raman Spectrosc.* **2016**, *47*, 499-530.
- [4] Prati, S.; Joseph, E.; Scitutto, G.; Mazzeo, R. *Acc. Chem. Res.* **2010**, *43*, 792-801.
- [5] Janssens, K.; Alfeld, M.; Van der Snickt, G.; De Nolf, W.; Vanmeert, F.; Radepon, M.; Monico, L.; Dik, J.; Cotte, M.; Falkenberg, G.; Miliani, C.; Brunetti, B. G. In *Annual Review of Analytical Chemistry, Vol 6*, Cooks, R. G.; Pemberton, J. E., Eds.; Annual Reviews: Palo Alto, 2013, pp 399-425.
- [6] Bertrand, L.; Cotte, M.; Stampanoni, M.; Thoury, M.; Marone, F.; Schoder, S. *Physics Reports-Review Section of Physics Letters* **2012**, *519*, 51-96.
- [7] Janssens, K.; Van der Snickt, G.; Vanmeert, F.; Legrand, S.; Nuyts, G.; Alfeld, M.; Monico, L.; Anaf, W.; De Nolf, W.; Vermeulen, M.; Verbeeck, J.; De Wael, K. *Top. Curr. Chem.* **2016**, 374.
- [8] De Nolf, W.; Vanmeert, F.; Janssens, K. *J. Appl. Crystallogr.* **2014**, *47*, 1107-1117.
- [9] Lauwers, D.; Brondeel, P.; Moens, L.; Vandenabeele, P. *Philos. Trans. R. Soc. A-Math. Phys. Eng. Sci.* **2016**, *374*, 10.
- [10] Trentelman, K. In *Annual Review of Analytical Chemistry, Vol 10*, Cooks, R. G.; Pemberton, J. E., Eds.; Annual Reviews: Palo Alto, 2017, pp 247-270.
- [11] Alfeld, M.; Janssens, K.; Dik, J.; de Nolf, W.; van der Snickt, G. *J. Anal. At. Spectrom.* **2011**, *26*, 899-909.
- [12] Ricciardi, P.; Delaney, J. K.; Facini, M.; Zeibel, J. G.; Picollo, M.; Lomax, S.; Loew, M. *Angew. Chem.-Int. Edit.* **2012**, *51*, 5607-5610.
- [13] Alfeld, M.; de Viguerie, L. *Spectrochim. Acta, Part B* **2017**, *136*, 81-105.
- [14] Alfeld, M.; Broekaert, J. A. C. *Spectrochim. Acta, Part B* **2013**, *88*, 211-230.
- [15] Cucci, C.; Delaney, J. K.; Picollo, M. *Acc. Chem. Res.* **2016**, *49*, 2070-2079.

- [16] Legrand, S.; Alfeld, M.; Vanmeert, F.; De Nolf, W.; Janssens, K. *Analyst* **2014**, *139*, 2489-2498.
- [17] Dooryhée, E.; Anne, M.; Bardiès, I.; Hodeau, J. L.; Martinetto, P.; Rondot, S.; Salomon, J.; Vaughan, G. B. M.; Walter, P. *Appl. Phys. A* **2005**, *81*, 663-667.
- [18] De Nolf, W.; Dik, J.; Van der Snickt, G.; Wallert, A.; Janssens, K. *J. Anal. At. Spectrom.* **2011**, *26*, 910.
- [19] Casadio, F.; Daher, C.; Bellot-Gurlet, L. *Top. Curr. Chem.* **2016**, *374*.
- [20] De Keyser, N.; Van der Snickt, G.; Van Loon, A.; Legrand, S.; Wallert, A.; Janssens, K. *Heritage Sci.* **2017**, *5*, 13.
- [21] Segal, S.; Helmus, L. *Jan Davidsz de Heem en zijn kring*; SDU: 's-Gravenhage, 1991.
- [22] Vanmeert, F.; Hendriks, E.; Van der Snickt, G.; Monico, L.; Dik, J.; Janssens, K. *Angew. Chem.-Int. Edit.* **2018**, *57*, 7418-7422.
- [23] Sole, V. A.; Papillon, E.; Cotte, M.; Walter, P.; Susini, J. *Spectrochim. Acta, Part B* **2007**, *62*, 63-68.
- [24] Jenkins, R.; Snyder, R. L. *Introduction to X-ray Powder Diffraction*; John Wiley & Sons, Inc., 1996.
- [25] De Nolf, W. *Imaging of crystalline phase distributions by means of scanning and tomographic X-ray powder diffraction*. Ph. D., University of Antwerp, Antwerp, 2013.
- [26] Berger, M. J.; Hubbell, J. H.; Seltzer, S. M.; Chang, J.; Coursey, J. S.; Sukumar, R.; Zucker, D. S.; Olsen, K.; NIST, PML, Radiation Physics Division, 1998.
- [27] Hirayama, A.; Abe, Y.; van Loon, A.; De Keyser, N.; Noble, P.; Vanmeert, F.; Janssens, K.; Tantrakarn, K.; Taniguchi, K.; Nakai, I. *Microchem. J.* **2018**, *138*, 266-272.
- [28] Kakoulli, I. *Stud. Conserv.* **2002**, *47*, 56-67.
- [29] Leona, M. *The Metropolitan Museum of Art Bulletin* **2009**, *67*, 7.

- [30] Buisson, N.; Burlot, D.; Eristov, H.; Eveno, M.; Sarkis, N. *Archaeometry* **2015**, *57*, 1025-1044.
- [31] Holakooei, P.; Karimy, A. H. *J. Archaeol. Sci.* **2015**, *54*, 217-227.
- [32] Brecoulaki, H. *La peinture funéraire de Macédoine: emplois et fonctions de la couleur IVe-IIe s. av. J.-C.*: de Boccard, Paris, 2006.
- [33] Hradil, D.; Hradilova, J.; Bezdicka, P.; Svarcova, S.; Cermakova, Z.; Kosarova, V.; Nemeč, I. *J. Raman Spectrosc.* **2014**, *45*, 848-858.
- [34] Keune, K.; Mass, J.; Meirer, F.; Pottasch, C.; van Loon, A.; Hull, A.; Church, J.; Pouyet, E.; Cotte, M.; Mehta, A. *J. Anal. At. Spectrom.* **2015**, *30*, 813-827.
- [35] FitzHugh, E. W. In *Artists' Pigments A Handbook of Their History and Characteristics*, FitzHugh, E. W., Ed.; Archetype Publications: London, 1997, pp 47-79.
- [36] Douglass, D. L.; Shing, C. C.; Wang, G. *Am. Mineral.* **1992**, *77*, 1266-1274.
- [37] Bindi, L.; Popova, V.; Bonazzi, P. *Can. Mineral.* **2003**, *41*, 1463-1468.
- [38] Kyono, A.; Kimata, M.; Hatta, T. *Am. Mineral.* **2005**, *90*, 1563-1570.
- [39] Vermeulen, M.; Nuyts, G.; Sanyova, J.; Vila, A.; Buti, D.; Suuronen, J. P.; Janssens, K. *J. Anal. At. Spectrom.* **2016**, *31*, 1913-1921.
- [40] Keune, K.; Mass, J.; Mehta, A.; Church, J.; Meirer, F. *Heritage Sci.* **2016**, *4*.
- [41] Holakooei, P.; Karimy, A.-H.; Nafisi, G. *Stud. Conserv.* **2018**, 1-12.
- [42] van Dyke, Y.; Centeno, S. A.; Caro, F.; Frantz, J. H.; Wypyski, M. T. *Heritage Sci.* **2018**, *6*, 9.
- [43] Magalhaes, M. C. F.; Silva, M. C. M. *Monatsh. Chem.* **2003**, *134*, 735-743.
- [44] Sjostedt, C.; Lov, A.; Olivecrona, Z.; Boye, K.; Kleja, D. B. *Appl. Geochem.* **2018**, *92*, 110-120.
- [45] Cotte, M.; Checroun, E.; De Nolf, W.; Taniguchi, Y.; De Viguerie, L.; Burghammer, M.; Walter, P.; Rivard, C.; Salomé, M.; Janssens, K.; Susini, J. *Stud. Conserv.* **2017**, *62*, 2-23.

- [46] Matović, V.; Erić, S.; Kremenović, A.; Colomban, P.; Srećković-Batoćanin, D.; Matović, N. *Journal of Cultural Heritage* **2012**, *13*, 175-186.
- [47] Eric, S.; Matovic, V.; Kremenovic, A.; Colomban, P.; Batocanin, D. S.; Neskovic, M.; Jelikic, A. *Constr. Build. Mater.* **2015**, *98*, 25-34.
- [48] Melcher, M.; Schreiner, M. *J. Non-Cryst. Solids* **2006**, *352*, 368-379.
- [49] Vettori, S.; Bracci, S.; Cantisani, E.; Riminesi, C.; Sacchi, B.; D'Andria, F. *Microchem. J.* **2016**, *128*, 279-287.
- [50] Marszalek, M. *J. Raman Spectrosc.* **2016**, *47*, 1473-1485.
- [51] Newton, R. In *Conservation of Glass*, Newton, R.; Davison, S., Eds.; Butterworth-Heinemann: Oxford, 1989, pp 135-164.
- [52] Garcia-Valles, M.; Gimeno-Torrente, D.; Martinez-Manent, S.; Fernandez-Turiel, J. L. *Am. Mineral.* **2003**, *88*, 1996-2006.
- [53] Prikryl, R.; Svobodova, J.; Zak, K.; Hradil, D. *Eur. J. Mineral.* **2004**, *16*, 609-617.
- [54] Melcher, M.; Schreiner, M.; Kreislova, K. *Physics and Chemistry of Glasses - European Journal of Glass Science and Technology Part B* **2008**, *49*, 346-356.
- [55] Simova, V.; Bezdicka, P.; Hradilova, J.; Hradil, D.; Grygar, T. *Powder Diffraction* **2005**, *20*, 224-229.
- [56] Zeng, Q. G.; Zhang, G. X.; Leung, C. W.; Zuo, J. *Microchem. J.* **2010**, *96*, 330-336.
- [57] Eastaugh, N.; Valentine, W.; Chaplin, T.; Siddall, R. *Pigment Compendium - A dictionary and optical microscopy of historical pigments*; Butterworth-Heinemann, 2008, p 960.
- [58] Sterpenich, J. *Bull. Eng. Geol. Environ.* **2002**, *61*, 179-193.
- [59] Cotte, M.; Susini, J.; Solé, V. A.; Taniguchi, Y.; Chillida, J.; Checroun, E.; Walter, P. *J. Anal. At. Spectrom.* **2008**, *23*, 820.
- [60] Van Loon, A.; Noble, P.; Boon, J. J. In *ICOM Committee for Conservation 16th Triennial Conference: Lisbon, 2011*.



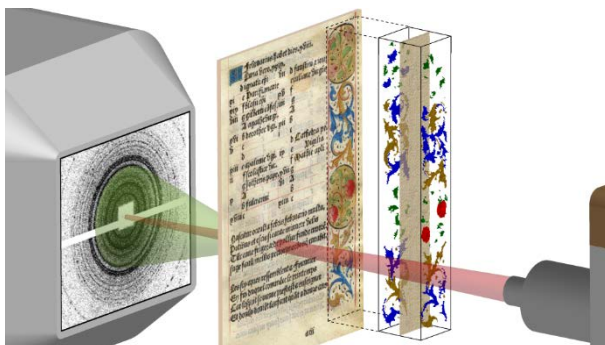
- [61] Boon, J. J.; Oberthaler, E. In *Vermeer, Die Malkunst – Spurensicherung an einem Meisterwerk : Ausstellungskatalog des Kunsthistorischen Museums Wien*, Haag, S.; Oberthaler, E.; Pénot, S., Eds.; Residenz Verlag, 2010, pp 328-335.
- [62] Boon, J. J. *Microsc. Microanal.* **2013**, *19*, 1408-1409.
- [63] Kirby, J.; Spring, M.; Higgitt, C. *Natl. Gallery Tech. Bull.* **2005**, *26*, 71-87.
- [64] Pages-Camagna, S.; Laval, E.; Vigears, D.; Duran, A. *Appl. Phys. A: Mater. Sci. Process.* **2010**, *100*, 671-681.

---

# Chapter 5 – Quantitative and Depth-Selective Analysis

---

*In this chapter, we demonstrate the synergy between the quantitative aspects of powder diffraction and the noninvasive scanning capability of MA-XRPD highlighting the potential of the method to reveal*



*new types of information. Furthermore, on the same artefact, the depth-selective possibilities of the method that stem from an exploitation of the shift of the measured diffraction peaks with respect to reference data are illustrated. The influence of different experimental parameters on the depth-selective analysis results is briefly discussed. Promising stratigraphic information could be obtained, even though the analysis is hampered by not completely understood variations in the unit cell dimensions of the crystalline pigment phases.*

This chapter is a modified version of a published paper: Reprinted with permission from **Vanmeert, F.**; De Nolf, W.; Dik, J.; Janssens, K. “Macroscopic X-ray Powder Diffraction Scanning: Possibilities for Quantitative and Depth-Selective Parchment Analysis” In: *Anal. Chem.* **2018**, *90* (11), 6445-6452. DOI: 10.1021/acs.analchem.8b00241. Copyright 2018 American Chemical Society.

## 5.1. INTRODUCTION

A wealth of information is present at or below the surface of painted works of art. Accessing this stratigraphic information may yield valuable insights into an artist's technique and/or thought process, the conservation history and state of preservation of the work and can uncover underlying compositions. In the last two decades several new photon-based analytical techniques for (sub)surface imaging have been developed that probe the inner structure of painted works and complement traditional X-ray radiography, infrared reflectography and the analysis of cross-sectioned samples [1,2]. Most of these innovative techniques provide curators, conservators and scientists with projected images that do not contain any (valuable) depth information. Indeed, only a limited number allow for some form of depth discrimination: computed tomography and laminography can be used to visualize three-dimensional density variations, optical coherence tomography and terahertz imaging can map interfaces inside the layer stratigraphy, such as between varnishes, glazes and various paint layers, and the local elemental composition at various depths along the layer structure can be probed with confocal X-ray fluorescence. Recently microscale spatially offset Raman spectroscopy (micro-SORS), a powerful technique that can penetrate larger depths compared to confocal RS, has been shown to retrieve molecular information from individual subsurface paint layers in samples from polychrome sculptures [3]. However because of strict experimental requirements, the technique is usually not applied *in situ* and has only recently been applied for imaging of a hidden mock-up [4,5].

X-ray powder diffraction (XRPD) is a well-established technique for the identification of crystalline materials in complex mixtures and is routinely used for the analysis of cultural heritage objects [6]. Analyses with conventional benchtop diffractometers typically require a finely ground homogenized powder

of (a limited amount of) material taken from the artwork. Also Gandolfi cameras can be used to obtain 'powder-like' diffraction data from samples containing only a few single crystals [7]. More recent advances in capillary optics allow for the nondestructive analysis of minute paint samples using microscopic beams inside the laboratory and can be used for the identification of crystalline compounds within individual layers [8-11]. At synchrotron radiation facilities compound-specific distribution images can be obtained with submicrometric spatial resolution revealing the entire, and often complex, sequence of paint and degradation layers [12].

Next to phase identification, XRPD is a powerful tool for the quantitative analysis of crystalline compounds. For precious (and often unique) samples, the analysis is frequently performed using the Rietveld method which does not require the addition of internal standards. Furthermore Rietveld refinement is applicable to mixtures of compounds that exhibit strong diffraction line overlap, as is the case for the various lead carbonates present in the pigment lead white [13]. From the obtained phase fractions, information about the pigment production process can be deduced. It was recently demonstrated that the composition of the lead white pigment, a mixture of the basic and neutral lead carbonates (respectively hydrocerussite and cerussite) changes as a function of the post-synthesis treatment employed [14-16]. For other materials information regarding their provenance and kinetics of degradation mechanisms can be gained by analyzing the mineral abundance [6]. Although the sensitivity and accuracy of laboratory microscopic ( $\mu$ -)XRPD instruments is limited compared to that of conventional benchtop diffractometers, a good estimation of the phase quantities can be obtained in a nondestructive manner [11].

The need for noninvasive analysis, i.e. without taking samples, in the cultural heritage field has driven the development of portable instrumentation. These

portable instruments allow various complementary techniques, such as X-ray fluorescence (XRF), Fourier transform infrared (FTIR), UV-Vis and RAMAN spectroscopy, and XRPD, to be employed without the need to sample or move the object [17]. For portable (p-)XRPD the analysis is restricted to a limited number of points as exposure times of several tens of minutes to one hour are required to obtain useful diffraction data from a single spot [18]; quantitative studies employing p-XRPD instruments have not yet been reported. Innovative noninvasive imaging methods at the macroscale have been developed for *in situ* analyses of flat painted works of art, such as macroscopic (MA-)XRF, MA-reflectance FTIR and hyperspectral full-field imaging [19-21]. To complement these techniques a combined MA-XRF/MA-XRPD scanning instrument has recently been described that is suited for highly-specific pigment mapping of flat painted objects [22]. The instrument typically requires dwell times between 0.2 – 10 seconds (depending on the work of art) to collect X-ray powder diffraction and fluorescence data simultaneously, allowing for macroscopic areas ( $\text{dm}^2$ ) to be imaged as shown in previous chapters.

Analysis of X-ray powder diffraction data largely relies on the accurate determination of the positions of diffraction peaks which are matched to information from reference databases. This is possible only if the sample is placed at a fixed calibrated distance from the diffraction detector. Noninvasive analysis of layered structures allows at most one layer to be placed at the calibrated distance, causing a shift in the measured diffraction peak positions with respect to the reference values for compounds present in other layers. However, this shift can be usefully exploited to calculate the displacement of each compound to the calibrated distance [23,24] and has recently been exploited by Chiari et al using the DUETTO p-XRPD system to determine the thickness of a calcite layer in a single point on a Roman-Egyptian funerary portrait [25].

In this chapter the capability of MA-XRPD for quantitative analysis and for delivering depth-sensitive information that can be linked to the macroscopic distribution images is illustrated on a sheet of parchment from an illuminated 15<sup>th</sup>/16<sup>th</sup> century Book of Tides. The various compound-specific distribution images obtained from this parchment have been discussed in Chapter 2.

## 5.2. EXPERIMENTAL SECTION AND METHODS

### 5.2.1. MA-XRF/MA-XRPD system

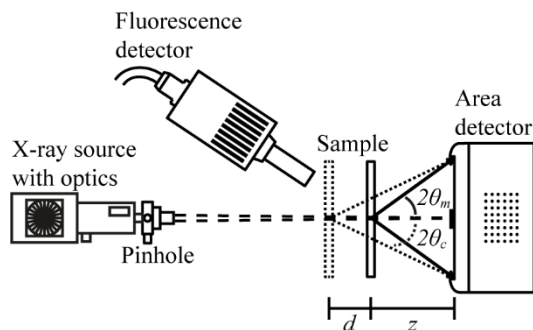


Figure 5-1. Schematic of the combined MA-XRF/MA-XRPD instrument. The dotted lines represent the diffraction signals coming from a sample that shows a displacement ( $d$ ) compared to the calibrated sample-detector distance ( $z$ ).

The combined MA-XRF/MA-XRPD instrument employs a low power Cu-anode X-ray micro source (30 W,  $I_{\mu\text{S-Cu}}$ , Incoatec GmbH, DE) that delivers a monochromatic ( $\text{Cu-K}_{\alpha}$ ) and focused X-ray beam (focal spot diameter:  $313 (5) \mu\text{m}$ ; output focal distance:  $39.8 (1) \text{cm}$ ; divergence:  $2.6 (4) \text{mrad}$ ). A PILATUS 200K detector placed perpendicular to the source at the output focal distance collects diffraction patterns in transmission mode, while fluorescence radiation is simultaneously acquired with a Vortex-EX silicon drift detector (SII, Northridge, CA, US). The parchment was positioned in front of the area detector at a distance of  $2.9 \text{cm}$  (see Figure 5-1). XYZ motorized stages (max. travel ranges:  $10 \text{cm} \times 25 \text{cm} \times 10 \text{cm}$ , Newport Corporation, Irvine, CA, US) allow for the movement of the artwork during the imaging experiment while the instrument remains stationary. A  $\text{LaB}_6$  standard for powder diffraction (SRM 660, NIST) is used for the calibration of the instrument. The analytical characteristics of the combined MA-XRF/MA-XRPD system are reported in Chapter 2 (configuration 9) [22].

## 5.2.2. Data processing

The same data reduction procedure as described in section 2.2.7 was followed. One-dimensional diffraction data shown throughout this chapter is expressed as a function of the scattering vector ( $Q = 2\pi/d = 4\pi \sin(\theta)/\lambda$ ).

## 5.2.3. Illuminated manuscript

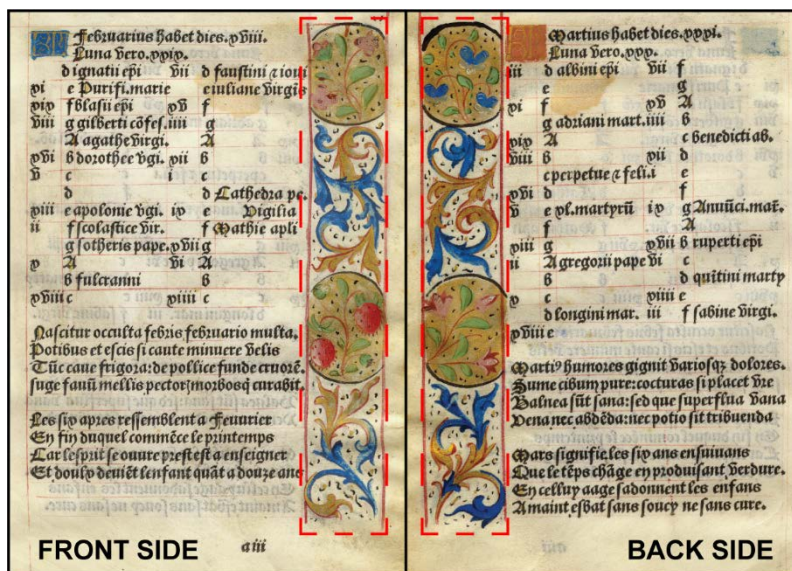


Figure 5-2 Photographs of the front and back side of the illuminated sheet of parchment with markings of the analyzed area (red dashed lines).

The manuscript (private collection) is an excerpt from an illuminated 15<sup>th</sup>/16<sup>th</sup> century Book of Tides and features numerous decorations, see Figure 5-2. In black ink, a Latin text accompanied by a French translation covers most of the parchment. In the margin, colorful vegetal motifs such as strawberries and flowers were applied on both *recto* and *verso* sides. The entire marginal decoration of the illuminated sheet of parchment was imaged using the MA-XRF/MA-XRPD instrument over a period of 8.4 hours (total map size: 137.6 × 22.8 mm<sup>2</sup>; pixel size: 0.4 × 0.4 mm<sup>2</sup>; 344 × 57 pixels; dwell time per point: 0.2 s). Up to twelve different



compound-specific distribution images were revealed in this manner in Chapter 2: azurite ( $2\text{CuCO}_3 \cdot \text{Cu}(\text{OH})_2$ ), malachite ( $\text{CuCO}_3 \cdot \text{Cu}(\text{OH})_2$ ), quartz ( $\text{SiO}_2$ ), barite ( $\text{BaSO}_4$ ), gold ( $\text{Au}^0$ ), cinnabar ( $\text{HgS}$ ), calcite ( $\text{CaCO}_3$ ), gypsum ( $\text{CaSO}_4 \cdot 2\text{H}_2\text{O}$ ), lead tin yellow type I ( $\text{Pb}_2\text{SnO}_4$ ), massicot (*o*- $\text{PbO}$ ), hydrocerussite ( $2\text{PbCO}_3 \cdot \text{Pb}(\text{OH})_2$ ) and cerussite ( $\text{PbCO}_3$ ). The reference diffraction file used for each compound is given in Table 5-1.

**Table 5-1. Overview of reference diffraction files**

Compound	Formula	AMCSD code <sup>a</sup>
Azurite	$2\text{CuCO}_3 \cdot \text{Cu}(\text{OH})_2$	0008598
Malachite	$\text{CuCO}_3 \cdot \text{Cu}(\text{OH})_2$	0010795
Quartz	$\text{SiO}_2$	0006362
Barite	$\text{BaSO}_4$	0005559
Gold	$\text{Au}$	0013108
Cinnabar	$\text{HgS}$	0012137
Calcite	$\text{CaCO}_3$	0000984
Gypsum	$\text{CaSO}_4 \cdot 2\text{H}_2\text{O}$	0011093
Lead Tin Yellow	$\text{Pb}_2\text{SnO}_4$	Gavarri (1981) [26]
Massicot	<i>o</i> - $\text{PbO}$	0010011
Hydrocerussite	$2\text{PbCO}_3 \cdot \text{Pb}(\text{OH})_2$	0010324
Cerussite	$\text{PbCO}_3$	0006304

<sup>a</sup> American Mineralogist Crystal structure database [27]

## 5.3. RESULTS AND DISCUSSION

### 5.3.1. Quantitative information

#### 5.3.1.1. Three types of Lead White

Photographs of the decorated cartouches depicted at the top of the manuscript on the *recto* and *verso* side are given in Figure 5-3A-B. The pink flowers, the white highlights and several blue-greyish areas (marked by red and blue dashed contours) appear together in the cerussite MA-XRPD distribution (Figure 5-3D) indicating that the neutral lead carbonate was used in these pictorial elements. Features from both the *recto* and *verso* side are simultaneously present in the distribution image as MA-XRPD provides superimposed mapping information. The basic lead carbonate, hydrocerussite (HC), is co-localized with cerussite (C), except in the green leaves (marked by green dashed contours) for which a lead white paint was used that only contains HC (Figure 5-3C). Qualitatively it can be seen that (at least) two different lead white mixtures were used based on these compound-specific spatial distribution images for HC and C.

With whole pattern fitting, the relative weight fractions of both carbonates in each point of the image can be determined (see examples given in Figure 5-5). For each individual point in the distribution images, the mass ratio (*MR*) for HC in the lead white pigment was calculated using the relative weight fractions (*w*) of HC and C ( $MR_i = w_i / \sum_i w_i$ ) and the results are shown in the histogram in Figure 5-3F. The histogram was constructed from 1383 individual XRPD patterns. In this histogram one broad distribution around  $MR_{\text{HC}} = 65 \text{ wt}\%$  and one narrow distribution at  $MR_{\text{HC}} = 100 \text{ wt}\%$  can be found indicating the presence of two lead white pigments with different HC-C content.

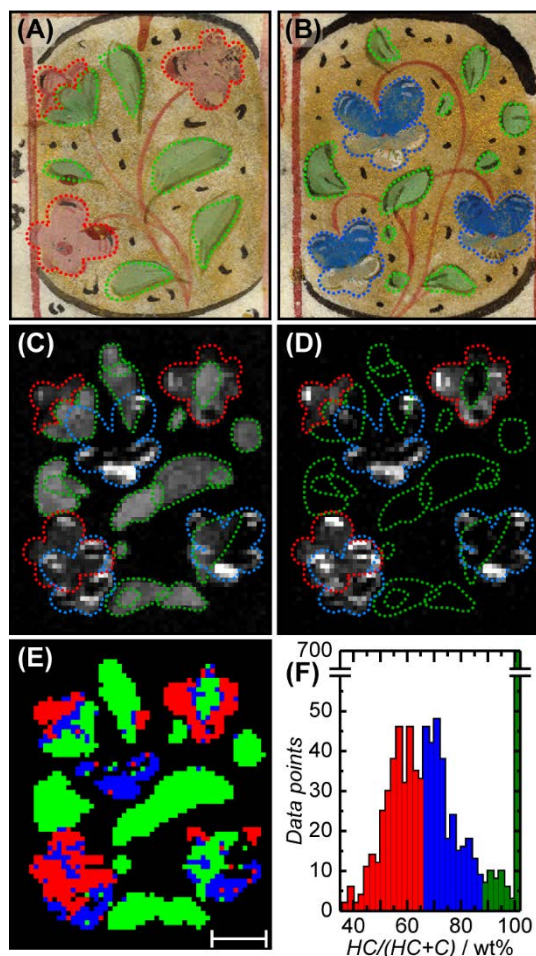


Figure 5-3. Photographs of the top cartouche depicted (A) on the *recto* and (B) *verso* side (mirrored) of the parchment. Compound-specific distribution images obtained for (C) hydrocerussite and (D) cerussite. Lighter grey values indicate a higher scaling parameter. The green, blue and red dashed contours highlight the different pictorial features visible in (A) and (B). (E) False color image of the lead white distribution using the color scheme shown in the histogram (scale bar = 5 mm). (F) Histogram of the HC/(HC+C) mass ratio containing 1383 data points. A threshold based on the hydrocerussite scaling parameter was employed to exclude data points from the histogram in which lead white was not detected.

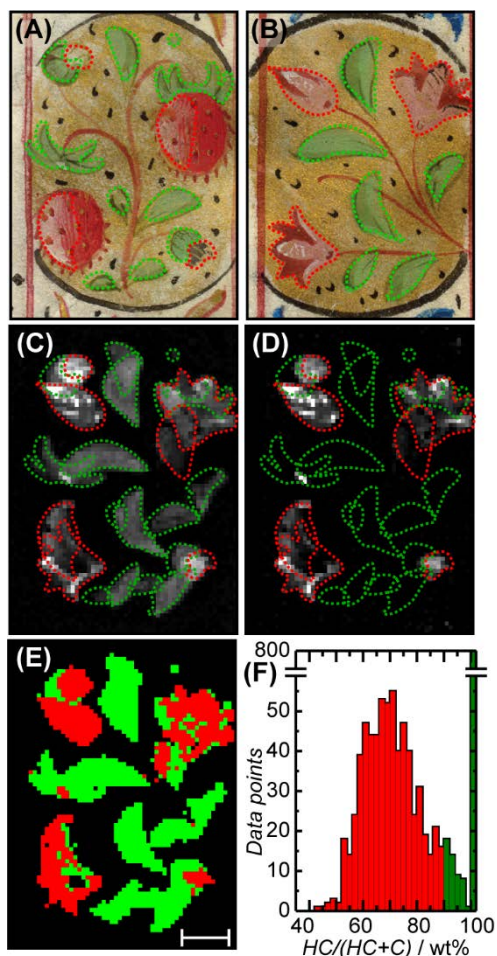


Figure 5-4. Photographs of the bottom cartouche depicted (A) on the front side and (B) on the back side (mirrored) of the parchment. Compound-specific distribution images obtained for (C) hydrocerussite and (D) cerussite. Whiter tones indicate a higher scaling parameter. The green and red dashed contours highlight the different pictorial features visible in (A) and (B). (E) False color image of the lead white distribution using the color scheme shown in the histogram (scale bar = 5 mm). (F) Histogram of the  $HC/(HC+C)$  ratios containing 1523 data points. A threshold based on the hydrocerussite scaling parameter was employed to exclude data points from the histogram in which lead white was not detected.

However, when linking the quantitative information to the macroscopic spatial distribution it becomes clear that in fact (at least) three different types of lead white were used, even though only two distributions are apparent in the histogram. Indeed, the broad mass ratio distribution contains contributions from two different lead white mixtures (shown in red and blue). The false color image shows the distribution of the three different lead white pigments throughout the gilded cartouches (Figure 5-3E). Lead white consisting of only HC was used in the green leaves, while the pink flowers and the blue-greyish regions of the blue flowers have been painted with two different HC-C mixtures. The compositions of the three lead whites are estimated from the histogram to contain  $MR_{HC} = 56 (\pm 6) \text{ wt\%}$  (red),  $74 (\pm 6) \text{ wt\%}$  (blue) and  $100 (\pm 2) \text{ wt\%}$  (green). These compositions are in good agreement with previous HC abundances determined in 16<sup>th</sup> century lead white mixtures [13]. Both cerussite containing pigments correspond to HC abundances consistently found in lead white synthesized following the stack process, while HC-pure lead white is thought to be formed using a very short synthesis time or by heating of the pigment in water [14,16]. Since the *recto* and *verso* sides are measured simultaneously, averaged compositions are obtained for regions that contain lead white on both sides of the parchment (e.g. overlap between the green leaves on the *recto* and the pink flowers on the *verso*, or vice versa) or for those regions in which the different lead white types are adjacent to each other (e.g. the pink flower with the green sepal in the top left corner). These regions also appear as blue in the false color image.

It remains unclear if the broad histogram distributions for the red and blue lead white mixtures are due to the uncertainty on the measured or modelled diffraction intensities, or if paint mixtures with a broad range in HC-C composition have been used. The latter would strongly depend on the lead white manufacturing process which often yielded a product of widely varying purity [28,29]. The quality of lead white also depends on the amount of extender,

such as calcite, that was added to the pigment for economic reasons [14,29]. However, the calcite content within the lead white paint could not be quantified, as calcite is also abundantly present throughout the entire parchment.

In addition to the green leaves and the pink flowers, also the white highlights of the strawberries in the bottom cartouches have been made with lead white. In this case (only) two different lead white mixtures could be distinguished with estimated compositions of  $MR_{HC} = 70 (\pm 9)$  and  $100 (\pm 2)$  wt%, respectively for both the pink flowers and white highlights and the green leaves (see Figure 5-4). Although it seems unlikely that the same pink flowers in the bottom and top cartouche were made with a lead white of different composition, the strong spatial overlap between these flowers (*verso*) and the highlights on the strawberries (*recto*) did not allow for a separate characterization.

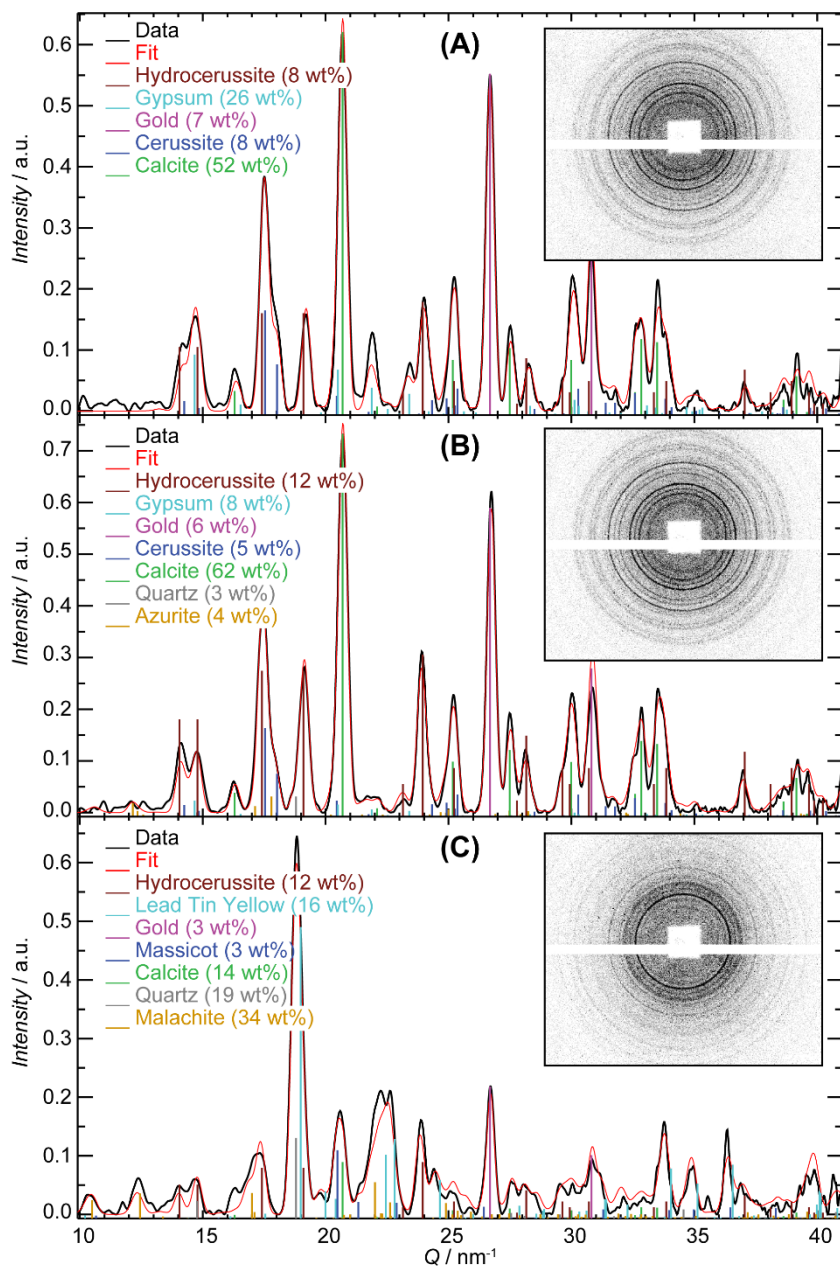


Figure 5-5. X-ray diffractograms and diffraction images of single data points located in (A) a pink corolla, (B) a grey-white highlight and (C) in a green leaf (respectively from the red, blue and green regions in the lead white false color image, Figure 5-3E).

### 5.3.1.2. Two types of Azurite

The blue paint used for the decorative scrollwork and the blue flowers consists of azurite, a copper carbonate frequently used in European painting. Barite and quartz are less common impurities related to azurite owing to its mineralogical origin [30,31] and are found to be co-localized with azurite on the parchment (see Figure 2-14 for more details). It has been suggested that identification of these unusual impurities could play an important role in provenance studies of azurite ore and a recent study has shown that up to four different azurite types can be present on the same manuscript cutting [32].

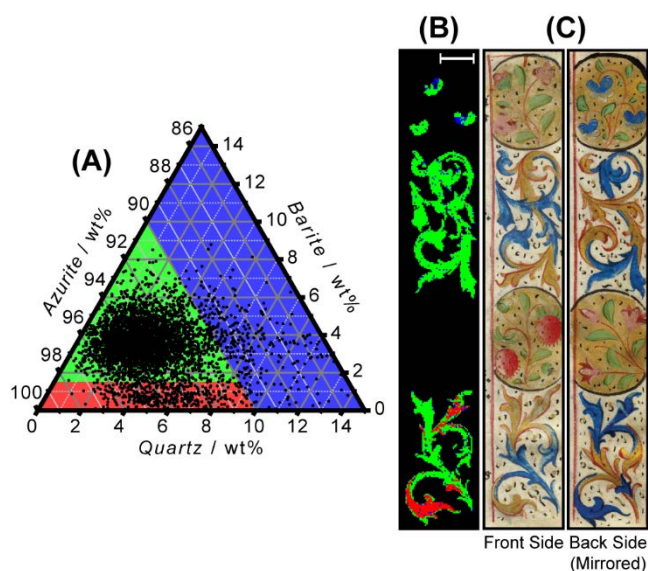


Figure 5-6. (A) Ternary plot of the azurite, barite and quartz mass ratios for the blue color used throughout the parchment. Each of the 4380 data points represents a single pixel in the mapping experiment. A threshold based on the azurite scaling parameter was employed to remove data points in which azurite was not detected. (B) False color image of the azurite distribution using the color scheme shown in the ternary plot (scale bar = 10 mm). (C) Photographs of the marginal decorations on the *recto* and *verso* sides of the parchment.



Figure 5-6 shows the mass ratios for azurite, barite and quartz in the blue paint obtained from 4380 individual XRPD patterns. Two types of azurite were found to be used for the blue decorations. The majority of the blue pigment has a (relatively) high barite content ( $MR_{\text{azurite}} = 93 (\pm 1) \%$ ,  $MR_{\text{barite}} = 4 (\pm 1) \%$  and  $MR_{\text{quartz}} = 3 (\pm 2) \%$ , shown in green) and has been used for the blue flowers and most of the scrollwork. A second type of azurite with no detectable barite and a higher quartz content was only found in some regions of the bottom blue scrollwork on the back side of the parchment ( $MR_{\text{azurite}} = 94 (\pm 2) \%$ ,  $MR_{\text{barite}} = 0.7 (\pm 4) \%$  and  $MR_{\text{quartz}} = 5 (\pm 2) \%$ , shown in red). Whole pattern fits of selected data points are shown in Figure 5-7. The data points with mass ratios in the blue region in Figure 5-6A are artefacts linked to two areas in the upper blue flowers. These represent the higher  $\text{SiO}_2$  contents that were detected because of overlap of the quartz reflections (101) and (10 $\bar{1}$ ) with those of lead tin yellow (121) used in the green leaves on the front side (see Figure 2-17D for details) and are not indicative of a third type of azurite. The different types of azurite could originate from different ore mines, differences within a single geological site or to different grades of/other procedures for purification [32]. It is not clear why, in this manuscript, the artist chose to use two different types of azurite for the same purpose. The presences of two varieties of azurite could simply indicate the use of different batches of pigment or point to azurite added during a later restoration.

The above interpretation of these quantitative results assumes that both barite and quartz are present together with azurite in the blue features of the illuminated parchment. However, since pigment material from both the front and back side of the parchment contribute simultaneously to the collected diffraction patterns, it is possible that barite and or quartz are constituents of the gilded scrollwork on the opposite side of the parchment and not of the azurite blue details. The next section will illustrate that MA-XRPD allows for a spatial differentiation between materials applied on either the front or back side of the parchment.

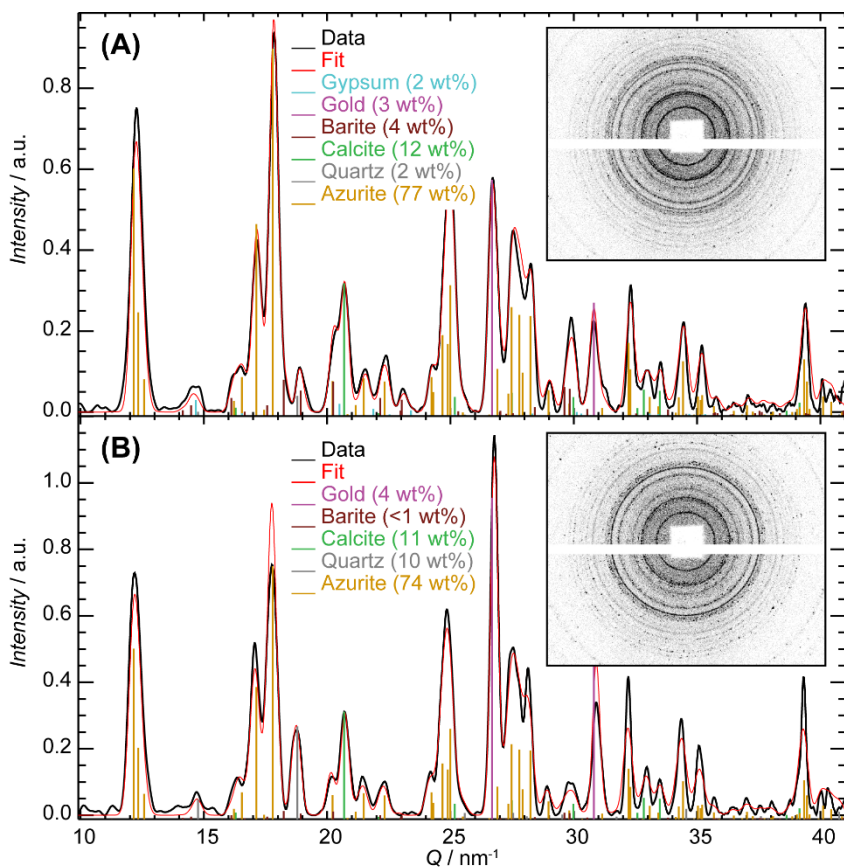


Figure 5-7. X-ray diffractograms and diffraction images of single data points located in the blue and golden scrollwork from the (A) green and (B) red regions in the azurite false color image (see Figure 5-6).

### 5.3.2. Depth-selective information

With conventional X-ray diffractometers a (paint) sample is ground and mixed to a fine homogenous powder before analysis. The powder is placed at the calibrated distance of the instrument so that the measured diffraction peak positions for all compounds correspond to the different interplanar distances present in the crystal structures. These measured peak positions can then be matched to those reported in crystal structure reference databases in order to identify the different compounds present in the sample.

For a multilayered paint system, at most one layer of the sample can be placed at the calibrated distance (typically the surface layer) at a given time. Crystalline material present within layers that are positioned in front or behind this optimal measurement position will exhibit a shift in their measured diffraction peak positions compared with those reported in literature. In Figure 5-8A it can be seen that for a paint sample consisting of a set of perfectly flat layers, the strata positioned closer to the detector than the calibrated distance ( $z$ ) will show a peak shift, resulting in smaller  $Q$  values (for the substrate,  $Q_s$ , and pigment,  $Q_p$ ) compared to the reported peak positions (for the substrate,  $Q_{sref}$ , and pigment,  $Q_{pref}$ ). For signals at higher  $2\theta$  angles (or  $Q$  values), up to  $45^\circ 2\theta$ , the same displacement will result in a larger peak shift (see Figure 5-11A and C). For overlapping layers of the same pigment ( $Q_{p2}$ ) either an intermediate shift and a broader diffraction peak or two separate peaks will be obtained depending on the distance between the two layers and the angular resolution of the instrument. The position of the substrate signal will stay unchanged between different points ( $Q_s$ ). If the different crystalline compounds are known, the shift between measured and reference peak position can be exploited to obtain stratigraphic information [25]. In the whole pattern fitting procedure this information is contained within the

displacement parameter (i.e. the distance of the center of mass of each compound to the detector) [23,24].

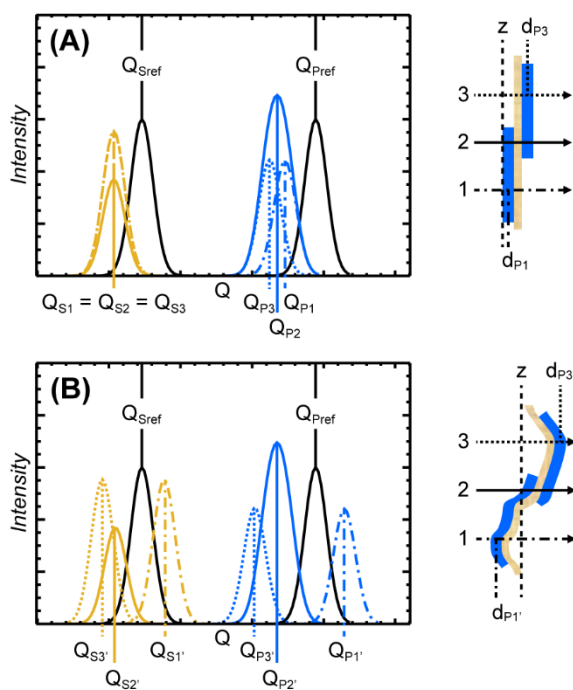


Figure 5-8. Shift of the diffraction peaks caused by displacement of the blue pigment layer (P, blue) and the substrate (S, beige) to the calibrated distance to the detector ( $z$ ) at different points (1-3) for (A) a perfect flat sample and (B) a sample showing strong curvature. The average distance of the blue layers to the detector in position 1 and 3 are given by respectively  $d_{P1}$  and  $d_{P3}$  for the flat sample and  $d_{P1'}$  and  $d_{P3'}$  for the sample with curvature. The arrows indicate the direction of the primary X-ray beam. The black signals correspond to the diffraction peak positions from reference databases.

For real objects, sample curvature, e.g. due to the bent surface of painted wooden panels or due to the presence of folds and wrinkles in a manuscript folio, will also contribute to the peak shift. In Figure 5-8B the shift of the diffraction signals not only depends on the stratigraphy of the layer structure but also on the sample

displacement (e.g.  $d_{PI}$  vs  $d_{PI'}$ ). In this case the shift in peak positions for  $Q_{PI'}$  and  $Q_{P3'}$  becomes larger or smaller depending on the curvature of the sample. A peak shift for the substrate layer is also observed, because the displacement with the calibrated distance is no longer constant between the different points ( $Q_S$ ). For single point measurements, sample curvature is not an issue as the sample can be moved to the same calibrated distance between exposures, but in a mapping experiment it is not (always) possible to continuously reposition the sample (or the instrument) at each measurement point. Therefore in order to extract information about the layer stratigraphy with MA-XRPD the sample curvature needs to be taken into account.

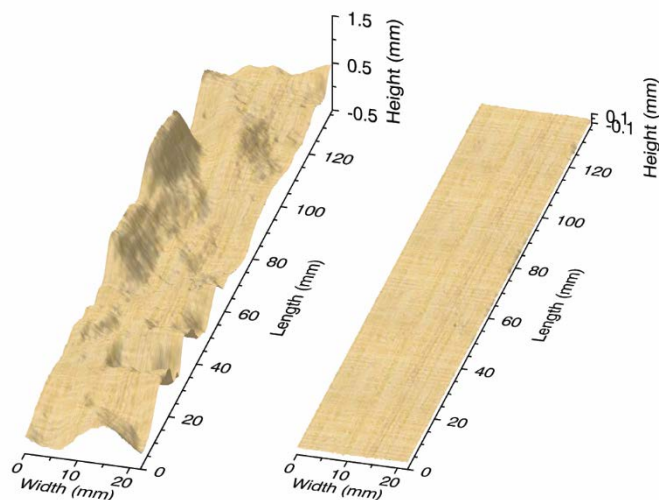


Figure 5-9. 3D visualization of the displacement parameter of calcite present in the parchment before (left) and after (right) curvature correction. The height-scale has been magnified by a factor 10 to improve readability.

Indeed, when looking at the displacement parameter for calcite the curvature of the illuminated parchment is clearly visible (see Figure 5-9 left). Since chalk is present inside the parchment substrate as it was used during its preparation, it is

an ideal marker to visualize its curvature. In each pixel of the imaging experiment the calcite displacement parameter ( $d$ ) can be used to correct the recorded peak positions ( $2\theta_m$ ) of all compounds. The corrected peak positions ( $2\theta_c$ ) for an area detector in transmission mode placed perpendicular to the primary X-ray beam at a calibrated sample-detector distance ( $z$ ) are given by Eq. 5-1

$$2\theta_c = \text{atan}(z \cdot \tan(2\theta_m)/(z + d)) \quad \text{Eq. 5-1}$$

with  $d < 0$  for compounds positioned closer to the detector.

After applying the curvature correction to all collected diffractograms and repeating the whole pattern fitting procedure on the corrected data set, it can be seen that a uniform distribution for the displacement parameter of calcite is obtained (Figure 5-9 right). All curvature has therefore been removed, corresponding to a virtual flattening of the manuscript in the scanned area.

Figure 5-10 shows the distributions of the displacement parameters for azurite, gold, barite and quartz after curvature correction. An intensity threshold was employed to remove data points from the imaging experiment in which the respective compounds were not present. The distinction between azurite and gold present in the scrollwork on either the front or back side can easily be made based on their displacement histograms (Figure 5-10F and G). The false color images, with red indicating pigments on the *recto* side of the manuscript (further from the detector) and green on the *verso* side, show the artistic interplay of the two pigments: areas of the scrollwork that have been painted with azurite on the front side are gilded on the back side and vice versa (Figure 5-10A and B). Confocal XRF analyses previously conducted on the illuminated parchment have shown that the gold layer is very thin ( $< 1 \mu\text{m}$ ) [33] so that the average thickness of the parchment can be estimated from the gold histograms and is about  $120 \mu\text{m}$ . Indeed, only the parchment separates the gilding on the *recto* and *verso* sides.

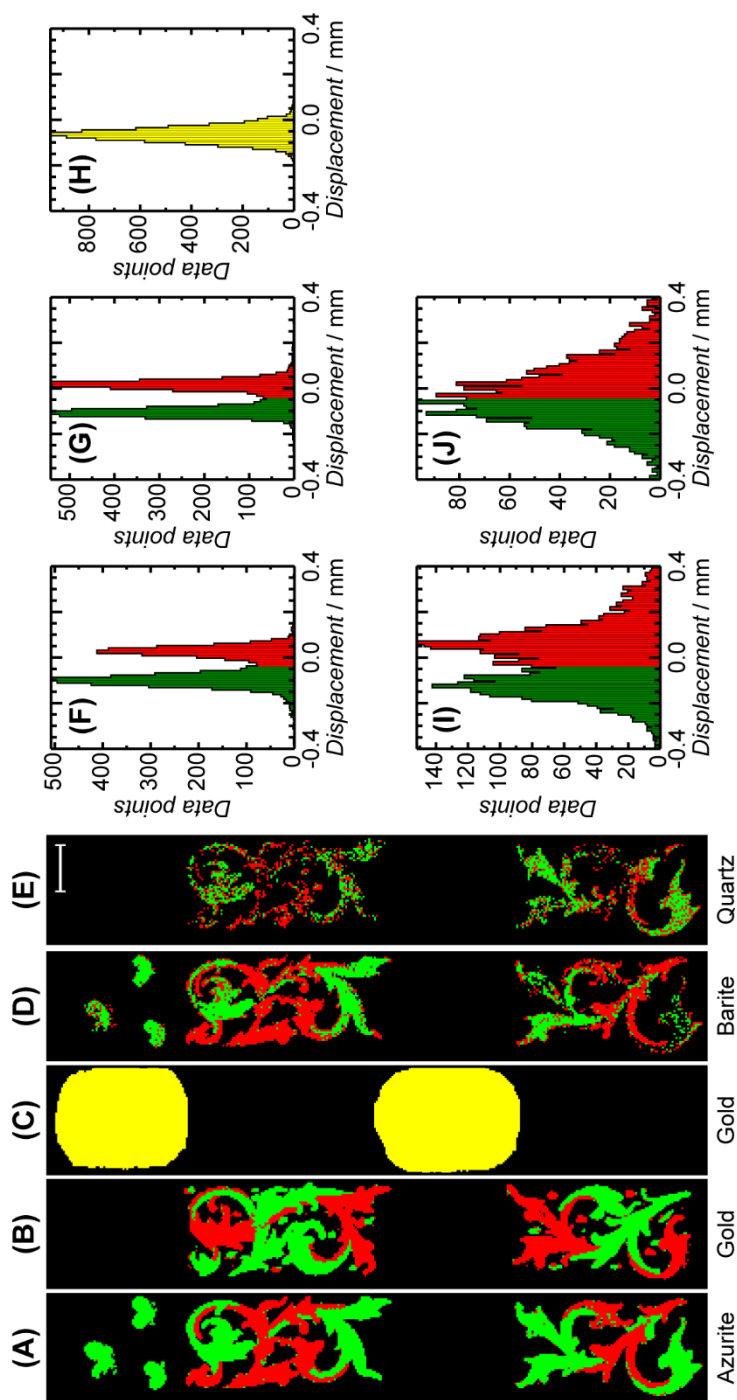


Figure 5-10. False color images of the (A) azurite, (B) gold used in the scrollwork, (C) gold used in the cartouches, (D) barite and (E) quartz distributions (scale bar = 10 mm). The histograms of the displacement parameters after curvature correction for (F) azurite, (G) gold in the scrollwork and (H) gold in the cartouches, (I) barite and (J) quartz show the color schemes that were used. A threshold based on the scaling parameter for each compound was employed to remove data points in which the compounds were not detected.

Unsurprisingly, barite features a similar depth distribution than azurite, showing it to be present on the front and back side in the same regions (Figure 5-10D). However, the low intensity of the barite XRPD peaks results in a large uncertainty on the modelled position of the diffraction signals, resulting in two broad distributions in the displacement histogram (Figure 5-10I). Even though for the quartz impurity the large spread in displacement values yields only one apparent layer in the histogram, a noisy image of its spatial distribution in the two different blue layers can still be extracted (Figure 5-10E and J).

While in the cartouches the gilding has been applied on both sides of the parchment, a unimodal distribution is visible in the corresponding displacement histogram (Figure 5-10C and H). The two gold layers are separated only by the parchment, with a thickness of 120  $\mu\text{m}$ . Rather than appearing as two separate contributions, the diffraction signals for gold originating from the front and back side appear as single combined peaks in the diffraction data. Indeed, when layers of the same pigment are applied on top of each other, the angular resolution of the MA-XRF/MA-XRPD instrument is insufficient to separate the diffraction signals coming from the individual layers unless a thicker intermediate layer (or sequence of layers) is present (as illustrated before in Figure 5-8). The minimal thickness of the intermediate layer to obtain a separation of the two pigment layers equal to their FWHM value is around 700  $\mu\text{m}$  (see Figure 5-11D) for the used instrument (configuration 9). Our experience has shown that not only the angular resolution, but also a higher primary energy or a smaller sample-detector distance (Figure 5-11A and B) can strongly improve the depth-selectivity.



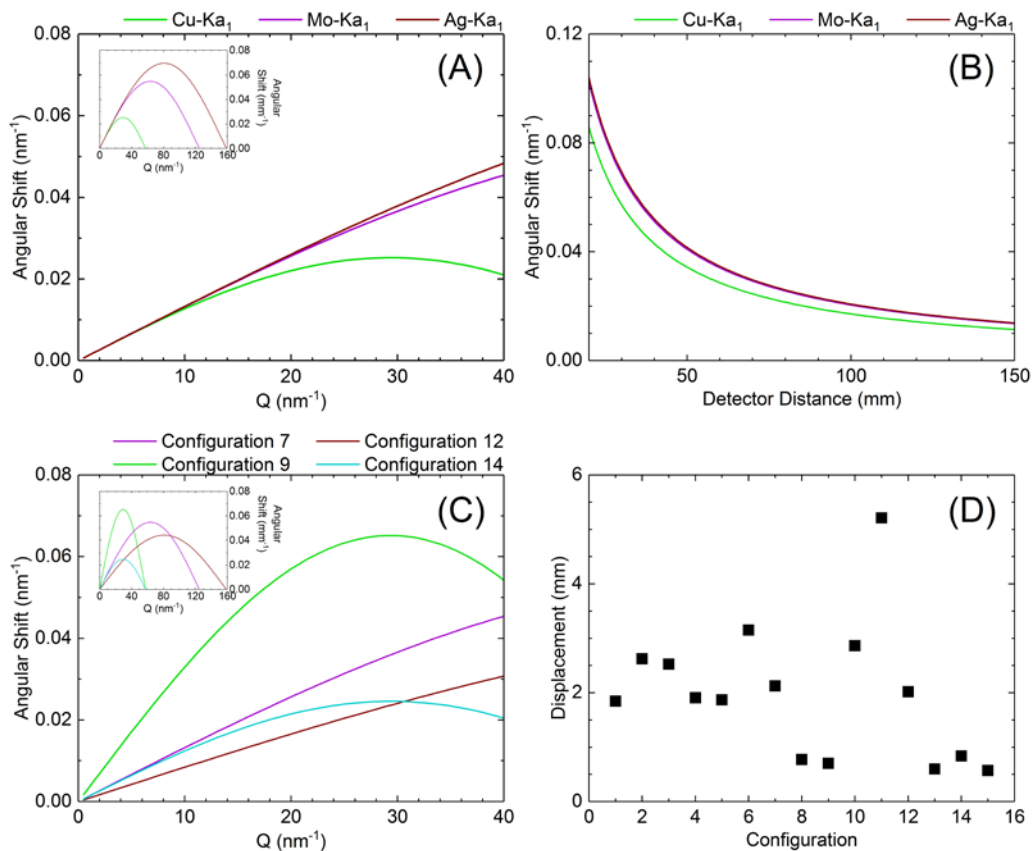


Figure 5-11. (A) Angular shift in function of the momentum transfer  $Q$  calculated for different primary energies ( $d = 100 \mu\text{m}$ ;  $z = 75 \text{ mm}$ ). The inset covers the entire  $Q$ -range for the different energies up to  $90^\circ 2\theta$ . (B) Angular shift of the LaB $_6$  (110) reflection in function of the sample-detector distance ( $z$ ) calculated for different energies ( $d = 100 \mu\text{m}$ ;  $Q = 21.38 \text{ nm}^{-1}$ ). (C) Angular shift in function of the momentum transfer  $Q$  calculated for different configurations ( $d = 100 \mu\text{m}$ ). The inset covers the entire  $Q$ -range for the different configurations up to  $90^\circ 2\theta$ . (D) The displacement resulting from a peak shift of the LaB $_6$  (110) reflection that equals the angular resolution of each configuration. A description of the different configurations is given in Table 2-4. The measurements in this chapter have been performed with configuration 9. All calculations were performed based on Eq. 5-1.

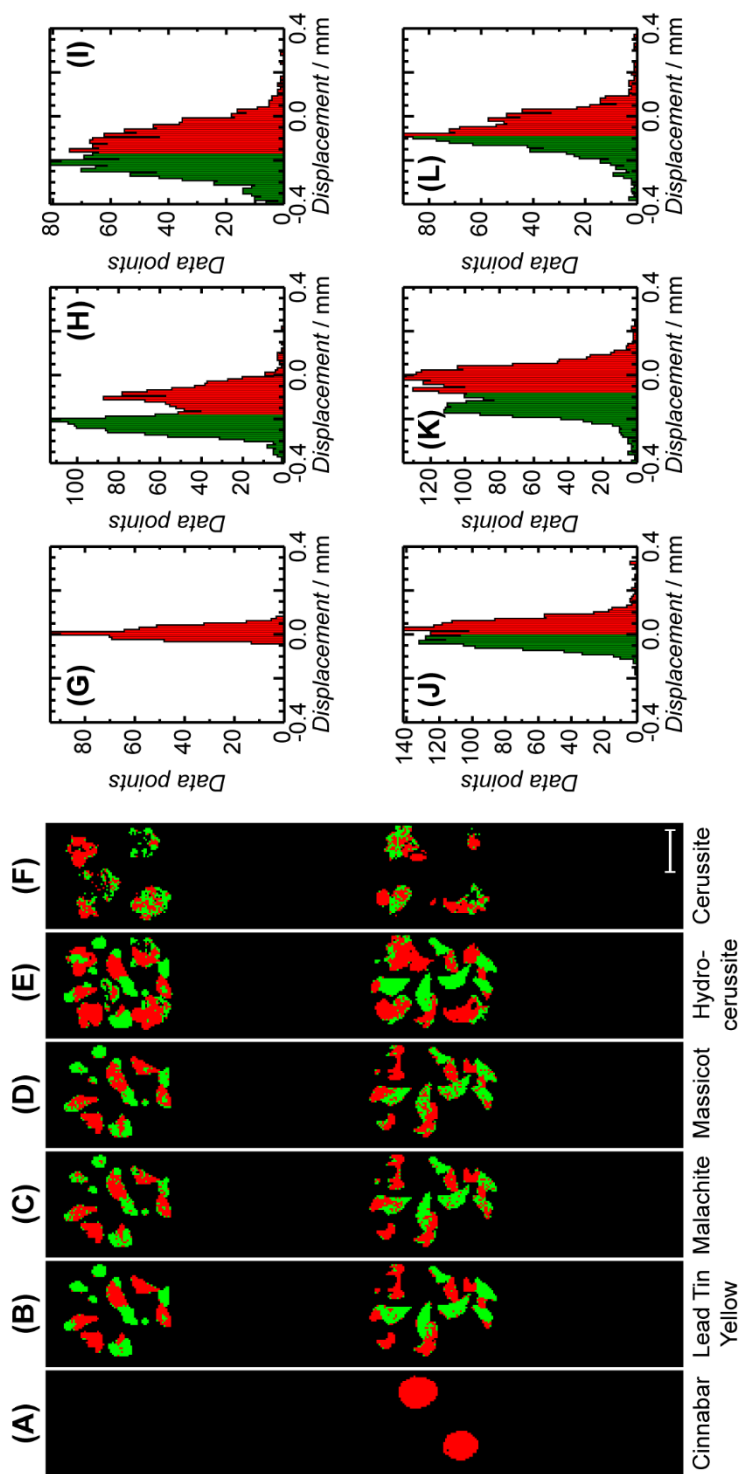


Figure 5-12. False color images of the (A) cinnabar, (B) lead tin yellow, (C) malachite, (D) massicot, (E) hydrocerussite and (F) cerussite distributions (scale bar = 10 mm). The histograms of the displacements for (G) cinnabar, (H) lead tin yellow, (I) malachite, (J) massicot, (K) hydrocerussite and (L) cerussite show the color schemes that were used. A threshold based on the scaling parameter was employed to remove data points in which the compounds are not present.

Although a separation can be made between the front and back side of the parchment, it is noteworthy that the absolute displacements for the different compounds are sometimes misleading. Indeed, the average displacement of lead tin yellow present on the front side of the parchment would place it together with azurite on the back side, respectively  $d_{\text{leadtinyellow,recto}} = -0.10$  mm and  $d_{\text{azurite,verso}} = -0.10$  mm (Figure 5-12H and Figure 5-10F). A similar displacement was found for malachite (Figure 5-12I).

Unfortunately, not only the displacement of the pigments influences the position of the measured diffraction signals, either because of stratigraphy or curvature, but also a difference between their actual unit cell dimensions compared to those reported in reference databases results in a shift in peak position. These variations in unit cell can be caused by isomorphic crystal structures. For example, the substitution of calcium with magnesium in the calcite crystal lattice may cause a reduction in the unit cell dimensions and consequently shifts the positions of the diffraction peaks of calcite to larger angles. Similarly small amounts of zinc can be incorporated in the crystal structure of the mineral malachite which alters the unit cell dimensions of the malachite lattice [34]. The origin of the shift in the synthetic pigment, lead tin yellow type I, remains unclear. The ability to determine absolute displacements for different compounds in a layered sample will therefore depend on how well the actual unit cell dimensions of the materials inside the object are known and will prove quite a challenge for the noninvasive analysis of real objects. Nonetheless the relative position between two or more layers containing the same pigment can be extracted, even when the unit cell dimensions are not accurately known.

For the pigments used for the vegetal and floral decorations throughout the cartouches a similar separation between the *recto* and *verso* sides could be made. However broad and overlapping histogram distributions, originating from low

intensity diffraction signals and overlapping layers of the same pigment, are more often present (Figure 5-12).

## 5.4. CONCLUSIONS

Combined MA-XRF/MA-XRPD is a powerful noninvasive technique that not only allows for the identification and visualization of highly-specific pigment distributions, but it can also extract quantitative information about the composition of pigments used throughout the work of art. In this chapter it has been shown that visualizing these phase fractions at the macroscale can help to differentiate even subtle differences in composition. These different compositions are often linked to various pigment qualities and their identification is a first step to understanding if certain pigment types were generally favored for the same purpose by a specific artist or period in time. MA-XRPD could prove particularly useful for clarifying the different compositions of lead white, a pigment that has been extensively used until the 19<sup>th</sup> century. However care should be taken in the interpretation of these results since averaged compositions will be obtained when multiple lead white layers are stacked on top of each other (e.g. lead white present in the ground and pictorial layers) because of the transmission geometry of the instrument. Quantification of the barite and quartz impurities within the azurite pigment revealed that two different azurite types (barite-rich and azurite-rich) were used on the illuminated parchment. Linking this information to the spatial distribution images showed distinct areas in which these two types were used.

In a second part of this chapter, the displacement parameter was used to extract limited information about the layer stratigraphy. It was possible to separate the same pigment applied on the front side of the parchment from the back side based on the collected diffraction data. However it was not possible to separate overlapping layers of the same pigment with the current instrument because of the thin separation layer (around 120  $\mu\text{m}$ ). Increasing the path length between the overlapping layers by positioning the sample under a smaller incident angle

(< 90 degrees) or in reflection geometry will increase the diffraction peak shift and reduce this limitation.

Two obstacles hamper the stratigraphic analysis: sample curvature and variations in unit cell dimensions. In this chapter, the former was corrected using calcite as a marker for the parchment roughness as it was present throughout the entire imaged area. The selected marker should ideally not be present within the paint layers themselves. Alternatively position sensitive devices can be used to measure and correct for sample displacement (e.g. laser sensor) before or after data collection. Furthermore, curvature correction simplifies data interpretation, as the shift in the position of the measured diffraction signals between individual points in the mapping experiment is greatly reduced. During whole pattern fitting this allows for more strict constraints on the displacement parameter so that erroneous contributions to compound-specific distribution images due to peak overlap can be minimized. Variations between the unit cell dimensions of the reference crystal structures and those of the actual materials present inside the object form the second obstacle. A systematic study of possible crystal structure variations for each pigment or a complementary analysis of cross-sections, when available, will result in more accurate depth information.

Next to identification of pigments, quantification of pigment compositions and delivering stratigraphic information of paint layers, also information about the texture and orientation, microstructure (crystallite and grain size) and/or isomorphs of pigments can provide valuable information. The ability of MA-XRPD to make some of this information available in a noninvasive manner and on a macroscopic scale holds a promising future for cultural heritage research.

## **ACKNOWLEDGMENTS**

The authors thank Incoatec GmbH for giving us the opportunity to test the I $\mu$ S-Cu X-ray source. We acknowledge financial support from BELSPO (Brussels) S2-ART, the NWO (The Hague) Science4Arts ‘ReVisRembrandt’ project and GOA Project Solarpaint (University of Antwerp Research Council).

## REFERENCES

- [1] Janssens, K.; Dik, J.; Cotte, M.; Susini, J. *Acc. Chem. Res.* **2010**, *43*, 814-825.
- [2] Alfeld, M.; Broekaert, J. A. C. *Spectrochim. Acta, Part B* **2013**, *88*, 211-230.
- [3] Conti, C.; Colombo, C.; Realini, M.; Matousek, P. *J. Raman Spectrosc.* **2015**, *46*, 476-482.
- [4] Casadio, F.; Daher, C.; Bellot-Gurlet, L. *Top. Curr. Chem.* **2016**, *374*.
- [5] Botteon, A.; Conti, C.; Realini, M.; Colombo, C.; Matousek, P. *Anal. Chem.* **2017**, *89*, 792-798.
- [6] Artioli, G. *Rendiconti Lincei-Scienze Fisiche E Naturali* **2013**, *24*, S55-S62.
- [7] Janssens, K. In *Non-destructive microanalysis of cultural heritage materials*, Janssens, K.; Van Grieken, R., Eds.; Elsevier Science, 2004, p 828.
- [8] Aze, S.; Vallet, J. M.; Baronnet, A.; Grauby, O. *Eur. J. Mineral.* **2006**, *18*, 835-843.
- [9] Benedetti, D.; Alessandri, I.; Bergese, P.; Bontempi, E.; Colombi, P.; Garipoli, D.; Pedrazzani, R.; Zanola, P.; Depero, L. E. *Microchim. Acta* **2006**, *155*, 101-104.
- [10] Duran, A.; Perez-Rodriguez, J. L.; Jimenez de Haro, M. C. *Anal. Bioanal. Chem.* **2009**, *394*, 1671-1677.
- [11] Svarcova, S.; Koci, E.; Bezdicka, P.; Hradil, D.; Hradilova, J. *Anal. Bioanal. Chem.* **2010**, *398*, 1061-1076.
- [12] Janssens, K.; Van der Snickt, G.; Vanmeert, F.; Legrand, S.; Nuyts, G.; Alfeld, M.; Monico, L.; Anaf, W.; De Nolf, W.; Vermeulen, M.; Verbeeck, J.; De Wael, K. *Top. Curr. Chem.* **2016**, *374*.
- [13] Welcomme, E.; Walter, P.; Bleuet, P.; Hodeau, J. L.; Dooryhee, E.; Martinetto, P.; Menu, M. *Appl. Phys. A: Mater. Sci. Process.* **2007**, *89*, 825-832.
- [14] Gonzalez, V.; Calligaro, T.; Wallez, G.; Eveno, M.; Toussaint, K.; Menu, M. *Microchem. J.* **2016**, *125*, 43-49.



- [15] Stols-Witlox, M.; Megens, L.; Carlyle, L. In *The artist's process: technology and interpretation*, Eyb-Green, S.; Townsend, J. H.; Clarke, M.; Nadolny, J.; Kroustallis, S., Eds.; Archetype Publications: London, 2012, pp 112-129.
- [16] Gonzalez, V.; Wallez, G.; Calligaro, T.; Cotte, M.; De Nolf, W.; Eveno, M.; Ravaud, E.; Menu, M. *Anal. Chem.* **2017**, *89*, 13203-13211.
- [17] Brunetti, B.; Miliani, C.; Rosi, F.; Doherty, B.; Monico, L.; Romani, A.; Sgamellotti, A. *Top. Curr. Chem.* **2016**, *374*.
- [18] Nakai, I.; Abe, Y. *Appl. Phys. A: Mater. Sci. Process.* **2012**, *106*, 279-293.
- [19] Alfeld, M.; Janssens, K.; Dik, J.; de Nolf, W.; van der Snickt, G. *J. Anal. At. Spectrom.* **2011**, *26*, 899-909.
- [20] Legrand, S.; Alfeld, M.; Vanmeert, F.; De Nolf, W.; Janssens, K. *Analyst* **2014**, *139*, 2489-2498.
- [21] Delaney, J. K.; Zeibel, J. G.; Thoury, M.; Littleton, R.; Palmer, M.; Morales, K. M.; de la Rie, E. R.; Hoenigswald, A. *Appl. Spectrosc.* **2010**, *64*, 584-594.
- [22] Vanmeert, F.; De Nolf, W.; De Meyer, S.; Dik, J.; Janssens, K. *Anal. Chem.* **2018**, *90*, 6436-6444.
- [23] De Nolf, W. *Imaging of crystalline phase distributions by means of scanning and tomographic X-ray powder diffraction*. Ph. D., University of Antwerp, Antwerp, 2013.
- [24] De Nolf, W.; Vanmeert, F.; Janssens, K. *J. Appl. Crystallogr.* **2014**, *47*, 1107-1117.
- [25] Chiari, G.; Sarrazin, P.; Heginbotham, A. *Appl. Phys. A: Mater. Sci. Process.* **2016**, *122*.
- [26] Gavarri, J. R.; Vigouroux, J. P.; Calvarin, G.; Hewat, A. W. *J. Solid State Chem.* **1981**, *36*, 81-90.
- [27] Downs, R. T.; Hall-Wallace, M. *Am. Mineral.* **2003**, *88*, 247-250.
- [28] Eastaugh, N.; Valentine, W.; Chaplin, T.; Siddall, R. *Pigment Compendium - A dictionary and optical microscopy of historical pigments*; Butterworth-Heinemann, 2008, p 960.

- [29] Stols-Witlox, M. In *Studying Old Master Paintings: Technology and Practice*, Spring, M., Ed.; Archetype Publications: London, 2011, pp 284-294.
- [30] Aru, M.; Burgio, L.; Rumsey, M. S. *J. Raman Spectrosc.* **2014**, *45*, 1013-1018.
- [31] Edwards, H. G. M.; Farwell, D. W.; Perez, F. R.; Villar, S. J. *Appl. Spectrosc.* **1999**, *53*, 1436-1439.
- [32] Smieska, L. M.; Mullett, R.; Ferri, L.; Woll, A. R. *Appl. Phys. A* **2017**, *123*, 484.
- [33] Lachmann, T.; van der Snickt, G.; Haschke, M.; Mantouvalou, I. *J. Anal. At. Spectrom.* **2016**, *31*, 1989-1997.
- [34] Behrens, M.; Girgsdies, F. *Z. Anorg. Allg. Chem.* **2010**, *636*, 919-927.

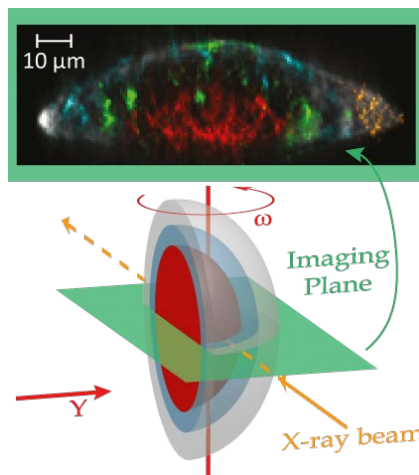


---

# Chapter 6 – Tomographic SR- $\mu$ -XRPD Imaging

---

Red lead, a semiconductor pigment used by artists since Antiquity, is known to undergo several discoloration phenomena. These transformations are either described as darkening of the pigment caused by the formation of plattnerite ( $\beta$ - $\text{PbO}_2$ ) or galena ( $\text{PbS}$ ), or as whitening by which red lead is converted into anglesite ( $\text{PbSO}_4$ ) or hydrocerussite ( $2\text{PbCO}_3 \cdot \text{Pb}(\text{OH})_2$ ) and cerussite ( $\text{PbCO}_3$ ). Tomographic SR- $\mu$ -XRPD imaging, a powerful analytical method that allows visualization of the internal distribution of different crystalline compounds in complex samples, was used to investigate a microscopic paint sample from ‘Wheat stack under a cloudy sky’ by Van Gogh. The high chemical and spatial specificity of this technique could be used to further elucidate the degradation mechanism behind the whitening of red lead.



This chapter is a modified version of a published paper: Reprinted with permission from **Vanmeert, F.**; Van der Snickt, G.; Janssens, K. “Plumbonacrite identified by X-ray powder diffraction tomography as a missing link during degradation of red lead in a Van Gogh painting” In: *Angew. Chem.-Int. Edit.* **2015**, 54 (12), 3607-3610. DOI: 10.1002/anie.201411691. Copyright 2015 John Wiley and Sons.

## 6.1. INTRODUCTION

X-ray powder diffraction (XRPD) mapping can be used to identify, visualize and to a certain extent quantify the different crystalline components that are present in complex heterogeneous paint systems [1]. Depending on the size of the X-ray probe it is possible to visualize crystalline-phase specific features on the macroscopic scale (as illustrated in previous chapters) or on the (sub)microscopic scale (discussed in the current chapter). For the latter, X-ray (sub)microbeams are available at high brilliance state-of-the-art synchrotron radiation facilities through the use of micro- and nanofocusing X-ray optics (e.g., capillary optics, Fresnel zone plates, Kirkpatrick-Baez mirrors, compound refractive lenses). In combination with motorized sample stages and highly efficient and fast area detectors, mapping experiments can be performed similar to the instruments described in the previous chapters.

In the field of cultural heritage the first X-ray powder diffraction mapping experiment was described by Dooryhée, et al. [1]. In the past 10 years, combined microscopic X-ray fluorescence and X-ray powder diffraction ( $\mu$ -XRF/ $\mu$ -XRPD) mapping experiments performed on samples extracted from works of art have been used for e.g., the study of ceramics from the Roman Period [2,3], the identification of various pigments and artist materials [4], as well as their degradation products (e.g., discoloration of cadmium yellow [5-7], and darkening of vermilion [8-10] and chrome yellow [11]), and even the imaging of a complete painting [12]. However, an intrinsic limitation of two-dimensional (2D) mapping remains the loss of depth information as projection images are obtained (see Figure 6-1A). Therefore, in order to investigate the stratigraphy of a paint system, typically a cross-section of a paint sample needs to be prepared, consuming to a lesser or greater extent part of the (often unique or very rare) sample. With  $\mu$ -XRPD tomography, the inner distribution of the crystalline components present

in such samples can be visualized without physically cross-sectioning the material under investigation [13,14] (see Figure 6-1B). Although the capabilities of this technique have been demonstrated on various complex materials [15], it has been scarcely used in the cultural heritage field [16].

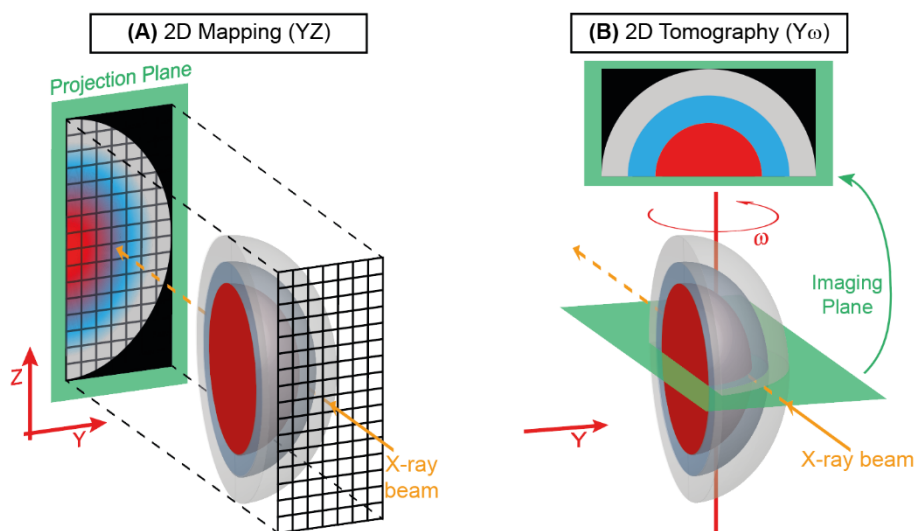


Figure 6-1. Schematic illustration of the 2D mapping (A) and tomography principle (B) on a spherical sample using a pencil beam. The corresponding imaging planes are shown in green.

In comparison to computed absorption tomography (CT) which shows the three-dimensional (3D) X-ray attenuation density distribution of the sample, the reconstructed virtual slice obtained by combined X-ray fluorescence and X-ray diffraction microbeam ( $\mu$ -XRF/ $\mu$ -XRPD) tomography contains both elemental and phase-specific information. For the latter, the measured volume is usually limited to one or a small stack of 2D slices because of the time-demanding point-by-point sequential scanning procedure.

In this chapter, the combined  $\mu$ -XRF/ $\mu$ -XRPD imaging experiment of a minute sample obtained from the painting *Wheat stack under a cloudy sky* by Vincent van

Gogh (October 1889, oil on canvas, Kröller-Müller Museum, NL) is discussed. On the one hand the described results highlight the capabilities of  $\mu$ -XRPD computed tomography on microscopic paint samples and on the other hand help to further elucidate the degradation mechanism of red lead.

## 6.2. EXPERIMENTAL SECTION AND METHODS

### 6.2.1. Experimental setup at beamline P06

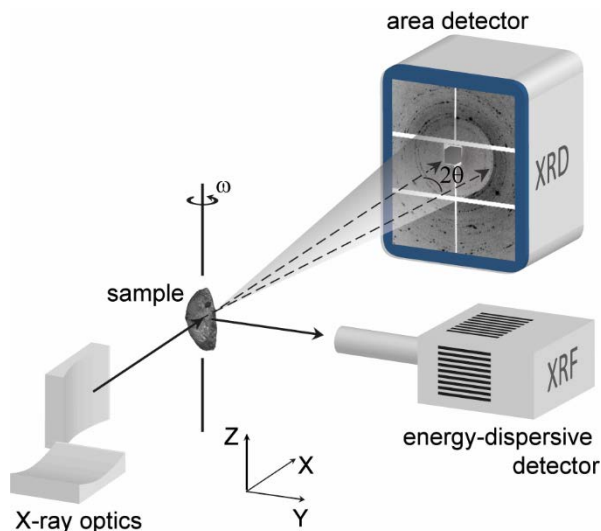


Figure 6-2. Schematic illustration of the experimental setup used for the 2D  $\mu$ -XRF/ $\mu$ -XRPD mapping (YZ) and tomography ( $Y\omega$ ) experiment at beam line P06 (PETRA III, DESY, DE).

The combined  $\mu$ -XRF/ $\mu$ -XRPD imaging experiments were performed at the microprobe station of the P06 Hard X-ray Micro/Nano-Probe beam line (PETRA III, DESY, Germany) [17]. A photon energy of 21 keV was selected by means of a Si(III) double crystal monochromator. The beam was focused to  $0.5 \times 0.5 \mu\text{m}$  (hor.  $\times$  vert.) employing a Kirkpatrick-Baez mirror optic. A Keyence optical microscope equipped with a perforated mirror allowed for precise positioning of the sample. For the tomographic experiments, the sample was placed in the center of rotation using two piezo stages mounted on top of the rotation stage. Fluorescence radiation was recorded by a Vortex-EM silicon drift detector (SII, Northridge, CA, US) placed perpendicular to the incident X-ray beam. Simultaneously, diffraction signals were recorded in transmission geometry



using a PILATUS 300K area detector (Dectris Ltd., CH) at a distance of approximately 15 cm behind the sample. Initial calibration of the diffraction setup was performed using a LaB<sub>6</sub> reference sample. A schematic representation of the experimental setup is given in Figure 6-2. The sample was placed on a small piece of transparent adhesive tape, which was fixed on a brass cylinder. This method proved stable against movements on the microscopic scale, showing no visual blurring of the image at the desired spatial resolution of the experiment.

### **6.2.2. X-ray diffraction tomography**

A virtual cross-section of the sample was obtained by repeatedly scanning one line on the sample point by point with a step size of 1  $\mu\text{m}$  using a pencil beam. In each point the sample was irradiated for 1 second during which both a diffraction image and a fluorescence spectrum were acquired. After each completed line, the sample was rotated over a small angular interval ( $2^\circ$ ). In this way, a 2D map is obtained with one translation ( $Y$ ) and one rotation ( $\omega$ ) dimension, called a sinogram. The resulting compound-specific sinograms were used to reconstruct the virtual cross-section of the paint sample using the maximum-likelihood expectation-maximization (MLEM) algorithm [18]. The statistical reconstruction algorithm MLEM was chosen over analytical reconstruction methods such as filtered back-projection (FBP) to suppress reconstruction artifacts originating from inconsistencies in the Radon space. These inconsistencies can be introduced by the experiment, e.g., due to absorption effects (XRF), “grainy” powder diffraction patterns (XRD) and/or counting noise (XRF/XRD).

### **6.2.3. X-ray absorption tomography**

The CT measurements were performed on an Xradia MicroXCT-400 instrument equipped with a Hamamatsu 150 kV X-ray source and a 2 K  $\times$  2 K Andor CCD camera. In addition to the geometric magnification, it also includes a set of

scintillator-coated objective lenses with an optical magnification of 0.5X, 4X, 10X, 20X and 40X. The microscopic paint sample was measured employing a 40 kV acceleration voltage and a 250  $\mu$ A current. No filter material was used. The CT data was recorded with 0.09° rotational step over a total angular range of 182 degrees. Each angular step was exposed for 35 sec. Reconstructions were performed using an algorithm based on cone beam filtered back projection, including ring artefact and beam hardening corrections. The latter is required since a polychromatic primary beam was used. The voxel size was  $0.5 \times 0.5 \times 0.5 \mu\text{m}$ .

#### **6.2.4. $\mu$ -XRF/ $\mu$ -XRPD data processing**

The software package PyMCA was used for spectral fitting of the fluorescence data [19], while whole pattern fitting of the diffraction data as well as the  $\mu$ -XRF and  $\mu$ -XRPD computed tomography reconstructions were performed using XRDUA [14]. This software package provides several methods for obtaining crystalline-specific distributions from a large number of diffraction patterns typically obtained in  $\mu$ -XRPD imaging experiments [16].

#### **6.2.5. *Wheat stack under a cloud sky*, Van Gogh**

The microscopic paint sample was obtained from *Wheat stack under a cloudy sky* by Vincent van Gogh (October 1889, F563, oil on canvas, Kröller-Müller Museum, NL) during the removal of the yellowed varnish. The sample consists of a severed pustular mass revealing a bright orange-red core (about 100  $\mu\text{m}$  in diameter) surrounded by a light blue tinted layer and a gray outer layer that partially covers the pustular mass (Figure 6-3). A faint impression of the red core remains visible through the thin outer layer.

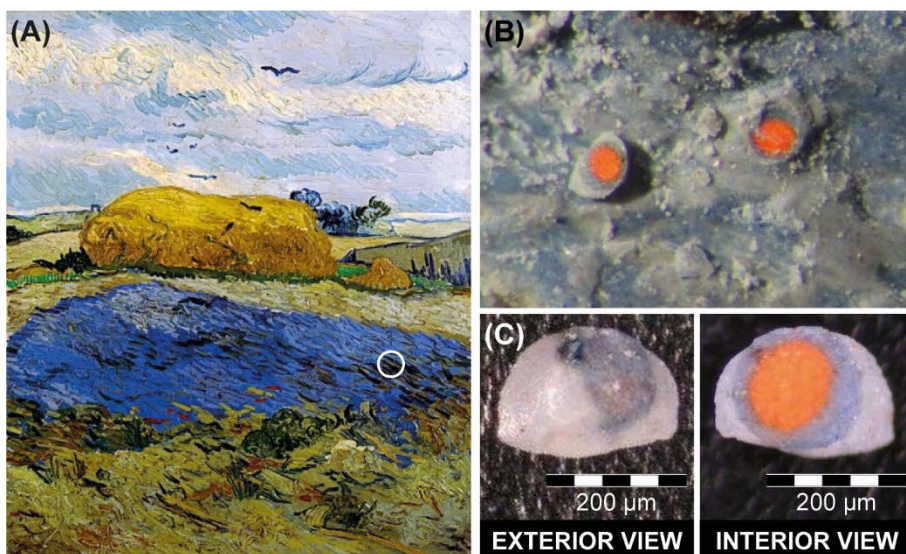


Figure 6-3. (A) Photograph of *Wheat stack under a cloudy sky* by Van Gogh (October 1889, F563, oil on canvas, Kröller-Müller Museum, NL). The sample area is indicated by the white circle; (B) Detail of the severed pustular mass on the painting surface showing the exposed bright red core; (C) Detail of the paint sample.

### 6.3. RESULTS AND DISCUSSION

The X-ray radiograph (XRR) obtained from the CT dataset clearly shows two regions with different particle size as shown in Figure 6-4. The outer layer of the pustular mass consists of finely grained particles, rich in both Zn and Pb (Zn-K and Pb-L  $\mu$ -XRF in Figure 6-4), that were applied onto the original blue paint layer which is made up of coarse grains. The compound-specific distribution maps ( $\mu$ -XRPD distributions in Figure 6-4) show that this gray layer contains a mixture of the pigments zinc white (zincite, ZnO) and lead white (hydrocerussite,  $2\text{PbCO}_3 \cdot \text{Pb}(\text{OH})_2$ ). Although both white pigments were part of Van Gogh's palette [20], this outer layer was not originally present but was added later, probably during retouching. While the lead white used in this outer layer consists only of basic lead carbonate, a different lead white composition is found in the light blue layer underneath that contains both neutral (cerussite,  $\text{PbCO}_3$ ) and basic lead carbonate (hydrocerussite). The blue color of this layer could originate from cobalt blue, a pigment frequently used by Van Gogh, as a significant Co XRF signal is observed. In the bright red core of the pustule, a third lead-containing pigment identified as red lead is present.

Red lead, most commonly designated with the term minium, is a semiconductor pigment used since ancient times and is thought to be one of the first artificially prepared pigments [21]. Minium corresponds to the lead(II,IV) oxide mineral of composition  $\text{Pb}_3\text{O}_4$  and can often be found on artworks in association with lead monoxide, either litharge (tetragonal PbO) or massicot (orthorhombic PbO) [22]. Either polymorph could have been intentionally added to the red lead pigment or is a byproduct of the pigment manufacturing process (that may involve roasting of hydrocerussite or litharge) [23]. However, the diffraction data did not show any lead(II) oxides in the sample.

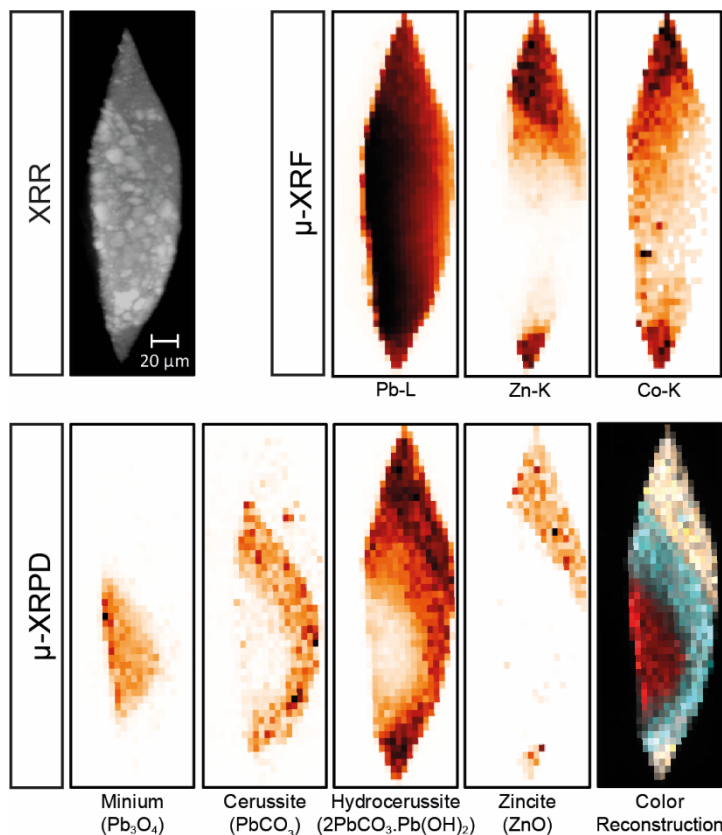


Figure 6-4. (Top) X-ray radiography (XRR) image calculated from the X-ray absorption tomography dataset. (Top row) Elemental and (bottom row) phase-specific 2D distribution images of the severed pustule. Map size:  $80 \times 255 \mu\text{m}$ ; Pixel size:  $4 \times 5 \mu\text{m}$ . Legend of the color reconstruction: minium (red), cerussite (blue), hydrocerussite (white) and zincite (orange)

The red lead pigment is known to be unstable with time. On the one hand, it is thought to play a role in the formation of lead soap protrusions where lead carbonate (basic and/or neutral form) and lead soaps are formed through the reaction of red lead with the fatty acids present in the oil medium [24]. On the other hand, orange, flake-like particles found in and around lead soap protrusions have been identified as minium [25,26], and are believed to have formed via

remineralization usually together with lead carbonate [27]. However, from the large grains shown to be present in the interior of the sample and the large amount of red lead present, it is most plausible that minium is the original material and not a degradation product as a result of protrusion formation. It is also known both from his letters and from the study of paint samples that Van Gogh used minium as a red pigment in his paintings from the Auvers-sur-Oise period [20]. MA-XRPD investigations (with configuration 12) on *Wheat stack under a cloudy sky* revealed reddish streaks of minium in the water puddle.

Next to being involved in protrusion formation, red lead can undergo severe discoloration [28]. The most frequently encountered color change is described as blackening or darkening of the pigment, caused by the formation of either galena (PbS) or plattnerite ( $\beta$ -PbO<sub>2</sub>). Although galena is more typically encountered in darkened areas on illuminated manuscripts [29], plattnerite is generally stated to be the main cause of red lead darkening through the oxidation of Pb<sub>3</sub>O<sub>4</sub>.

A second, less documented discoloration, visible as whitening or bleaching of the pigment has also been described [30]. In this case the alteration products are shown to be either lead carbonate (neutral and/or basic) or lead sulfate (PbSO<sub>4</sub>) resulting from the interaction with atmospheric CO<sub>2</sub> and SO<sub>2</sub>, which in humid conditions leads to a decrease in pH. However, CO<sub>2</sub> can also be generated *in situ* through a photochemical breakdown of organic dyes [31,32]. Both lead carbonates described to the whitening of the pigment are present in the blue covering layer, making it difficult to conclude that whitening of the red lead is taking place.

However, the tomographic reconstructions of the inner distribution of the crystalline phases revealed a “vacant space” between the minium core and the blue-tinted lead white layer (Figure 6-5). In fact a fourth lead-containing compound, plumbonacrite (3PbCO<sub>3</sub>.Pb(OH)<sub>2</sub>.PbO), is found to be present in the

sample (see Figure 6-6), which is largely situated in this “void”. To some extent an overlap between the lead white layer and plumbonacrite is visible.

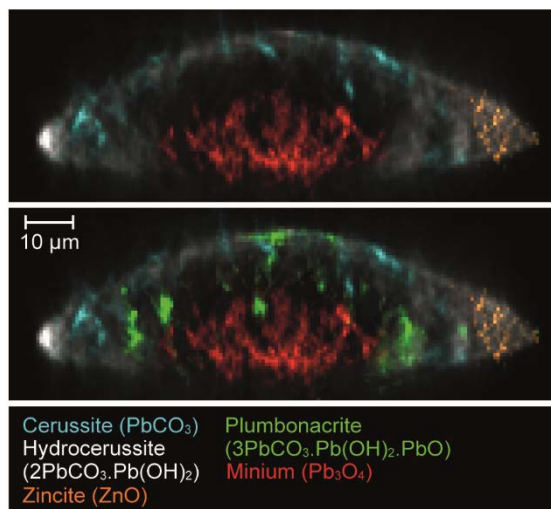


Figure 6-5. Color reconstructions of the inner crystalline distribution of the paint sample. Reconstructed map size:  $111 \times 43 \mu\text{m}$ ; Pixel size:  $1 \times 1 \mu\text{m}$ .

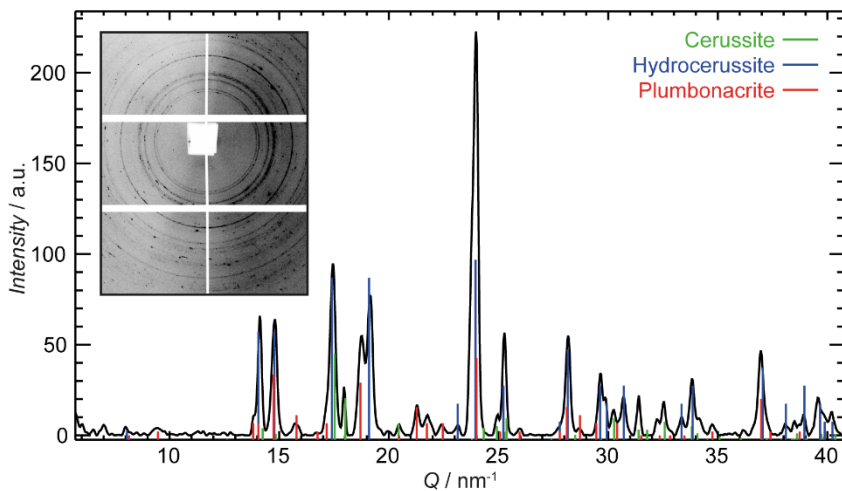


Figure 6-6. X-ray diffractogram showing the presence of the rare mineral plumbonacrite ( $3\text{PbCO}_3 \cdot \text{Pb}(\text{OH})_2 \cdot \text{PbO}$ ).

Plumbonacrite, a very rare lead carbonate mineral, can be formed in aqueous systems at ambient temperature and pressure and is metastable with respect to litharge ( $t$ -PbO) and hydrocerussite [33,34]. The name plumbonacrite can refer to either the naturally occurring lead carbonate mineral described by Heddle [35] or a synthetic compound. The crystal structure of synthetic plumbonacrite was first described by Olby [36], who proposed the formula  $6\text{PbCO}_3 \cdot 3\text{Pb(OH)}_2 \cdot \text{PbO}$ . This structure was later redetermined to be  $3\text{PbCO}_3 \cdot \text{Pb(OH)}_2 \cdot \text{PbO}$  [37]; however the formula given by Olby is still frequently being used in current literature.

Plumbonacrite has been commonly reported as a corrosion product, for example in artificial ageing studies of lead samples subjected to acidic environments [38,39], and on bronzes [40], as well as on naturally aged objects [41,42]. However, literature regarding the presence of plumbonacrite in paintings or painters materials is very scarce. Plumbonacrite, together with (hydro)cerussite, was identified as a degradation product formed from lead(II) oxides upon artificial ageing [43,44]. It is worth mentioning that plumbonacrite was made synthetically from the mid-20<sup>th</sup> century while trying to produce a lead white variant with a more uniform composition and is therefore present on several paintings of this period [45]. Before, it was, to our best knowledge, never detected on paintings, either as part of lead white mixtures or as a pure compound.

In our case, the presence of this carbonate-poor Pb-compound in between the red lead and the carbonate-rich lead white layer strongly suggests that plumbonacrite is present as an intermediate degradation product formed during the whitening of minium. Since PbO, a remnant of the red lead production process [28], is more reactive than  $\text{Pb}_3\text{O}_4$ , it may have initiated the degradation. Alternatively, minium itself can be photoactivated, leading to the reduction of  $\text{Pb}^{\text{IV}}$  to  $\text{Pb}^{\text{II}}$ . For the latter pathway, we propose an additional step in the photochemical reaction described by Zhou, et al. [31] (Figure 6-7).



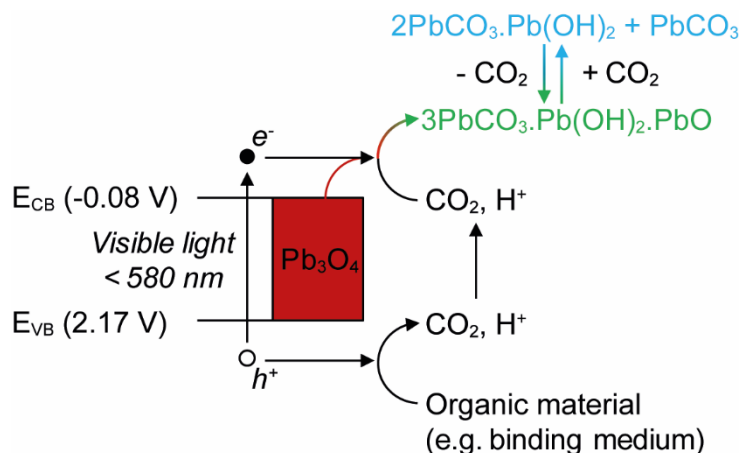
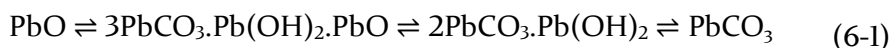


Figure 6-7. Proposed pathway for the photochemical degradation of  $Pb_3O_4$  under visible light irradiation. Conduction and valence band potentials, respectively  $E_{CB}$  and  $E_{VB}$ , are given relative to the normal hydrogen electrode (NHE) [31].

Electron hole pairs are formed between the valence (2.17 V) and conduction band (-0.08 V) of minium upon exposure to visible light ( $\lambda < 580 \text{ nm}$ ). The electrons generated in the conduction band can reduce  $Pb^{IV}$  present in minium to  $Pb^{II}$  which in turn reacts with  $CO_2$  to form one or more lead carbonate compounds [31,32]. The required  $CO_2$  can be formed *in situ* through the oxidative decarboxylation of free fatty acids present in e.g., the binding medium [24]. However the influence of atmospheric  $CO_2$  has also been proven to affect the whitening of red lead [30]. Here we propose an intermediate step in the fixation of  $CO_2$  where a gradual uptake of  $CO_2$  leads to the formation of plumbonacrite. Depending on the availability of  $CO_2$ , the initially formed plumbonacrite layer can take up more  $CO_2$  to form hydrocerussite and finally cerussite. Indeed, such a gradual uptake of  $CO_2$  by lead(II) oxide has been shown to exist [34].



Thus, our observations are fully consistent with the results obtained by Taylor and Lopata [34], who studied the solubility and stability of the PbO-CO<sub>2</sub>-H<sub>2</sub>O system and they complete the photoinduced degradation pathway of minium.

## 6.4. CONCLUSIONS

XRF/XRPD mapping and tomography at the (sub)microscopic scale are powerful analytical tools that allowed us to investigate the stratigraphy of a multi-layered microscopic paint sample from the canvas painting *Wheat stack under a cloudy sky* by Van Gogh and to extract some insights into the chemical reactivity of the pigment red lead. Although XRF revealed lead to be present in the entire sample, with  $\mu$ -XRPD imaging it was possible to identify and visualize four different lead-containing crystalline phases distributed over separate micrometric layers. The orange-red color of the inner core of the sample is attributed to the red lead pigment. Lead white, consisting of both hydrocerussite and cerussite was identified in the light blue layer, where a Co-containing pigment is responsible for the blue color. The grayish outer layer, applied in a later period as a retouch, contains a mixture of fine particles of zinc white and hydrocerussite. Through visualization of the inner crystalline distribution of the microscopic paint sample by  $\mu$ -XRPD tomography a very rare lead mineral, plumbonacrite, was found to be located in between the minium core and the hydrocerussite/cerussite layer.

To our best knowledge this is the first reported occurrence of plumbonacrite in a sample taken from a painting dating from before the mid-20<sup>th</sup> century. The presence of plumbonacrite encapsulated in between the lead(II,IV) oxide layer and the lead carbonate-rich layer strongly suggests that this compound is an intermediate product in the photochemical degradation pathway leading to the whitening of red lead. Additional work is required to verify experimentally that the plumbonacrite intermediate is formed according to the proposed degradation pathway and to elucidate the role of possible lead(II) oxide (either litharge or massicot) on the photochemical degradation of the more stable minium compound.

## **ACKNOWLEDGMENTS**

Luuk van der Loeff and Margje Leeuwestein (Kröller-Müller Museum, Otterlo) are gratefully acknowledged for providing the paint sample. We thank Dr. Jakub Jaroszewicz (Warsaw University of Technology) for performing the CT measurements. This research was carried out at the light source PETRA III at DESY, a member of the Helmholtz Association (HGF). We would like to thank Dr. Gerald Falkenberg and the members of his team for their assistance in using beam line P06.

## REFERENCES

- [1] Dooryh e, E.; Anne, M.; Bardi es, I.; Hodeau, J. L.; Martinetto, P.; Rondot, S.; Salomon, J.; Vaughan, G. B. M.; Walter, P. *Appl. Phys. A* **2005**, *81*, 663-667.
- [2] Sciau, P.; Goudeau, P.; Tamura, N.; Dooryhee, E. *Appl. Phys. A* **2006**, *83*, 219-224.
- [3] Leon, Y.; Sciau, P.; Goudeau, P.; Tamura, N.; Webb, S.; Mehta, A. *Appl. Phys. A* **2010**, *99*, 419-425.
- [4] Welcomme, E.; Walter, P.; Bleuet, P.; Hodeau, J. L.; Dooryhee, E.; Martinetto, P.; Menu, M. *Appl. Phys. A: Mater. Sci. Process.* **2007**, *89*, 825-832.
- [5] Van der Snickt, G.; Dik, J.; Cotte, M.; Janssens, K.; Jaroszewicz, J.; De Nolf, W.; Groenewegen, J.; Van der Loeff, L. *Anal. Chem.* **2009**, *81*, 2600-2610.
- [6] Van der Snickt, G.; Janssens, K.; Dik, J.; De Nolf, W.; Vanmeert, F.; Jaroszewicz, J.; Cotte, M.; Falkenberg, G.; Van der Loeff, L. *Anal. Chem.* **2012**, *84*, 10221-10228.
- [7] Pouyet, E.; Cotte, M.; Fayard, B.; Salom e, M.; Meirer, F.; Mehta, A.; Uffelmann, E. S.; Hull, A.; Vanmeert, F.; Kieffer, J.; Burghammer, M.; Janssens, K.; Sette, F.; Mass, J. *Appl. Phys. A* **2015**, 1-14.
- [8] Cotte, M.; Susini, J.; Sol e, V. A.; Taniguchi, Y.; Chillida, J.; Checroun, E.; Walter, P. *J. Anal. At. Spectrom.* **2008**, *23*, 820.
- [9] Radepont, M.; de Nolf, W.; Janssens, K.; Van der Snickt, G.; Coquinot, Y.; Klaassen, L.; Cotte, M. *J. Anal. At. Spectrom.* **2011**, *26*, 959.
- [10] Da Pieve, F.; Hogan, C.; Lamoen, D.; Verbeeck, J.; Vanmeert, F.; Radepont, M.; Cotte, M.; Janssens, K.; Gonze, X.; Van Tendeloo, G. *Phys. Rev. Lett.* **2013**, *111*, 208302.
- [11] Monico, L.; Janssens, K.; Hendriks, E.; Vanmeert, F.; Van der Snickt, G.; Cotte, M.; Falkenberg, G.; Brunetti, B. G.; Miliani, C. *Angew. Chem.-Int. Edit.* **2015**, *54*, 13923-13927.

- [12] De Nolf, W.; Dik, J.; Van der Snickt, G.; Wallert, A.; Janssens, K. *J. Anal. At. Spectrom.* **2011**, *26*, 910.
- [13] Bleuet, P.; Welcomme, E.; Dooryhee, E.; Susini, J.; Hodeau, J. L.; Walter, P. *Nat. Mater.* **2008**, *7*, 468-472.
- [14] De Nolf, W.; Janssens, K. *Surf. Interface Anal.* **2010**, *42*, 411-418.
- [15] Alvarez-Murga, M.; Bleuet, P.; Garbarino, G.; Salamat, A.; Mezouar, M.; Hodeau, J. L. *Phys. Rev. Lett.* **2012**, *109*.
- [16] De Nolf, W.; Vanmeert, F.; Janssens, K. *J. Appl. Crystallogr.* **2014**, *47*, 1107-1117.
- [17] Schroer, C. G.; Boye, P.; Feldkamp, J. M.; Patommel, J.; Samberg, D.; Schropp, A.; Schwab, A.; Stephan, S.; Falkenberg, G.; Wellenreuther, G.; Reimers, N. *Nuclear Instruments and Methods in Physics Research Section A: Accelerators, Spectrometers, Detectors and Associated Equipment* **2010**, *616*, 93-97.
- [18] Shepp, L. A.; Vardi, Y. *IEEE Transactions on Medical Imaging* **1982**, *MI-1*, 113-122.
- [19] Sole, V. A.; Papillon, E.; Cotte, M.; Walter, P.; Susini, J. *Spectrochim. Acta, Part B* **2007**, *62*, 63-68.
- [20] Geldof, M.; Megens, L.; Salvant, J. In *Van Gogh's studio practice*, Vellekoop, M.; Geldof, M.; Hendriks, E.; Jansen, L.; de Tagle, A., Eds.; Mercatorfonds, 2013, pp 238-255.
- [21] FitzHugh, E. W. In *Artists' Pigments: A Handbook of their history and Characteristics*, Feller, R. L., Ed.; Oxford University Press, 1985, pp 109-139.
- [22] Eastaugh, N.; Valentine, W.; Chaplin, T.; Siddall, R. *Pigment Compendium - A dictionary and optical microscopy of historical pigments*; Butterworth-Heinemann, 2008, p 960.
- [23] Aze, S.; Vallet, J. M.; Pomey, M.; Baronnet, A.; Grauby, O. *Eur. J. Mineral.* **2007**, *19*, 883-890.
- [24] Higgitt, C.; Spring, M.; Saunders, D. *Natl. Gallery Tech. Bull.* **2003**, *24*, 14.

- [25] Boon, J. J.; Van der Weerd, J.; Keune, K.; Noble, P.; Wadum, J. In *ICOM Committee for Conservation, 13th Triennial Meeting, Rio de Janeiro*; Maney - Heritage, 2002, pp 401-406.
- [26] van der Weerd, J.; Boon, J. J.; Geldof, M.; Heeren, R. M. A.; Noble, P. *Zeitschrift für Kunsttechnologie und Konservierung* **2002**, *16*, 36-51.
- [27] Keune, K.; Boon, J. J. *Stud. Conserv.* **2007**, *52*, 161-176.
- [28] Aze, S.; Vallet, J. M.; Detalle, V.; Grauby, O.; Baronnet, A. *Phase Transitions* **2008**, *81*, 145-154.
- [29] Miguel, C.; Claro, A.; Goncalves, A. P.; Muralha, V. S. F.; Melo, M. J. *J. Raman Spectrosc.* **2009**, *40*, 1966-1973.
- [30] Saunders, D.; Spring, M.; Higgitt, C. In *13th Triennial Meeting Rio De Janeiro Preprints*, 2002, pp 455-463.
- [31] Zhou, Y. G.; Lin, H. X.; Gu, Q.; Long, J. L.; Wang, X. X. *Rsc Advances* **2012**, *2*, 12624-12627.
- [32] Zhou, Y. G.; Long, J. L.; Gu, Q.; Lin, H. X.; Lin, H.; Wang, X. X. *Inorg. Chem.* **2012**, *51*, 12594-12596.
- [33] Haacke, D. F.; Williams, P. A. *J. Inorg. Nucl. Chem.* **1981**, *43*, 406-406.
- [34] Taylor, P.; Lopata, V. J. *Can. J. Chem.* **1984**, *62*, 395-402.
- [35] Heddle, M. F. *Mineral. Mag.* **1889**, *8*, 200-203.
- [36] Olby, J. K. *J. Inorg. Nucl. Chem.* **1966**, *28*, 2507-&.
- [37] Krivovichev, S. V.; Burns, P. C. *Mineral. Mag.* **2000**, *64*, 1069-1075.
- [38] Tetreault, J.; Sirois, J.; Stamatopoulou, E. *Stud. Conserv.* **1998**, *43*, 17-32.
- [39] Tetreault, J.; Cano, E.; van Bommel, M.; Scott, D.; Dennis, M.; Barthes-Labrousse, M. G.; Minel, L.; Robbiola, L. *Stud. Conserv.* **2003**, *48*, 237-250.
- [40] Bertolotti, G.; Bersani, D.; Lottici, P. P.; Alesiani, M.; Malcherek, T.; Schluter, J. *Anal. Bioanal. Chem.* **2012**, *402*, 1451-1457.
- [41] Bersani, D.; Campani, E.; Casoli, A.; Lottici, P. P.; Marino, I. G. *Anal. Chim. Acta* **2008**, *610*, 74-79.

- [42] Matovic, V.; Vaskovic, N.; Eric, S.; Sreckovic-Batocanin, D. *Environ. Earth Sci.* **2010**, *60*, 1153-1164.
- [43] Kotulanová, E.; Bezdička, P.; Hradil, D.; Hradilová, J.; Švarcová, S.; Grygar, T. *Journal of Cultural Heritage* **2009**, *10*, 367-378.
- [44] Aze, S. *Alterations chromatiques des pigments au plomb dans les œuvres du patrimoine - Etude expérimentale des altérations observées sur les peintures murales*. PhD, Université de Droit, d'Economie et des Sciences d'Aix-Marseille 2005.
- [45] Corbeil, M. C.; Sirois, P. J. *Stud. Conserv.* **2007**, *52*, 281-288.





---

# Chapter 7 – Conclusions

---

At or below the surface of painted works of art, valuable information is present that provides insights into an object's past, such as the artist's technique and the creative process that was followed or its conservation history, but also on its current state of preservation. Various noninvasive techniques have been developed over the past two decades that can probe this information either locally (via point analysis) or on a macroscopic scale (e.g. full-field imaging and raster scanning).

In this work instrumentation for MA-XRPD was developed and employed for the investigation of painted works of art. MA-XRPD allows for mapping of crystalline compounds present in paint layers, complementing the elemental distribution images provided by MA-XRF and the molecular features imaged with hyperspectral imaging. When exposed to a monochromatic and quasi-parallel X-ray beam, each type of crystal generates its own unique diffraction pattern. Different crystalline materials can be identified by comparing their unique 'fingerprints' against a database of known minerals and compounds. In MA-XRPD a (slightly) focused and monochromatic X-ray beam is used to raster-scan the surface of painted works of art (typically with 1 mm<sup>2</sup> steps), while in each point a diffraction pattern is recorded. Compound-specific distributions are finally obtained by assigning each pixel in the image with a grey scale value that relates to the scaling factor of the recorded diffraction signals. For this purpose dedicated XRPD imaging software (XRDU) initially developed for scanning and tomographic imaging at synchrotron radiation (SR) facilities proved essential.

While several different configurations have been used throughout this work, the fundamental components of these instruments remain the same. The developed transportable laboratory X-ray powder diffraction setup consists of a microfocus X-ray source that delivers a monochromatic and focused X-ray beam (0.1 - 0.5 mm) using a set of curved multilayer mirrors, while a two-dimensional hybrid photon counting area detector is used for capturing diffraction images. The hybrid photon counting detector was chosen over other area detectors, such as charge-coupled device or image plate detectors that are traditionally used in two-dimensional XRPD because of its very fast read-out, significantly reducing the time between consecutive measurements. On the side of the X-ray source, a viable alternative could be the use of double curved crystal optics [1]. The source and detector are augmented with a motorized sample/artefact stage and appropriate control software to create a scanning MA-XRPD instrument.

By changing the geometry of the different components, imaging investigations can be performed both in transmission and in reflection mode allowing for either depth-averaged or superficial information. In transmission mode, a Ag-anode source, with a high primary energy, was used for the analysis of thicker, more absorbing objects, while a Cu-anode source, which typically delivers a higher flux, was shown to be best suited for the investigation of thinner materials. In reflection mode, due to geometrical constraints, the Cu source is preferred; for the same crystalline material the lower primary energy results in diffraction signals at higher scattering angles.

Through the successful conversion of XRPD imaging, which was only available at SR facilities, into a transportable scanning instrument, this work has made a valuable contribution to the array of noninvasive analytical (imaging) techniques that are becoming the preferred methods of investigation for irreplaceable works of art. The capabilities of the MA-XRPD instrument have been demonstrated on

several case studies, illustrating its high degree of specificity on a chemical, material and spatial level.

The large-scale maps obtained with MA-XRPD provide a much higher degree of specificity compared to MA-XRF as shown on a 15<sup>th</sup>/16<sup>th</sup> century illuminated manuscript, differentiating between multiple Ca, Cu and Pb containing pigments. Furthermore, quantification of azurite and two of its impurities, barite and quartz, allowed to visualize two distinct applications of the blue paint mixture. Additionally, by looking at the hydrocerussite-cerussite ratio of the lead white paint, different mixtures could be linked to different pictorial features. In this case, the high flux of the Cu-source allowed for fast scanning with a dwell time of 0.2 seconds per point.

For the crystallographically very similar chrome yellow pigments,  $\text{PbCrO}_4$  and  $\text{PbCr}_{1-x}\text{S}_x\text{O}_4$  ( $x \approx 0.5$ ), the specificity of MA-XRPD allowed to highlight their different usage by Van Gogh on *Sunflowers* (1889, F458, oil on canvas, Van Gogh Museum, NL). The latter chrome yellow subtype exhibits a strong difference in chemical stability when exposed to light, leading to an olive-brown superficial discoloration. It is thus important for conservators and curators to know if and where this sensitive yellow pigment is present and in which pigment mixtures it is employed.

The study of three flower still life paintings, *Flowers and Insects* (Royal Museum of Fine Arts Antwerp, BE) and *Festoon of Fruit and Flowers* (Rijksmuseum, NL) by Jan Davidsz. de Heem and a copy painting by an unknown artist after De Heem's *Still Life with Fruit and a Lobster* (Rijksmuseum, NL) revealed that next to original pigment material, also degradation products can be revealed. These products can be formed *in situ* as a result of spontaneously occurring chemical reactions inside the paint. This unique advantage of chemical imaging paves new ways for the

monitoring of restoration treatments or for guiding sampling campaigns to strategic areas based on the macroscopic distributions of the alteration products.

The majority of studies in the field of cultural heritage employs XRPD as a means to identify crystalline species in e.g., paint samples, or powders scraped from metal objects, sculptures, stone monuments and historical glass. To facilitate identification an accurate determination of the diffraction peak positions is necessary which are subsequently compared to reference databases. This is possible only if the sample is placed at a fixed calibrated distance. For samples that are made up of several distinct layers, only one of these layers can be placed at the calibrated distance, resulting in a shift between the measured and reference peak positions for the crystalline species present in the other layers. On a 15<sup>th</sup>/16<sup>th</sup> century illuminated parchment, this limited shift is exploited to differentiate between pigments applied on the front or back side of the parchment. The sensitivity of MA-XRPD for this displacement is determined by the angular resolution of the instrument. However also the energy of the primary X-rays and the distance between the area detector and the artefact can significantly influence the depth-sensitivity.

Additionally, on Van Gogh's *Sunflowers* it was possible to visualize the orientation of the chrome yellow crystallites.  $\text{PbCr}_{1-x}\text{S}_x\text{O}_4$  ( $x \approx 0.5$ ) crystals inside the chrome yellow paint were shown to be aligned with the direction of the brush strokes made by the artist. While this information is mostly lost after azimuthal integration to 1D diffractograms, it is contained within the 2D diffraction images. Since the noninvasive determination of crystal orientations within paint layers is a novel discovery, its impact remains unsure. However, studies concerning the red pigment hematite ( $\text{Fe}_2\text{O}_3$ ) have shown that when this pigment is applied to wall paintings, the hematite particles can freely orient and align themselves with the Earth's magnetic field before the paints dries. Extracting information about the

orientation of these particles is postulated to potentially facilitate the dating of painted artworks in general [2].

Next to investigations on the macroscopic scale, at SR facilities, the sequence of layers used by an artist to create the desired visual effect can be investigated on minute paint samples (typically  $< 1 \text{ mm}^2$ ) with very narrow X-ray beams (in the order of  $1 \mu\text{m}^2$ ). In addition to gaining insights into an artist's *modus operandi*, further information about degradation processes that occur spontaneously inside the paint layers can be revealed. While 2D mapping experiments (two translation movements) provide projective images, resulting in the loss of depth information, this work has shown that the virtual cross-section achieved with diffraction tomography (one translation and one rotation movement) can be used to further elucidate the degradation sequence of red lead. A downside of synchrotron radiation facilities is that they are typically not equipped to deal with large objects ( $\text{dm}^2 - \text{m}^2$ ), and the risk and costs associated with the transportation of precious artworks to these large-scale facilities limits the number of macroscopic investigations.

While the handful of case studies published to date illustrates the potential of MA-XRPD imaging, the instrument developed in this work is not without its limitations. Using the latest developments in X-ray optics and area detectors, the measurement time per point remains relatively slow for an imaging technique (0.2 – 10 s range). This way, only relatively small areas can be investigated within a reasonable time frame. On the side of the area detector there is only limited improvement possible to speed-up the scanning process: recently CdTe has been introduced as sensor material which yields a higher detection efficiency for higher energies ( $> 90\%$  for Ag- $K_{\alpha}$ ; 1 mm thickness) compared to the conventional Si crystals ( $\sim 50\%$  for Ag- $K_{\alpha}$ ; 1 mm thickness). This could potentially double the scanning speed for high energy X-rays. However, for low energetic X-rays (e.g.,

Cu-K $\alpha$ ) the detection efficiency of current detector technology is already > 90%. Therefore, a more significant increase in scanning speed will depend on improvements of X-ray source and optic technology.

In transmission mode, several constraints are currently imposed on the size and substrate of the works of art that can be investigated. In this mode, the work of art is translated while the instrument remains stationary, limiting the weight of the object to the carrying capacity of the motorized stages. Upgrading to large, dedicated motorized rail systems will expand the range of moveable artworks that can be investigated, but are present in few museums. Additionally works on panel, or regions in front of a stretcher bar strongly hamper or prevent their investigation because of the strong attenuation of the diffracted X-rays by the wooden supports. Further development of the instrument in reflection mode, allowing the work of art to remain stationary while the instrument performs the scanning movement (in analogy to MA-XRF), can be a solution and opens up avenues to immovable objects, such as mural paintings.

## REFERENCES

- [1] Chen, Z. W.; Gibson, W. M. *Powder Diffr.* **2002**, *17*, 99-103.
- [2] Chiari, G.; Lanza, R. *Phys. Earth Planet. Inter.* **1997**, *101*, 79-83.





---

# Abstract

---

At or below the surface of painted works of art, valuable information is present that provides insights into an object's past, such as the artist's technique and the creative process that was followed or its conservation history, but also on its current state of preservation. Typically, a (very) limited set of small paint samples is taken which provide direct access to the individual paint layers. The chemical build-up of these layers can then be investigated in great detail using various microscopic analytical methods. However, in recent years a new trend towards both elemental and chemical imaging techniques has been set which are capable of visualizing the (often) heterogeneous composition of painted objects on a macroscopic scale.

In this dissertation, various forms of specificity attainable with X-ray powder diffraction (XRPD) imaging are explored: at the chemical, material and spatial level. This high specificity is illustrated throughout several applications stemming from the field of cultural heritage, both at the macroscopic (MA) and microscopic ( $\mu$ ) scale.

As a first step, XRPD imaging was transformed to a transportable instrument that can be employed for the *in situ* investigation of artworks, e.g., inside museums and conservation workshops. With this unique instrument large-scale maps ( $\text{cm}^2 - \text{dm}^2$ ) reflecting the distribution of crystalline phases on/below the surface of flat painted artefacts can be visualized in a noninvasive manner. In this way compound-specific information was attained which can be related to original pigments or materials that have been added in a later stage and even degradation/secondary products that have formed spontaneously inside the paint

layers. The degradation processes of arsenic sulfide pigments and the formation of (thin) sulfate layers at the surface of different 17<sup>th</sup> century paintings by Jan Davidsz. de Heem could be investigated in this manner. These investigations revealed the strong tendency of arsenate ions to precipitate with lead, while various secondary  $\text{Pb}^{2+}$ ,  $\text{Ca}^{2+}$  and  $\text{K}^{2+}$  (mixed) sulfates are able to form in specific regions on the paintings depending on available ion sources.

Additionally, with MA-XRPD imaging it was possible to link quantitative information of pigment compositions to the 2D compound-specific distribution images, allowing for a further distinction between very similar artists' materials. This was shown for three different types of lead white paint and two different applications of azurite on a single 15<sup>th</sup>/16<sup>th</sup> century illuminated sheet of parchment. Furthermore, the limited depth-selectivity of this technique, obtained by exploiting the small shift in the position of the diffraction signals, allowed to differentiate between pigments applied on either the *recto* or *verso* side of the parchment.

Employing MA-XRPD for the investigation of different types of the chrome yellow pigment,  $\text{PbCr}_{1-x}\text{S}_x\text{O}_4$ , used by Van Gogh on *Sunflowers* (Van Gogh Museum, Amsterdam), illustrated that two specific subtypes of chrome yellow are present: monoclinic  $\text{PbCrO}_4$  and monoclinic  $\text{PbCr}_{1-x}\text{S}_x\text{O}_4$  ( $x \approx 0.5$ ). While the former is stable, the latter is prone to discoloration. Preferred orientation effects were found in the sensitive chrome yellow type which could be linked to the direction of the brushstrokes made by Van Gogh.

Finally, a minute paint sample from *Wheat stack under a cloudy sky* by Van Gogh was investigated at a synchrotron radiation facility with tomographic  $\mu$ -XRPD imaging at the microscopic scale. The high chemical and spatial specificity of this imaging method was exploited to further elucidate the degradation pathway of the red lead pigment.

---

# Samenvatting

---

Aan of net onder het oppervlak van geschilderde kunstwerken ligt waardevolle informatie waarmee inzichten in het verleden van een kunstobject kunnen worden verworven, zoals de gebruikte techniek en het creatieve proces dat werd gevolgd door een kunstenaar of de conservatie geschiedenis van het object, maar ook over de huidige staat van bewaring. Meestal wordt een (heel) kleine set van minuscule verfmonsters genomen, zodat directe toegang tot de individuele verf lagen mogelijk wordt. De chemische opbouw van deze verschillende lagen kan vervolgens tot in detail worden onderzocht door middel van verschillende analytische microscopie methoden. Echter, in afgelopen jaren is er een nieuwe trend zichtbaar om zowel elementaire en moleculaire beeldvormende technieken te gebruiken waarmee de heterogene samenstelling van geschilderde objecten op macroscopische schaal kan worden getoond.

In dit doctoraatsonderzoek werden verschillende vormen van specificiteit onderzocht die verkregen kunnen worden met röntgen-poederdiffractie (XRPD) als beeldvormende methode: zowel op een chemisch, materieel en ruimtelijk niveau. Deze hoge graad van specificiteit werd aangetoond aan de hand van verscheidene toepassingen afkomstig uit het veld van het cultureel erfgoed, zowel op de macroscopische (MA) en microscopische ( $\mu$ ) schaal.

Als eerste stap werd een transporteerbaar instrument ontwikkeld dat toestaat om kunstwerken *in situ* te onderzoeken met XRPD-beeldvorming, bv. in een museum of conservatie atelier. Met dit uniek instrument worden, op een niet invasieve manier, macroscopische distributiebeelden verkregen ( $\text{cm}^2$  –  $\text{dm}^2$ ) die overeenkomen met de verdeling van de kristallijne fasen aanwezig op/onder het

oppervlak van vlakke geschilderde kunstwerken. Deze verbindingsspecifieke beelden leveren informatie op over originele pigmenten of over materialen die in een latere fase werden aangebracht, maar ook over degradatie/secondaire producten die spontaan zijn gevormd binnenin de verflagen. Het degradatieproces van arseen sulfide pigmenten en de vorming van (dunne) sulfaat-rijke laagjes aan het oppervlak van verschillende 17<sup>de</sup>-eeuwse schilderijen van Jan Davidsz. de Heem konden op deze wijze worden onderzocht. Uit dit onderzoek blijkt dat arsenaat ionen een sterke neiging hebben om neer te slaan met lood, terwijl verschillende secondaire  $Pb^{2+}$ ,  $Ca^{2+}$  en  $K^{2+}$  (gemengde) sulfaten in specifieke gebieden kunnen vormen, afhankelijk van de aanwezige ionen.

Daarnaast was het mogelijk om met MA-XRPD-beeldvorming kwantitatieve informatie over de samenstelling van pigmenten te koppelen aan de 2D verbindingsspecifieke verdelingsbeelden, waardoor verder onderscheid gemaakt kon worden tussen zeer gelijkaardige verfmaterialen. Dit werd aangetoond voor drie verschillende types van het pigment loodwit en twee verschillende types van azuriet op een 15<sup>de</sup>/16<sup>de</sup>-eeuws verlucht perkament. Bijkomend werd aangetoond dat de gelimiteerde diepte-gevoeligheid van deze techniek in staat is om onderscheid te maken tussen pigmenten die op de voor- of achterkant van het perkament werden aangebracht. Deze gevoeligheid uit zich in een zeer kleine verschuiving in de positie van diffractiesignalen wanneer deze afkomstig zijn vanuit verschillende dieptes in de laagstructuur van de verf.

Verder werd het MA-XRPD instrument ingeschakeld om het gebruik van verschillende types van het pigment chroomgeel,  $PbCr_{1-x}S_xO_4$ , door Van Gogh in *Zonnebloemen* (Van Gogh Museum, Amsterdam) na te gaan. Hierbij werd aangetoond dat twee verschillende types van chroomgeel werden gebruikt: monoklien  $PbCrO_4$  en monoklien  $PbCr_{1-x}S_xO_4$  ( $x \approx 0.5$ ). Terwijl het eerste type stabiel is, vertoont het tweede type de neiging tot verkleuring. Het gevoelige

chromgeel vertoond overigens voorkeursoriëntatie dewelke gekoppeld kon worden aan de richting waarin Van Gogh penseelstreken aanbracht op het schilderij.

Tot slot werd een minuscuul verfmonster bekomen van het schilderij *Korenschelf onder wolkenlucht* gemaakt door Van Gogh onderzocht op microscopische schaal aan een synchrotron faciliteit met tomografische  $\mu$ -XRPD-beeldvorming. De hoge chemische en ruimtelijke specificiteit van deze beeldvormende methode werd toegepast om het degradatiemechanisme van het pigment loodmenie verder te ontrafelen.



---

# Appendix – Publications

---

## AI Journal Articles

- [1] Salvant, J.; Williams, J.; Ganio, M.; Casadio, G.; Daher, C.; Sutherland, K.; Monico, L.; **Vanmeert, F.**; De Meyer, S.; Janssens, K.; Cartwright, C.; Walton, M.; “A Roman Egyptian Painting Workshop: technical investigation of the portraits from Tebtunis, Egypt”, *Archaeometry*, **2018**, *60* (4), 815-833, DOI: 10.1111/arcm.12351
- [2] **Vanmeert, F.**; Hendriks, E.; Van der Snickt, G.; Monico, L.; Dik, J.; Janssens, K.; “Chemical Mapping by Macroscopic X-ray Powder Diffraction (MA-XRPD) of Van Gogh's Sunflowers: identification of areas with higher degradation risk”, *Angew. Chem. Int. Ed.*, **2018**, *57* (25), 7418-7422, DOI: 10.1002/anie.201713293
- [3] Hirayama, A.; Abe, Y.; van Loon, A.; De Keyser, N.; Noble, P.; **Vanmeert, F.**; Janssens, K.; Tantrakarn, K.; Taniguchi, K.; Nakai, I.; “Development of a new portable X-ray powder diffractometer and its demonstration to on-site analysis of two selected old master paintings from the Rijksmuseum”, *Microchem. J.*, **2018**, *138*, 266-272, DOI: 10.1016/j.microc.2018.01.003
- [4] **Vanmeert, F.**; De Nolf, W.; Dik, J.; Janssens, K.; “Macroscopic X-ray powder diffraction scanning: possibilities for quantitative and depth-selective parchment analysis”, *Anal. Chem.*, **2018**, *90* (11), 6445-6452, DOI: 10.1021/acs.analchem.8b00241



- [5] **Vanmeert, F.**; De Nolf, W.; De Meyer, S.; Dik, J.; Janssens, K.; “Macroscopic X-ray powder diffraction scanning, a new method for highly selective chemical imaging of works of art: instrument optimization”, *Anal. Chem.*, **2018**, *90* (11), 6436-6444, DOI: 10.1021/acs.analchem.8b00240
- [6] Cagno, S.; Brede, D. A.; Nuyts, G.; **Vanmeert, F.**; Pacureanu, A.; Tucoulou, R.; Cloetens, P.; Falkenberg, G.; Janssens, K.; Salbu, B.; Lind, O. C.; “Combined computed nanotomography and nanoscopic x-ray fluorescence imaging of cobalt nanoparticles in caenorhabditis elegans”, *Anal. Chem.*, **2017**, *89* (21), 11435-11442, DOI: 10.1021/acs.analchem.7b02554
- [7] Idaszek, J.; Brynk, T.; Jaroszewicz, J.; **Vanmeert, F.**; Bruinink, A.; Świążzkowski, W.; “Investigation of mechanical properties of porous composite scaffolds with tailorable degradation kinetics after in vitro degradation using digital image correlation”, *Polym. Compos.*, **2015**, *38* (11), 2402-2410, DOI: 10.1002/pc.23825
- [8] Van der Snickt, G.; Legrand, S.; Caen, J.; **Vanmeert, F.**; Alfeld, M.; Janssens, K.; “Chemical imaging of stained-glass windows by means of macro X-ray fluorescence (MA-XRF) scanning”, *Microchem. J.*, **2016**, *124*, 615-622, DOI: 10.1016/j.microc.2015.10.010
- [9] Monico, L.; Janssens, K.; Cotte, M.; Sorace, L.; **Vanmeert, F.**; Brunetti, B. G.; Miliani, C.; “Chromium speciation methods and infrared spectroscopy for studying the chemical reactivity of lead chromate-based pigments in oil medium”, *Microchem. J.*, **2016**, *124*, 272-282, DOI: 10.1016/j.microc.2015.08.028

- [10] 't Hart, L.; Storme, P.; Anaf, W.; Nuyts, G.; **Vanmeert, F.**; Dorriné, W.; Janssens, K.; De Wael, K.; Schalm, O.; “Monitoring the impact of the indoor air quality on silver cultural heritage objects using passive and continuous corrosion rate assessments”, *Appl. Phys. A*, **2016**, *122* (923), DOI: 10.1007/s00339-016-0456-2
- [11] Janssens, K.; Van der Snickt, G.; **Vanmeert, F.**; Legrand, S.; Nuyts, G.; Alfeld, M.; Monico, L.; Anaf, W.; De Nolf, W.; Vermeulen, M.; Verbeeck, J.; De Wael, K.; “Non-invasive and non-destructive examination of artistic pigments, paints, and paintings by means of X-Ray methods”, *Top. Curr. Chem.*, **2016**, *374* (6), DOI: 10.1007/s41061-016-0079-2
- [12] Janssens, K.; Legrand, S.; Van der Snickt, G.; **Vanmeert, F.**; “Virtual archaeology of altered paintings: multiscale chemical imaging tools”, *Elements*, **2016**, *12* (1), 13-18, DOI: 10.2113/gselements.12.1.39
- [13] Pouyet, E.; Cotte, M.; Fayard, B.; Salomé, M.; Meirer, F.; Mehta, A.; Uffelman E.S.; Hull, A.; **Vanmeert, F.**; Kieffer, J.; Burghammer, M.; Janssens, K.; Sette, F.; Mass, J.; “2D X-ray and FTIR micro-analysis of the degradation of cadmium yellow pigment in paintings of Henri Matisse”, *Appl. Phys. A*, **2015**, *121* (3), 1-14, DOI: 10.1007/s00339-015-9239-4
- [14] Odin, G.; **Vanmeert, F.**; Farges, F.; Gand, G.; Janssens, K.; Romero-Sarmiento, MF.; Steyer, J.; Vantelon, D.; Rouchon, V.; “Alteration of fossil-bearing shale (Autun, France; Permian), part II: monitoring artificial and natural ageing by combined use of S and Ca K-edge XANES analysis, Rock-Eval pyrolysis and FTIR analysis”, *Annales de Paléontologie*, **2015**, *101* (3), 225-239, DOI: 10.1016/j.annpal.2015.03.001

- [15] Monico, L.; Janssens, K.; Hendriks, E.; **Vanmeert, F.**; Van der Snickt, G.; Cotte, M.; Falkenberg, G.; Brunetti, B. G.; Miliani, C.; “Evidence for degradation of the chrome yellows in Van Gogh's sunflowers: a study using noninvasive in situ methods and synchrotron-radiation-based x-ray techniques”, *Angew. Chem. Int. Ed.*, **2015**, *54* (47), 13923-13927, DOI: 10.1002/anie.201505840
- [16] Monico, L.; Janssens, K.; Alfeld, M.; Cotte, M.; **Vanmeert, F.**; Ryan, C. G.; Falkenberg, G.; Howard, D. L.; Brunetti, B. G.; Miliani, C.; “Full spectral XANES imaging using the Maia detector array as a new tool for the study of the alteration process of chrome yellow pigments in paintings by Vincent van Gogh”, *J. Anal. At. Spectrom.*, **2015**, *30* (3), 613-626, DOI: 10.1039/c4ja00419a
- [17] **Vanmeert, F.**; Van der Snickt, G.; Janssens, K.; “Plumbonacrite identified by X-ray powder diffraction tomography as a missing link during degradation of red lead in a Van Gogh painting”, *Angew. Chem. Int. Ed.*, **2015**, *54* (12), 3607-3610, DOI: 10.1002/anie.201411691
- [18] Odin, G.; **Vanmeert, F.**; Janssens, K.; Lelièvre, H.; Mertz, J-D.; Rouchon, V.; “Accelerated ageing of shales of palaeontological interest: impact of temperature conditions”, *Annales de Paléontologie*, **2014**, *100* (2), 137-149, DOI: 10.1016/j.annpal.2013.12.002
- [19] Monico, L.; Janssens, K.; **Vanmeert, F.**; Cotte, M.; Brunetti, B. G.; Van der Snickt, G.; Leeuwestein, M.; Salvant, J.; Menu, M.; Miliani, C.; “Degradation process of lead chromate in paintings by Vincent van Gogh studied by means of spectromicroscopic methods: part 5: effects of nonoriginal surface coatings into the nature and distribution of chromium and sulfur species in chrome yellow paints”, *Anal. Chem.*, **2014**, *86* (21), 10804-10811, DOI: 10.1021/ac50284lg

- [20] Legrand, S.; **Vanmeert, F.**; Van der Snickt, G.; Alfeld, M.; De Nolf, W.; Dik, J.; Janssens, K.; “Examination of historical paintings by state-of-the-art hyperspectral imaging methods: from scanning infra-red spectroscopy to computed X-ray laminography”, *Heritage Science*, **2014**, 2 (13), DOI: 10.1186/2050-7445-2-13
- [21] Legrand, S.; Alfeld, M.; **Vanmeert, F.**; De Nolf, W.; Janssens, K.; “Macroscopic Fourier transform infrared scanning in reflection mode (MA-rFTIR), a new tool for chemical imaging of cultural heritage artefacts in the mid-infrared range”, *Analyst*, **2014**, 139 (10), 2489-2498, DOI: 10.1039/c3an02094k
- [22] De Nolf, W.; **Vanmeert, F.**; Janssens, K.; “XRDU: crystalline phase distribution maps by two-dimensional scanning and tomographic (micro) X-ray powder diffraction”, *J. Appl. Crystallogr.*, **2014**, 47 (3), 1107-1117, DOI: 10.1107/s1600576714008218
- [23] Da Pieve, F.; Hogan, C.; Lamoen, D.; Verbeeck, J.; **Vanmeert, F.**; Radepont, M.; Cotte, M.; Janssens, K.; Gonze, X.; Van Tendeloo, G.; “Casting light on the darkening of colors in historical paintings”, *Phys. Rev. Lett.*, **2013**, 111 (20), 208302, DOI: 10.1103/physrevlett.111.208302
- [24] Monico, L.; Janssens, K.; Miliani, C.; Brunetti, B. G.; Vagnini, M.; **Vanmeert, F.**; Falkenberg, G.; Abakumov, A.; Lu, Y.; Tian, H.; Verbeeck, J.; Radepont, M.; Cotte, M.; Hendriks, E.; Geldof, M.; van der Loeff, L.; Salvant, J.; Menu, M.; “Degradation process of lead chromate in paintings by Vincent van Gogh studied by means of spectromicroscopic methods: part 3: synthesis, characterization, and detection of different crystal forms of the chrome yellow pigment”, *Anal. Chem.*, **2013**, 85 (2), 851-859, DOI: 10.1021/ac302158b

- [25] Mudronja, D.; **Vanmeert, F.**; Hellemans, K.; Fazinic S.; Janssens, K.; Tibljas D.; Rogosic, M.; Jakovljevic, S.; “Efficiency of applying ammonium oxalate for protection of monumental limestone by poultice, immersion and brushing methods”, *Appl. Phys. A: Mater. Sci. Process.*, **2013**, *III (1)*, 109-119, DOI: 10.1007/s00339-012-7365-9
- [26] Alfeld, M.; Van der Snickt, G.; **Vanmeert, F.**; Janssens, K.; Dik, J.; Appel, K.; van der Loeff, L.; Chayannes, M.; Meedendorp, T.; Hendriks, E.; “Scanning XRF investigation of a Flower Still Life and its underlying composition from the collection of the Kröller-Müller Museum”, *Appl. Phys. A*, **2013**, *III (1)*, 165-175, DOI: 10.1007/s00339-012-7526-x
- [27] **Vanmeert, F.**; Mudronja D.; Fazinic, S.; Janssens, K.; Tibljas, D.; “Semi-quantitative analysis of the formation of a calcium oxalate protective layer for monumental limestone using combined micro-XRF and micro-XRPD”, *X-ray Spectrom.*, **2013**, *42 (4)*, 256-261, DOI: 10.1002/xrs.2486
- [28] Janssens, K.; Alfeld, M.; Van der Snickt, G.; De Nolf, W.; **Vanmeert, F.**; Radepon, M.; Monico, L.; Dik, J.; Cotte, M.; Falkenberg, G.; Miliani, C.; Brunetti B.G.; “The use of synchrotron radiation for the characterization of artists' pigments and paintings”, *Annu. Rev. Anal. Chem.*, **2013**, *6*, 399-425, DOI: 10.1146/annurev-anchem-062012-092702
- [29] Van der Snickt, G.; Janssens, K.; Dik, J.; De Nolf, W.; **Vanmeert, F.**; Jaroszewicz, J.; Cotte, M.; Falkenberg, G.; Van der Loeff, L.; “Combined use of synchrotron radiation based micro-X-ray fluorescence, micro-X-ray diffraction, micro-X-ray absorption near-edge, and micro-fourier transform infrared spectroscopies for revealing an alternative degradation pathway of the pigment cadmium yellow in a painting by Van Gogh”, *Anal. Chem.*, **2012**, *84 (23)*, 10221-10228, DOI: 10.1021/ac3015627

- [30] Rouchon, V.; Pellizzi, E.; Duranton, M.; **Vanmeert, F.**; Janssens, K.; “Combining XANES, ICP-AES, and SEM/EDS for the study of phytate chelating treatments used on iron gall ink damaged manuscripts”, *J. Anal. At. Spectrom.*, **2011**, 26 (12), 2589-2597, DOI: 10.1039/c1ja10185d
- [31] Rouchon, V.; Duranton, M.; Burgaud, C.; Pellizzi, E.; Lavedrine, B.; Janssens, K.; de Nolf, W.; Nuyts, G.; **Vanmeert, F.**; Hellemans, K.; “Room-temperature study of iron gall ink impregnated paper degradation under various oxygen and humidity conditions: time-dependent monitoring by viscosity and X-ray absorption near-edge spectrometry measurements”, *Anal. Chem.*, **2011**, 83(7), 2431-2441, DOI: 10.1021/ac1029242

### H3 Book Chapters

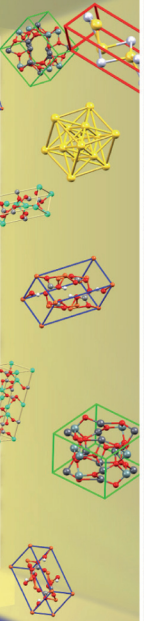
- [1] **Vanmeert, F.**; Van der Snickt, G.; Legrand, S.; Janssens, K.; “Velázquez?: A portrait of Pope Innocent X. An X-ray imaging investigation II”. In: *Velázquez – Suggestions, Proposals, Solutions*, **2018**, 132-141, ISBN 978-3-99020-155-8
- [2] De Meyer, S.; **Vanmeert, F.**; Janssens, K.; Storme, P.; “A mobile scanner for XRPD-imaging of paintings in transmission and reflection geometry”. In: *Acta Artis Academica 2017*, **2017**, 29-38, ISBN 978-80-87108-75-8
- [3] **Vanmeert, F.**; Van der Snickt, G.; Janssens, K.; “Fading of Van Gogh’s red lead pigment”, In: *Photon Science 2015: Highlights and Annual Report*, **2015**, 46-47, ISBN 978-3-945931-00-4

## PI Conference Proceedings

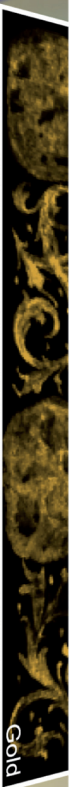
- [1] Storme, P.; Selucká, A.; Rapouch, K.; Mazik, M.; **Vanmeert, F.**; Janssens, K.; Van de Voorde, L.; Vekemans, B.; Vincze, L.; Caen, J.; De Wael, K.; “Composition and corrosion forms on archaeological and non-archaeological historic printing letters from the Moravian Museum, Memorial of Kralice Bible, the Czech Republic and the Museum Plantin-Moretus Antwerp, Belgium”, *Institut du Patrimoine Wallon*, **2015**, 59-65

Februarius habet dies. p̄viii.  
Luna vero. p̄xix.  
dignati epi. vii. d. faustini e ion  
e Purifi. marie. vi. d. celsiane virgini  
p̄blasii epi. vi. d. f  
g gilberti cōfes. iiii. d. g  
A agathe virgi. vi. d. b  
si b dorothee virgi. vii. d. c  
c  
d Lathecia pe  
e apolome virgi. ix. d. e  
ff scolastice vir. x. d. f  
g soliferis pape. p̄viii. d. g  
A si A  
b fulcranni. vi. d. b  
diii. c. viii. c.

asatur ocausta febriis febuario multa.  
otibus et esais si caute minure velis  
ne caue frigoia: de pollice funde cruce  
feurice  
pintemps  
a enseigner  
at a douze ans



Calcite



Gold



Azurite



Cinnabar



Lead Tin Yellow

BACK

FRONT

